ZESZYTY NAUKOWE
POLITECHNIKI RZESZOWSKIEJ

SCIENTIFIC LETTERS
OF RZESZOW UNIVERSITY OF TECHNOLOGY

NR 293

(e-ISSN 2300-5211)

MECHANIKA

Kwartalnik
tom XXXIII
zeszyt 88 (nr 2/2016)
kwiecień-czerwiec

WYDZIAŁ
BUDOWY MASZYN
I LOTNICTWA
POLITECHNIKI RZESZOWSKIEJ

Wydano za zgodą Rektora

R e d a k t o r n a c z e l n y
Wydawnictw Politechniki Rzeszowskiej
prof. dr hab. inż. Leonard ZIEMIAŃSKI

p-ISSN 0209-2689
e-ISSN 2300-5211

Wersja drukowana Kwartalnika jest wersją pierwotną.

Redakcja czasopisma: Politechnika Rzeszowska, Wydział Budowy Maszyn i Lotnictwa
al. Powstańców Warszawy 8, 35-959 Rzeszów (e-mail: tomtrz@prz.edu.pl)
http://oficyna.portal.prz.edu.pl/pl/zeszyty-naukowe/mechanika

Wydawca: Oficyna Wydawnicza Politechniki Rzeszowskiej
al. Powstańców Warszawy 12, 35-959 Rzeszów (e-mail:oficyna1@prz.edu.pl)
http://oficyna.portal.prz.edu.pl

Informacje dodatkowe i stopka – str. 183

SPIS TREŚCI

ZESZYTY NAUKOWE POLITECHNIKI RZESZOWSKIEJ 293, Mechanika 88
RUTMech, t. XXXIII, z. 88 (2/16), kwiecień-czerwiec 2016, s. 91-99

Sergei M. BOSIAKOV[1]
Denis V. ALEKSEEV[2]
Ihar E. SHPILEUSKI[3]
Vadim V. SILBERSCHMIDT[4]
Feliks STACHOWICZ[5]
Tomasz TRZEPIECIŃSKI[6]

FORMATION OF MICROCRACKS NEAR SURGICAL DEFECT IN FEMUR: ASSESSMENT OF ULTIMATE LOADING CONDITIONS

A bone defect of rectangular shape in a femur is considered as a result of a surgical resection of tumor lesions. Based on finite-element calculation of J-integral near the bone defect, ultimate combinations of loads corresponding to formation of microcracks were determined. The loads corresponds to simultaneous actions of own human's weight, flexion-extension, adduction-abduction and rotation of the femur. Recommendations for the prevention of pathological fractures of the femur with the surgical defect based on the obtained results were formulated.

Keywords: surgical resection, compact bone, J-integral, microcracks, combined loading

1. Introduction

The main method of treatment of benign tumours and metastatic lesions of long bones is a surgical removal of the affected area within an unmodified tissue (surgical resection). After surgery, as shown in Figure 1, a sectoral defect of rectangular shape is formed in the bone. As a result, bone strength and functionality of the operated limb decrease and the risk of pathologic fracture of the surgical resection increases.

[1] Autor do korespondencji/corresponding author: Sergei Bosiakov, Belarusian State University, Nezavisimosti 4, 220030 Minsk, Belarus, e-mail: bosiakov@bsu.by

[2] Denis V. Alekseev, Belarusian State University, e-mail: onardeon@gmail.com

[3] Ihar E. Shpileuski, Republican Scientific and Practical Centre for Traumatology and Orthopedics, Minsk, Belarus, e-mail: ihar@gmail.com

[4] Vadim V. Silberschmidt, Loughborough University, UK, e-mail: V.Silberschmidt@lboro.ac.uk

[5,6] Feliks Stachowicz, Tomasz Trzepieciński, Rzeszow University of Technology, Poland, e-mails: stafel@prz.edu.pl, tomtrz@prz.edu.pl

Clinical and radiological criteria of the possibility of loading long bones and the magnitude of the ultimate load on the operated extremity are developed in sufficient detail. However, practical recommendations on compensation of a bone strength loss and the prevention of pathological fracture after a sectoral resection (load limitation, bone reinforcement or external immobilization) are exclusively descriptive.

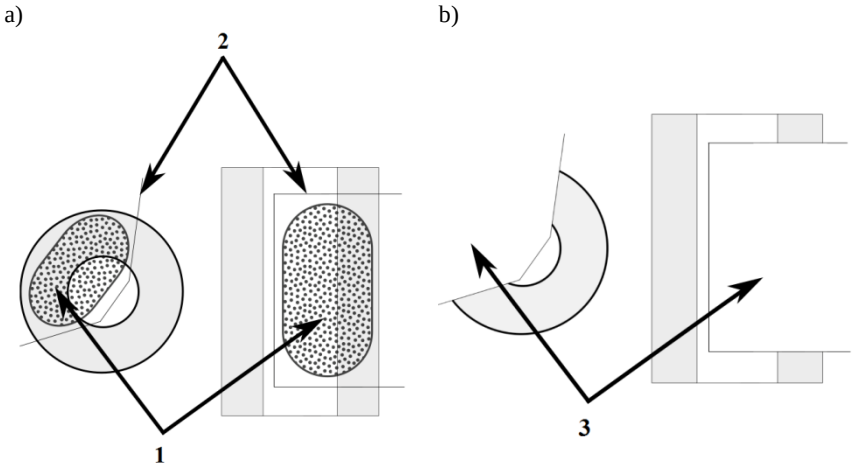

Fig. 1. Scheme of femoral resection: a - fragment of cortical bone before surgical resection (1 - lesion, 2 -line of bone excision), b - fragment of cortical bone after resection (3 - post-resection defect)

A retrospective research of bone functioning and assessment of its fracture risk after a surgical resection of a humerus was performed in [19]. The authors concluded that pathological fractures of the distal humerus were rare and associated with repeated operations; for the prevention of fractures in a proximal region and diaphysis, the use of pros-thesis and fixation, respectively, were suggested. At the same time, development of practical recommendations for the prevention of pathologic fractures after a surgical resection is a fundamental issue, since a restriction of a functional load on an operated limb reduces significantly the patient's ability for self-care and mobility (especially in a case of a lower extremity). Reinforcement of a bone at the level of surgical resection (preventive fixation) can compensate for the loss of strength of the affected segment more fully and minimize a decline in the quality of life; however, this method needs re-intervention to remove the fixation. Development of recommendations on a use of different methods to compensate the loss of bone strength and prevent pathological fracture after a sector resection is required to avoid excessive treatment. Similar recommendations for the prevention of pathological fractures of bone with metastases and tumors took into account a size of the lesion, damage to cortical bone, results of radiographic examination, as well as an increase

in local pain [6, 8, 12]. A scoring system combining radiographic and clinical factors into a single indicator to predict impending fracture was proposed. These approaches were subjected to some criticism in [4] and [18]. Moreover, the authors of these studies stated that indications for prophylactic fixation of impending fractures of long bones were not defined rigorously. So, it is necessary to perform additional research and formulate more stringent criteria for prediction of the risk of potential fractures of long bones with metastatic lesions.

Finite-element (FE) modelling is the most appropriate method for suggestion of objective indicators for the prevention of fractures after surgical resection of bones. This approach is currently widely used for prediction of fractures and corresponding loads as well as localization of fracture in femur under different loading conditions; important results in this area are described in [1, 2, 9, 10, 13, 14]. Assessments of fracture risk and definition of a failure load for bones with metastatic lesions based on the finite-element method were carried out in [3, 5, 7, 15, 16]. In a study on prediction of fracture load and objective assessment of the failure of femur with lytic defects [11], an engineering theory of beams was used in conjunction with tomographic data on structural stiffness. Basically, FE modelling and corresponding experimental verification were carried out for femurs with metastatic lesions of round or oval shape [3, 7, 11, 16]. FE simulations of femurs with rectangular-shaped defects were carried out in [5] and [15]. A maximum width of defects in these studies was assumed to be equal to 0.3 [5] and 0.25 [15] of an external diameter of the bone. Rectangular concentrators due to defect corners were examined in [5]. These concentrators were with the right angles [5] or with rounded edges [15]. The mentioned geometric dimensions of defects do not correspond fully to cuts formed after a sectoral resection; an angular size of post-resection defects can reach $3\pi/2$. Another important feature of post-resection defects is formation of notches in defect's corners after a use of cutting tools. Such notches have a significant effect on development of cracks in a bone.

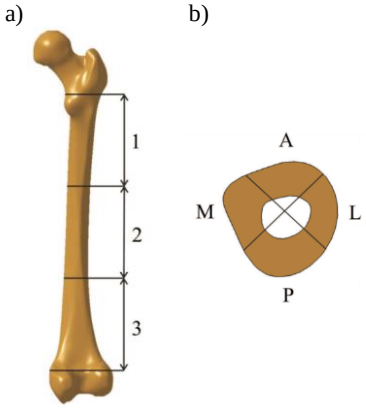

Fig. 2. (a) Three parts of femur diaphysis (posterior view): 1 – top part, 2 – middle part, 3 – bottom part; (b) cross-section of femur in middle part: A – anterior side, M – medial side, P – posterior side, L – lateral side

The aim of this study is the FE-based prediction of ultimate loading combinations that could be applied to a femur with a post-resection defect exposed to combinations of the human's own weight and flexion-tension, adduction-abduction or rotation. The bone defect was considered to be in the medial section of the femur on its medial side. Three main parts of the femur and its different cortices are shown in Figure 2. Recommendations to prevent excessive treatment of patients after surgical resection are formulated on the basis of FE calculations of J-integral and experimental results [20]. These recommendations, primarily, may refer to the description of the unloading regime conditions for patients after surgical resections.

2. FE modelling of femur loading

Computed tomography of a femur was carried out with a spiral X-ray Tomograph (Siemens Somatom Emotion 16) with a slice step of 2.0 mm, and its three-dimensional solid model was obtained by using a computer system of medical image processing ScanIP (Simpleware Ltd., UK). A STL-model was converted into a solid model with CATIA V5 (Dassault Systemes, France). A bone tissue was modelled as a homogeneous transversally isotropic material [1]. Lower sections of the femoral condyles (regions of contact with the condyles of the tibia) were fixed rigidly. The bone defect's length was 64 mm, its angular size was 1800, and the bone defect was located in the femur's middle third on its medial side.

The loads in the model were applied in accordance with the location of the biomechanical z_1-axis and anatomical z_2-axis. Point O_1 (see Figure 3) was the center of the head of the femur; point O_2 was a trochanteric fossa point, point O was located in the center between the two lower condyles. The human's own weight was applied along the z_1-axis to one-third of the area of the femur head. A bending moment for flexion-tension acted in the yz_1-plane (y-axis was parallel to the plane tangent to the condyles of the lower joint). A bending moment for abduction-adduction acted in the xz_1 -plane (x-axis was perpendicular to the yz1-plane). A torsion torque was applied in O_2; distance between point O_2 and biomechanical axis was an arm for the torsion torque of the femur. The used coordinate systems $x0z_1$ and $x0z_2$ are shown in Figure 3. The biomechanical and anatomical axes and the characteristic point were embedded in accordance with recommendations from [21, 22]. In the corners of the post-resection defect, predefined cracks were located in order to calculate values of j-integrals (see Figure 4). The bone was meshed with maximum size of the element 5 mm. Meshes of domains near the corners of the cutting defect were refined (the element size was 0.1 mm) and mapped to achieve higher uniformity. The finite-element model of the femur region with concentrators of the post-resection defect is shown in Figure 4.

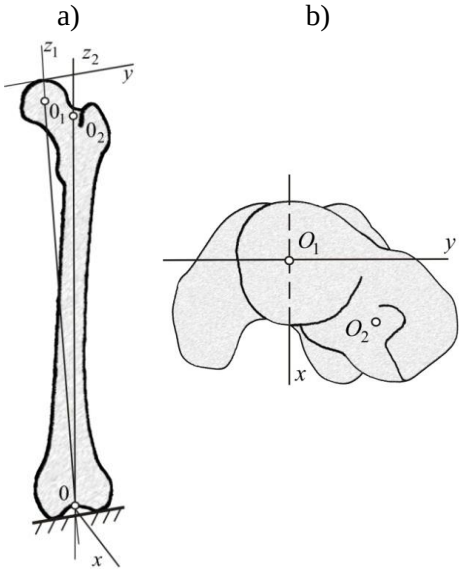

Figure 3. Top (*a*) and side (*b*) view of femur with local coordinate systems; the z_1-axis and z_2-axis are the biomechanical and anatomical axes, respectively; y -axis is parallel to the plane tangent to the condyles of the lower joint; the x -axis is perpendicular to the yz_1-plane. Point O_1 is the center of the head of the femur, point O_2 is a trochanteric fossa point; point O is located in the center between the two lower condyles

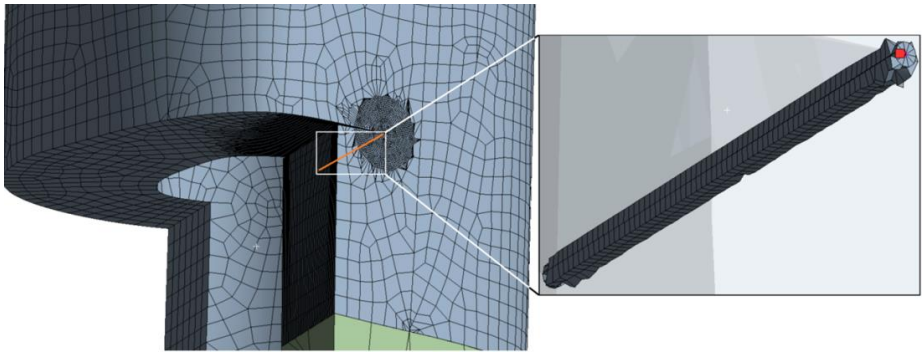

Fig. 4. Finite-element model of femur in middle third of diaphysis (defect length 2d, angular size 1800, length of pre-defined crack for calculations of J-integrals is 3 mm. A zoomed-in part shows finite elements along the crack front

3. Ultimate load combinations

Assessment of ultimate loading conditions for the post-resection bone defect was carried out using the critical value of *J*-integral corresponding to onset of crack propagation obtained in the experiment [20]. The critical *J*-integral was equal approximately to 5925 N/m [20]. Ultimate load combinations corresponded to such combinations of simultaneously applied loads that lead to the critical value of *J*-integral. Several types of load combinations were considered, namely, the human's own weight P together with the flexion-tension moment $T_{\text{f-t}}$, the adduction-abduction moment $T_{\text{a-a}}$ or the torque T_{r}. Figure 5 presents the curves

corresponding to such ultimate load combinations in coordinates ($T_{f\text{-}t}$, P), ($T_{a\text{-}a}$, P) and (T_r, P).

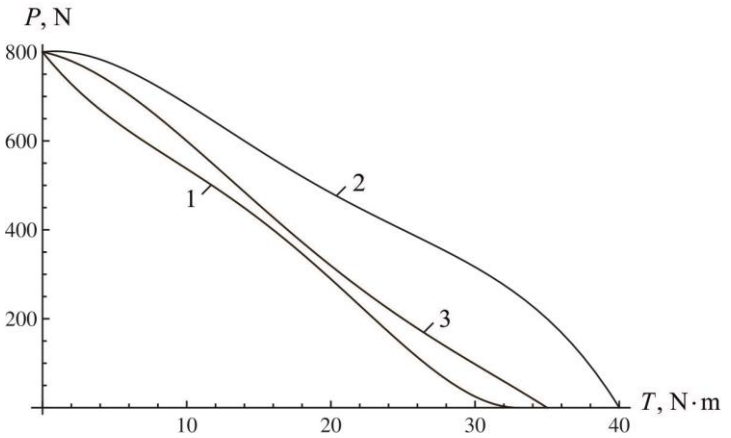

Fig. 5. Ultimate combinations of loading factors: human's own weight P and bending moment $T_{f\text{-}t}$ for flexion-tension (curve 1), bending moment $T_{a\text{-}a}$ for adduction-abduction (curve 2) or torsion torque T_r (curve 3)

The ultimate values of the human's own weight, the bending moments $T_{f\text{-}t}$, $T_{a\text{-}a}$ and the torque T_r corresponding to critical value of J-integral in the cases of, only a single load-applied to the operated bone are shown in Table 1. As reflected by the Figure 5 and Table 1, superposition of the bending moments or the torsion torque on the human's own weight is much more dangerous for a patient than action of their own weight. The most dangerous addition to the human's own weight for the studied type of the post-resection defect is that of the bending moment $T_{f\text{-}t}$ load while the least dangerous that of the bending moment $T_{a\text{-}a}$. Importantly, any additional load can cause a significant reduction of the allowed fraction of weight to be applied to the operated bone.

Table 1. Ultimate magnitudes of human's own weight bending moments and torque

Type of loading	Ultimate magnitudes
Own weight P, N	800.0
Adduction-abduction moment $T_{f\text{-}t}$, N·m	40.0
Flexion-tension moment $T_{a\text{-}a}$, N·m	33.0
Torque T_r, N·m	35.0

4. Conclusions

Finite-element calculations of the J-integrals were used to assess the ultimate combinations of loads (the human's own weight together with one of three types of loads – the flexion-tension moment, the adduction-abduction moment or

the torque for the model of the femur bone after surgical resection. The post-resection defect was in the middle third of the femur on its medial side. The obtained results showed that for defect with this location the most dangerous loads combination was of the human's own weight and $T_{f\text{-}t}$. Nearly the same danger is in the case of action of the weight and the torque T_r. Based on FE simulations, for the post-resection defect with the studied dimensions, any weight in excess of 800 N is critical. For patients with lower weight a discharge regime can be recommended after surgery; if the weight is more than 800 N, reinforcement of the femur bone would be viable; but even in the discharge regime flexion-tension and torsion loads should be avoided. Obviously, some safety margin should be introduced to accommodate significant levels of uncertainty, e.g. dynamic load components. The critical values for the flexion-tension bending moment and the torque can be used to obtain ultimate rotation angles for a femur corresponding to onset of cracking near the post-resection defect. Based on these angles, more precise recommendations for implementing a discharge regime after surgical resection can be formulated for a patient. The approach to obtaining the ultimate loads (both for single and their combinations) applied on the femur bone with post-resection defect based on FE calculation of *J*-integrals presented in this study can be extended to post-resection defect with different sizes as well as to other long human bones (shank, humerus, radius and ulna of forearm).

Acknowledgement

The research leading to these results has received funding from the People Programme (Marie Curie International Research Staff Exchange) of the European Union's Seventh Framework Programme FP7/2007-2013/ under REA grant agreement n° PIRSES-GA-2013-610547.

References

[1] Bessho M., Ohnishi I., Matsuyama J., Matsumoto T., Imai K. Nakamura K.: Prediction of strength and strain of the proximal femur by a CT-based finite element method, J. Biomech., 40 (2007) 1745-1753.

[2] Dall'Ara E., Luisier B., Schmidt R., Kainberger F., Zysset P., Pahr D.: A nonlinear QCT-based finite element model validation study for the human femur tested in two configurations in vitro, Bone, 52 (2013) 27-38.

[3] Derikx L.C., van Aken J.B., Janssen D., Snyers A., van der Linden Y.M., Verdonschot N., Tanck E.: The assessment of the risk of fracture in femora with metastatic lesions, J. Bone Joint Surg., British Vol., 94-B (2012) 1135-1142.

[4] Dijkstra P.D.S., Oudkerk M., Wiggers T.: Prediction of pathological subtrochanteric fractures due to metastatic lesions, Arch. Orthop. Trauma Surg., 116 (1997) 221-224.

[5] Elias J.J., Frassica F.J., Chao E.Y.S.: The open section effect in a long bone with a longitudinal defect - a theoretical modeling study, J. Biomech., 33 (2000) 1517-1522.

[6] Harrington K.D.: New trends in the management of the lower extremity metastases, Clinic. Orthop., 169 (1982) 53-61.

[7] Hipp J.A., Edgerton B.C., An K.-N., Hayes W.C.: Structural consequences of transcortical holes in long bones loaded in torsion, J. Biomech., 23 (1990) 1261-1268.

[8] Hipp J. A., Springfield D.S. Hayes W.C.: Predicting pathologic fracture risk in the management of metastatic bone defects, Clinic. Orthop., 312 (1995) 120-135.

[9] Keyak J.H., Rossi S.A.: Prediction of femoral fracture load using finite element models: an examination of stress- and strain-based failure theories, J. Biomech., 33 (2000) 209-214.

[10] Keyak J.H., Rossi S.A., Jones K.A., Les C.M., Skinner H.B.: Prediction of fracture location in the proximal femur using finite element models, Med. Eng. Phys., 23 (2001) 657-664.

[11] Lee T.: Predicting failure load of the femur with simulated osteolytic defects using noninvasive imaging technique in a simplified load case, Annal. Biomed. Eng., 35 (2007) 642-650.

[12] Mirels H.: Metastatic disease in long bones: a proposed scoring system for diagnosing impending pathologic fractures, Clinic. Orthop., 249 (1989) 256-264.

[13] Ota T., Yamamoto I., Morito R.: Fracture simulation of the femoral bone using the finite-element method: How a fracture initiates and proceeds, J. Bone Min. Metabolism, 17 (1999) 108-112.

[14] Schileo E., Taddei F., Cristofolini L., Viceconti M.: Subject-specific finite element models implementing a maximum principal strain criterion are able to estimate failure risk and fracture location on human femurs tested in vitro, J. Biomech., 41 (2008),356-367.

[15] Spruijt S., van der Linden J. C., Dijkstra P.D.S., Wiggers T., Oudkerk M., Snijders C.J., van Keulen F., Verhaar J.A.N., Weinans H., Swierstra B.A.: Prediction of torsional failure in 22 cadaver femora with and without simulated subtrochanteric metastatic defects, Acta Orthopaed., 77 (2006) 474-481.

[16] Tanck E., van Aken J.B. van der Linden, Y.M., Schreuder H.W.B., Binkowski M., Huizenga H., Verdonschot N.: Pathological fracture prediction in patients with metastatic lesions can be improved with quantitative computed tomography based computer models, Bone, 45 (2009) 777-783.

[17] Tanne T., Sakuda M. Biomechanical and clinical changes of the craniofacial complex from orthopedic maxillary protraction, Angle Orthod., 61 (1991) 145-152.

[18] Van der Linden Y.M., Dijkstra P.D.S., Kroon H.M., Lok J.J., Noordijk E.M. Leer J.W.H., Marijnen C.A.M.: Comparative analysis of risk factors for pathological fracture with femoral metastases, J. Bone Joint Surg., British Vol., Vol. 86-B (2004) 566-573.

[19] Wedin R., Hansen B. H., Laitinen M., Trovik C., Zaikova O., Bergh P., Kalen A., Schwarz-Lausten G., Vult von Steyern F., Walloe A., Kellerand J., Rudiger J. W.: Complications and survival after surgical treatment of 214 metastatic lesions of the humerus, J. Shold. Elbow Surg., 21 (2012) 1049-1055.

[20] Li S.: Cutting of cortical bone tissue: analysis of deformation and fracture process, PhD thesis, Loughborough University, UK, 2013.

[21] Letter to editor: ISB recomendation on definitions of joint coordinate ssytem of various joints for the reporting of human joint motion - part I: ankle, hip, and spine, J. Biomech., 35 (2002) 543-548.

[22] Yoshioka Y., Siu D., Cooke D.V., Chir B.: The anatomy and functional axes of the femur, J. Bone Join. Surg., 69-A, No. 6 (1987) 873-880.

POWSTAWANIE MIKROPĘKNIĘĆ W POBLIŻU WAD CHIRURGICZNYCH KOŚCI UDOWEJ: OCENA WARUNKÓW OBCIĄŻEŃ NISZCZĄCYCH

S t r e s z c z e n i e

W artykule przedstawiono wyniki badań w których analizowano wady kości udowej o prostokątnym kształcie będące wynikiem resekcji chirurgicznej zmian nowotworowych. Na podstawie obliczeń metodą elementów skończonych całki *J* w okolicy wady kości określono niszczące kombinacje obciążeń odpowiadające powstawaniu mikropęknięć. obciążenia odpowiadające jednoczesnemu obciążeniu kości przez ciężar człowieka, obciążenia ściskająco-rozciągające, odwodzenie i obrót kości udowej. Na podstawie uzyskanych wyników sformułowano zalecenia dotyczące zapobiegania patologicznemu złamaniu kości udowej z defektem chirurgicznym.

Słowa kluczowe: resekcja chirurgiczna, kość, całka J, mikropęknięcia, obciążenie złożone

DOI: 10.7862/rm.2016.8

Otrzymano/received: 12.05.2016 r.
Zaakceptowano/accepted: 22.06.2016 r.

ZESZYTY NAUKOWE POLITECHNIKI RZESZOWSKIEJ 293, Mechanika 88
RUTMech, t. XXXIII, z. 88 (2/16), kwiecień-czerwiec 2016, s. 101-113

Wiesław FRĄCZ[1]
Grzegorz JANOWSKI[2]
Gennadi MIKHASEV[3]

THE MANUFACTURING ISSUES OF TECHNICAL PRODUCTS MADE OF POLYIMIDE - CARBON FIBERS COMPOSITE BY MEANS INJECTION MOULDING PROCESS

Nowadays modern commercial simulation software provides acceptably faithful representation of reality, assuming the correctness of boundary conditions and reliability of data of processed composite material. In the case of non-standard plastics which include polyimide, we do not always have access to the target material and we do not have proper equipment to produce such products. Due to very interesting properties of the polyimide and its low popularity in use as an injection moulding material, the analysis of injection moulding of tooth plastic gear made from carbon fiber-polyimide composite was made. In this work the chosen material data, necessary for the numerical analysis, were presented. The impact analysis of main factors controlling the volumetric shrinkage during injection moulding processing was conducted. It was found that the greatest impact on the quality criterion is the melt temperature. To optimize control factors, the Taguchi orthogonal plans were used. In addition, the issue of polyimide properties, the possibility of its injection moulding and applications was discussed.

Keywords: polyimides, polymer composites, numerical simulations, optimization, injection moulding

1. Introduction

Polyimides are polymers which are created by condensation polymerization of pyromellitic anhydrides and primary diamines. The presence of cyclic groups along the polymer chain (fig. 1) results in good specific properties [9]. These compounds contain group -CO-NR-CO as a part of a ring along the polymer chain, which results in high temperature parameters. Use in the synthesis of pol-

[1] Wiesław Frącz, Rzeszow University of Technology, e-mail: wf@prz.edu.pl
[2] Autor do korespondencji/corresponding author: Grzegorz Janowski, Rzeszow University of Technology, 8 Powstańców Warszawy Ave., 35-959 Rzeszów, e-mail: gjan@prz.edu.pl
[3] Gennadi Mikhasev, Belarusian State University, e-mail: mikhasev@bsu.by

yimides aromatic diamine provides exceptional thermal stability. As an example, di-(4-amino-phenyl) ether could be used to produce Kapton - polyimide manufactured by DuPoint [6].

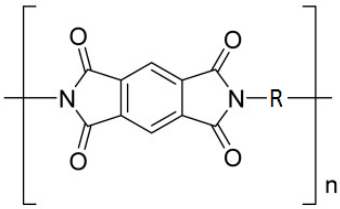

Fig. 1. Structure of polyimide

These materials that have very good physical properties are used in terms in which parts are exposed to aggressive environments. They have excellent high temperature properties and oxidative stability which allows them to withstand continuous operation in air at 260°C [1]. These materials are combustible, but have affinity for self-extinguishing. They are resistant to weak acids and organic solvents. They also have good electrical properties and are resistant to ionizing radiation. They are further characterized by high tensile strength and modulus, excellent abrasion resistance, resistance to creeping and long-term heat resistance in air or in an inert atmosphere. A disadvantage of polyimide is its ability to hydrolyze. Exposure to water or water vapor above 100°C may cause cracking of products made from this polymer [2]. A study where after 1000 hours of exposure in air at 300°C, these polymers retain 90% of its tensile strength was conducted. Moreover, after 1500 h exposure to radiation of the value of about 10 rad and the temperature of 175°C form stability was preserved but it became brittle. The first commercial application of polyimide was the use of it as an enamel wire, then as a coating of glass fiber (Pyre ML, Du Pont) and a film (Kapton, Du Pont). Composite laminates produced by impregnating glass fiber and carbon fiber with a polyimide were pressed and cured at a temperature of about 200°C and then were cured at temperatures up to 350°C. Such laminates can be occasionally used continuously at temperatures up to 250°C and 400°C in the application. The laminates have found use in the aerospace industry, in particular in the production of supersonic aircraft. On the other hand, polyimide foam (Skybond Monsanto) has been used for damping the sound of jet engines. Moreover, fibers from a polyimide by Upjohn and Rhone-Poulenc (KERMEL) were produced [4, 6].

Initially, the main problem of above materials was a narrow range of applications due to the fact, that they could not be formed by standard techniques for thermoplastics. In an attempt to overcome this limitation, in the early 1970s scientists have developed modified polyimides that were more susceptible to processing than common polyimides, but still have significant heat resistance. An

important compound group of such modified polyimides are polyamide (eg. Torlon synthesized by Amoco Chemicals), polybismaleinimides (eg. Kinel manufactured by Rhone-Poulenc), polyesters imides (e.g. Icdal Ti40 Dynamit Nobel), polyether (e.g., Ultem produced by General Electric). For example Torlon is designed to use ironing pressure and injection moulding. In the case of pressing the pressure-molded compound was heated to 280°C then formed at the 340°C at a pressure of 30 MPa. Next to 260°C before the end of the process it was cooled. For injection moulding, plasticized Torlon was injected at about 355°C into a mold maintained at a temperature of 230°C. Products from this material are used to produce: pumps, valves, refrigeration components and electronic components. Typical properties of unfilled polyimide were compared in table 1 [4, 10, 17].

Table 1. Some mechanical and thermal properties of unfilled polyimides

Attribute	Temperature	Kinel (Rhone-Poulenc)	Ultem (General Electric)	Vespel (ICI)	Torlon (Amoco)
Flexular modulus [GPa]	25°C	3.8	3.3	3.5	4.6
	150°C	-	2.5	2.7	3.6
	260°C	2.8	-	2.3	3.0
Heat distortion temperature [°C]		-	200	357	282
Tensile strength [MPa]	25°C	~ 40	100	90	186
	150°C	-	-	67	105
	260°C	~ 25	-	58	52

2. Thermoplastic polyimide with carbon fiber

Polyimide - carbon fiber composites, for example Aurum JCL 3030, is a material designed for injection moulding process. This composite has high mechanical (Tab. 2) and thermal properties (Tab. 3), which allows to use it in many industries such as automotive, machine, aerospace, electronics. This material has good dimensional stability, radiation resistance, resistance to fluids and industrial solvents, low thermal expansion coefficient, creep resistance and low flammability, low wear rate, low surface friction over a wide range of temperatures in dry and lubricating conditions.

Table 2. Mechanical properties of polyimide carbon fiber composite – AURUM JCL 3030 [13]

Attribute	Tensile strength [MPa]	Elongation [%]	Flexural strength [MPa]	Modulus of elasticity [MPa]	Compressive strength [MPa]
22.98°C	229	2	314	17.2	207
148.89°C	144	4	216	15.2	102
Measurement method	ASTM D-638		ASTM D-790		JIS K-7208

AURUM JCL 3030 can be processed by means of injection moulding technology at melt temperature above 400ºC and mold temperature of 200ºC. The granulate should be dried prior to the processing in the oven with air circulation under the following conditions: 8 hours at 220ºC, 10 hours at a temperature of 200ºC and 12 hours at a temperature of 356ºC. The injection pressure should be in a range between 75.84 MPa – 241.32 MPa, screw speed of 100-200 rpm. AURUM can be cleaned through unfilled or glass fiber reinforced polyether, polysulfone and polyetherimide.

Table 3. Thermal properties of polyimide carbon fiber composite - AURUM JCL 3030 [14]

Attribute	Measurement method	Value
Melting temperature [ºC]	DSC	388
Glass transition temperaturę [ºC]	DSC	250
Melt Index [g/10 min]	ASTM D-1238	27-37
Coefficient of thermal expansion [10^{-5}/ºC]	ASTM D-696	(0.6MD/4.7TD)
Heat deflection temperature [ºC]	ASTM D-648	248

The components produced from composite polyimide-carbon fiber are excellent substitutes for metals, ceramics, and other plastics. Products with high strength may be manufactured in form of: thrust washers and o-rings oil for automotive gear and off road vehicles, thermal insulators, parts of jet engines, check ball valves, fittings spline, heat-resistant gears, blades, wear strips and valve seats. Other applications include: elements for hard drives and aluminum silicon wafers, plain bearings and handles [7, 13, 14, 17].

3. The simulation of injection moulding process

Plastic gear wheels are products in which technological problems still occur. Due to the considerable thickness of the walls and their frequent variation, it is difficult to get the proper dimensional accuracy [3, 12]. The main factor which determining for obtaining a correct dimension is shrinkage of the part. Keeping of this value in the required range depends on many factors such as: mold temperature, melt temperature, injection time. Substitution of any of these parameters results in a change in the shrinkage processing, thus changing the geometric dimensions of the part. To determine the required parameters of the injection molding process a lot of experimental tests should be made. In the case of non-standard plastic we do not always have access to target material and we do not have proper equipment to form such product. These restrictions may be replaced by numerical simulations. Numerical analysis can give interesting results, data and often give a solid foundation to start experimental research. There are many economic and technical aspects, which incline to use software, such as CAE. The technical factors include: possibility of process accuracy increasing, antici-

pated problems and their solutions at design stage, the choice of suitable raw materials and optimize process parameters. It is also worth mentioning economic aspects, which include a material saving, while reducing a number of prototype versions and preparation time [5].

Due to the very interesting properties of the polyimide and its low popularity in use as an injection molding material, numerical analysis of gear injection molding process of polyimide-carbon fiber composite was made. The steps of simulation included: the geometrical model preparing, model discretization using 3D finite elements (FE) of tetra type, setting of initial and boundary conditions, numerical analysis and simulation results interpretation. The geometrical model of the gear was designed in the NX8 (fig.2a). Computer simulations were performed using Autodesk Moldflow Insight 2013. The analyzed material with the trade name AURUM JCL3030 - polyimide filled with 30% carbon fiber was used. The numerical model of the gear consisted of over 320 000 FE (fig. 2b).

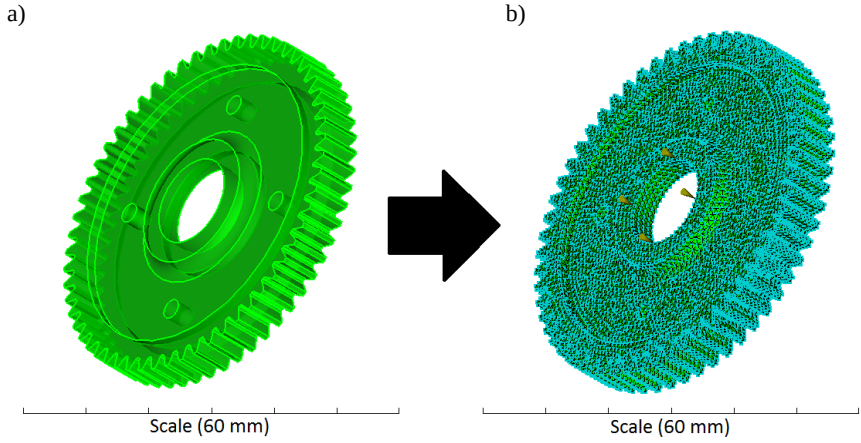

Fig. 2. Gear models: a) geometric model, b) discretized 3D mesh model with injection points locations

4. PVT and rheological characteristics of polyimide-carbon fiber composites

One of the major stages of the simulation test is to define the data describing properties of the processed materials. In the case of polymer composite these data include thermal, rheological, optical, mechanical and processing properties for both polymer matrix and fiber filler.

To carry out the simulation it is necessary to adopt rheological equation of polymer state, which defines the relationship between the viscosity of the polymer, and shear rate. Among the well-known mathematical models the 7-parameter rheological Cross-WLF model was used, which provides a relatively accurate mathematical description of rheological properties of the polymer. In

this model the viscosity of the polymer is determined by Cross equation [11, 15, 16]:

$$\eta\left(\dot{\gamma}, T, p\right) = \frac{\eta_0(T,p)}{1+\left(\frac{\eta_0 \cdot \dot{\gamma}}{\tau^*}\right)^{1-n}} \tag{1}$$

where: η - viscosity of melt polymer, T – temperature, p – pressure, n and τ^* - constant parameters of the model, η_o – the zero shear viscosity. The zero shear viscosity is calculated from the equations by Williams-Landel-Ferry (WLF):

$$\eta_0(T,p) = D_1 \cdot \exp\left[-\frac{A_1 \cdot \left(T - T^*\right)}{A_2 + \left(T - T^*\right)}\right] \tag{2}$$

wherein:

$$T^*(p) = D_2 + D_3 \tag{3}$$

and

$$A_2 + A_3 + D_3 p \tag{4}$$

where: T^* - glass transition temperature, $D1, D2, D3, A_1, A_2, A_3$ - constant parameters of the WLF model.

The parameters of the Cross-WLF model were found in the material database of Autodesk Moldflow Insight 2013 commercial code (tab. 4). Figure 3 shows the viscosity curve used in the numerical analysis.

Table 4. The values of model parameters Cross-WLF for composite AURUM JCL3030

Parameter	n	τ^*	D1	D2	D3	A1	A2~
Unit	-	[Pa]	[Pa*s]	[K]	[K/Pa]	-	[K]
Value	0.4809	15880	1.271e013	523.14	0	25.17	51.6

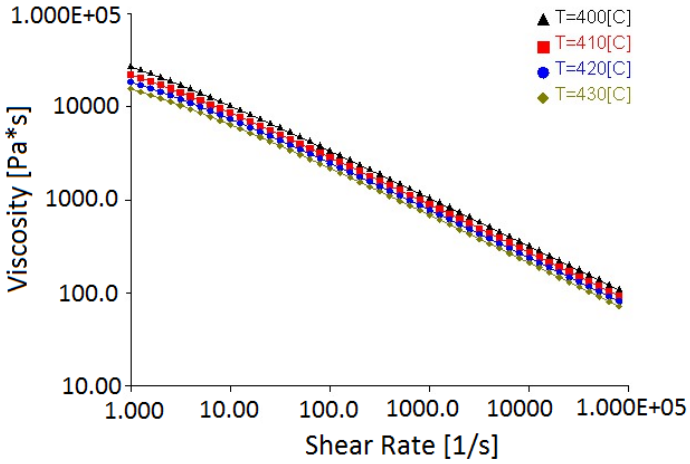

Fig. 3. Viscosity vs. shear rate graph for AURUM JCL3030composite

To determine the composite volumetric shrinkage it is necessary to know the p-V-T characteristics. In numerical calculations the Tait equation was used, which shows the specific volume change as a function of temperature and pressure. The Tait model is given by equations [8, 9, 15]:

$$v(T,p) = v_0(T)[1 - C\ln(1 + \frac{p}{B(T)})] + v_t(T,p) \tag{5}$$

where: $v_t(T,p)$ – specific volume at a given temperature and pressure, T – temperature, p – pressure, C – constant (C = 0.0894), B - pressure sensitivity of the material, defined below:
when $T>T_t$):

$$v_0 = b_{1m} + b_{2m}(T - b_5) \tag{6}$$

$$B(T) = b_{3m}\exp[-b_{4m}(T - b_5)] \tag{7}$$

$$v_t(T,p) = 0 \tag{8}$$

where: b_{1m}, b_{2m}, b_{3m}, b_{4m}, b_5 - data-fitted coefficients (describes the volumetric transition temperature, at zero gauge pressure)
when $T<T_t$:

$$v_0 = b_{1S} + b_{2S}(T - b_5) \tag{9}$$

$$B(T) = b_{3S} \exp[-b_{4S}(T - b_5)] \tag{10}$$

$$v_t(T, p) = b_7 \exp[b_8(T - b_5)) - (b_9 p)] \tag{11}$$

b_{1S}, b_{2S}, b_{3S}, b_{4S}, b_5, b_6, b_7, b_8, b_9 - data-fitted coefficients.

Figure 4 shows the relationship between specific volume and temperature under different pressures. Viscosity curves and p-v-T graph were assumed by Autodesk Moldflow material database, based on experimental data.

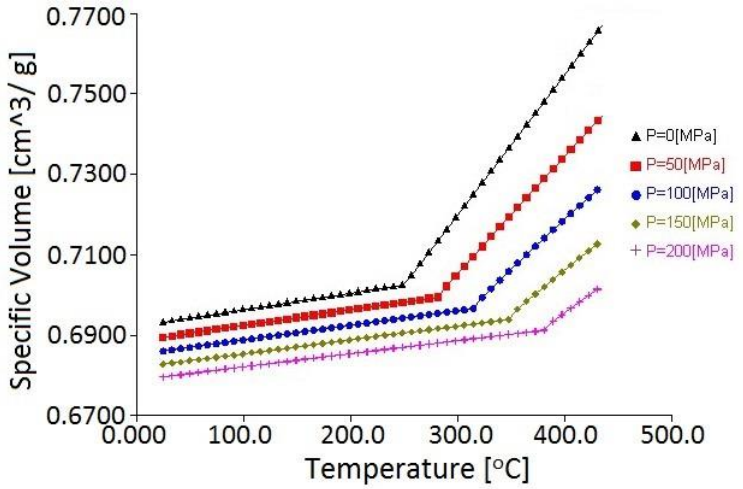

Fig. 4. The p-v-T graph for AURUM JCL3030 composite

5. The optimization of injection moulding parameters

The processing parameters have been optimized using Taguchi method. In the analysis the control factors were following: the melt temperature in the range of 400°C to 440°C, mold temperature in the range of 180°C to 220°C, injection time in the scope of 0.8 s to 1.2 s, holding time in the range 10-14 s and holding pressure in the scope of 70% - 90% of the injection pressure. Scopes of input parameters were based on the literature and material database of Autodesk Moldflow Insight 2013 commercial code.

As quality criteria, the volumetric shrinkage at ejection was selected. The optimization analysis was made through the design of the experiment, implemented in the program. Based on calculations, the impact of the main factors controlling the value of shrinkage was estimated. It was found that the melt temperature has the greatest impact on the quality criterion (fig. 5). Several important computer calculations have been conducted, which allowed to obtain optimal injection parameters: the melt temperature – 400°C, mold temperature -

220°C, injection time 0.8 s, holding pressure of 90% of the injection pressure and holding time 12 s. The lowest shrinkage value was received using these parameters. The range of optimum processing parameters vs. control parameters were illustrated by means of response surface method RSM (figs. 6-8).

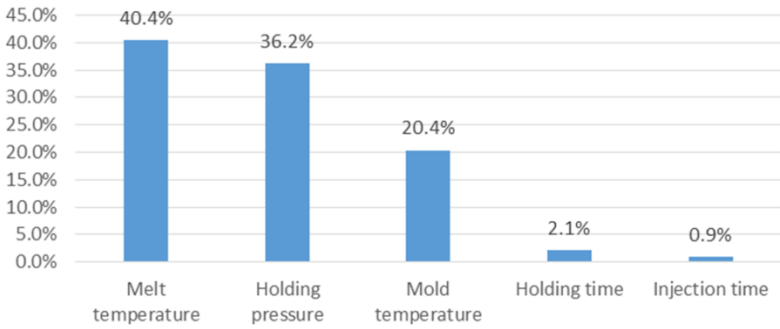

Fig. 5. Percentage impact of the main factors controlling the value of shrinkage at ejection

The analysis of numerical simulation results were focused on the basic process parameters, i.e. filling certainty of the mold cavity, fiber orientation and weld lines. Analyzing the composite flow it was found that the mold cavity was filled efficiently. Weld lines in the plastic gear molded piece are formed predominantly due to connection of the jet forming stream according to the complex structure of the part. In these places the decreasing of composite strength takes place. Weld lines created in the gear molded piece are shown in figure 9a. The most likely occurrence places of weld lines are in the vicinity of assembly holes.

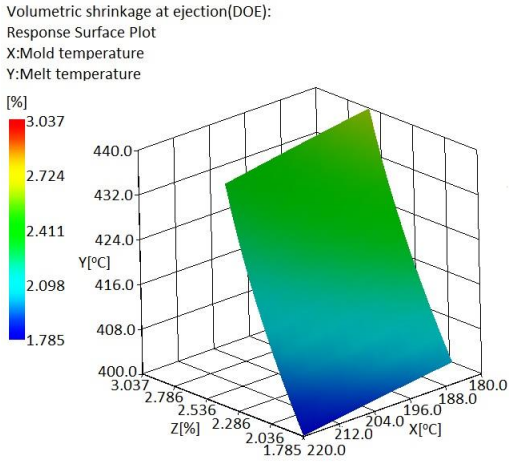

Fig. 6. RSM surface plots of volumetric shrinkage for factors: mold temperature and melt temperature

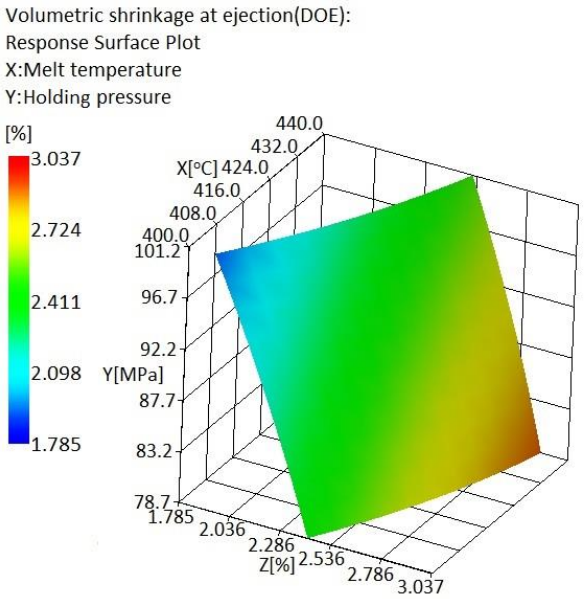

Fig. 7. RSM surface plots of volumetric shrinkage for factors: melt temperature and holding pressure

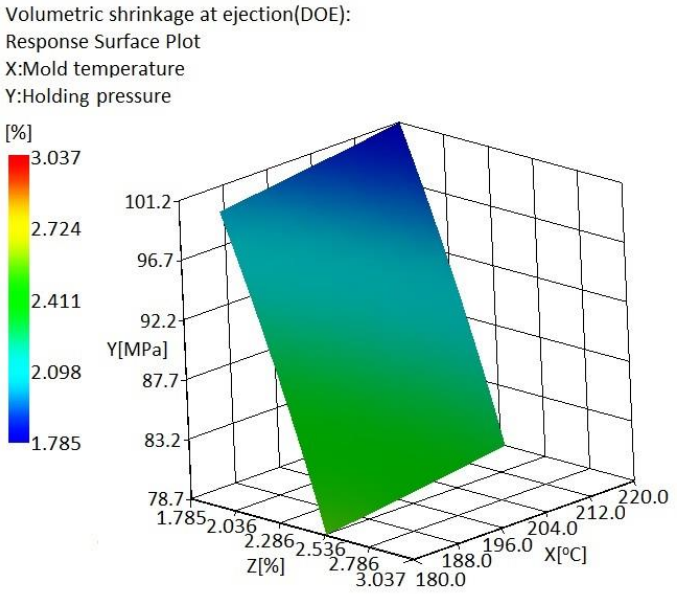

Fig. 8. RSM surface plots of volumetric shrinkage for factors: mold temperature and holding pressure

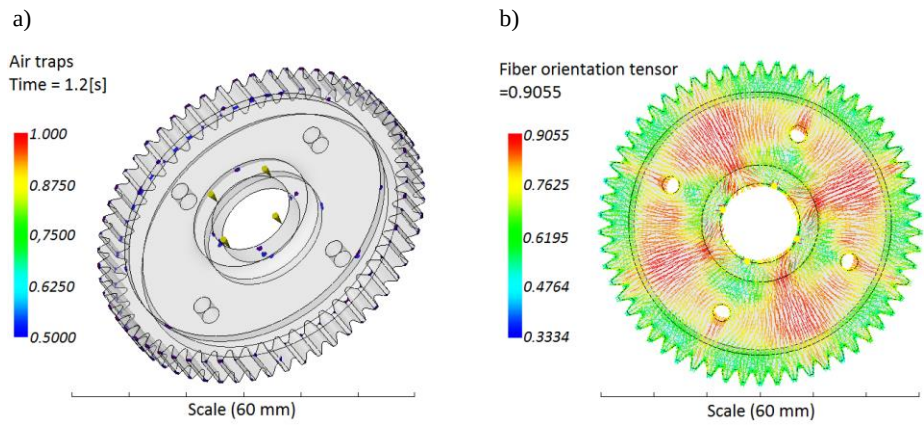

Fig. 9. Presentation: a) line connecting the composite, b) fiber orientation tensor

In the calculations of fiber orientation the Tucker - Folgar model was applied. It was used a numerical procedure that allows to calculate the coefficient of the interaction of the fibers and the polymer matrix. Elastic properties of composites reinforced with short fibers were calculated on the base of micromechanical Halpin-Tsai model. Elastic properties of the polymer matrix and fiber content and their shape factor were included. The unidirectional composite reinforcement was assumed. To determine the coefficients of thermal expansion: for both longitudinal and transverse direction, the Rosen-Hashine model was selected. Disorders of fibers orientation were undoubtedly associated with the change of molded piece geometry and polymer flow path (fig. 9b).

6. Conclusions

The results of the analysis of numerical simulations indicate that the specialized computer programs allow to predict phenomena in specific technological processes. Modern simulation commercial codes provide acceptably faithful representation of reality, assuming the correctness of initial and boundary conditions and the reliability of material data. In the case of non-standard plastic, as in the case of polyimide, we do not always have access to the target material and we do not have proper equipment to enable the manufacturing of such product. Due to the very interesting properties of the polyimide and its low popularity in use as an injection molding material, an analysis of injection molding process of the gear made from this composite was made. In this work the chosen material data necessary for numerical analysis were presented. The impact analysis of the main factors controlling the value on volumetric shrinkage during the injection mouldings was conducted. It was found that the greatest impact on the quality criterion was the melt temperature. Injection parameters were optimized using orthogonal Taguchi plans. It was also found that the processing parameters of

the polyimide determine to use of non-standard machines and equipment for processing by injection moulding technology.

Acknowledgement

The research leading to these results has received funding from the People Programme (Marie Curie International Research Staff Exchange) of the European Union's Seventh Framework Programme FP7/2007-2013/ under REA grant agreement n° PIRSES-GA-2013-610547.

References

[1] Berins M.L.: Plastics Engineering Handbook of the Society of the Plastics Industry, 5th ed., Chapman and Hall, New York 1991.

[2] Brydson J.A.: Plastics Materials, 6th ed., Butterworth-Heinemann, Oxford 1995.

[3] Budzik G., Bernaczek J., Kozik B., Sobolewski B., Sobolak M., Oleksy M., Grzelka M., Dobrowolska A.: Advanced integrated cad/rp systems in manufacturing process of planetary gear demonstrator, Acta Technica Corviniensis-Bulletin of Engineering, 6 (2013) 95.

[4] Chanda M., Roy S. K.: Plastics Technology Handbook, CRC Press, Boca Raton 2007.

[5] Gajdoš I., Duleba B., Spišák E., Greškovič F., Dulebová L.: Optimization of injection molding process by DOE, Hutnik - Wiadomosci Hutnicze, 81 (2014) 470- 475.

[6] Harper C.A.: Handbook of Plastics Technologies: The Complete Guide to Properties and Performance, McGraw-Hill, New York 2006.

[7] Harper C. A., Petrie, E. M.: Plastics Materials and Processes: A Concise Encyclopedia, Wiley, Berlin 2003.

[8] Kowalska B., Sikora R.: The effect of cooling time of the injection moldings on the therodynamic equation of state, Polimery, 48 (2003) 359-364.

[9] Kroschwitz, J.I.: Concise Encyclopedia of Polymer Science and Engineering, John Wiley and Sons, New York 1990.

[10] Kutz M.: Applied Plastics Engineering Handbook, William Andrew, 2011.

[11] Kwiatkowski D., Gnatowski A., & Nabiałek J.: Numerical analysis of residual stress and deformation of injection moulded parts manufactured from polymeric composite with different processing conditions. Kompozyty, 11 (2011) 294-298.

[12] Marciniec A., Budzik G., Sobolewski B., Grzelka M., Wieczorkowski M.: Ocena dokładności prototypów stożkowych kół zębatych z zastosowaniem CMM, Czasopismo Techniczne. Mechanika, 107 (2010) 73-80.

[13] AURUM® JCL3030 Thermoplastic Polyimide - Product data.

[14] AURUM® JCL3030 Thermoplastic Polyimide - Product data.

[15] Pötsch G., Michaeli W., Injection Molding. An Introduction, Carl Hanser Verlag, Munich 2008.

[16] Wilczyński K., Reologia w przetwórstwie tworzyw sztucznych, WNT, Warszawa 2001.

[17] Yang H., Liu J., Ji M., Yang S.: Novel thermoplastic polyimide composite materials, INTECH open science 2012, pp. 1-11.

PROBLEMATYKA WYTWARZANIA WYROBÓW TECHNICZNYCH Z KOMPOZYTÓW TYPU POLIIMID – WŁÓKNO WĘGLOWE W TECHNOLOGII FORMOWANIA WTRYSKOWEGO

S t r e s z c z e n i e

Współczesne programy symulacyjne w dość wierny sposób zapewniają odzwierciedlenie rzeczywistych procesów wytwarzania, przy założeniu poprawnie wprowadzonych warunków przeprowadzania procesu oraz danych przetwarzanego materiału. W przypadku nietypowych tworzyw sztucznych jakim jest m.in. poliimid – nie zawsze mamy dostęp do materiału oraz odpowiedniej aparatury w celu przetworzenia takiego wytworu. Z uwagi na bardzo interesujące właściwości poliimidu i małą popularność jako materiału nadającego się do wtryskiwania, wykonano symulację formowania wtryskowego koła zębatego wykonanego z kompozytu poliimid – włókno węglowe. W pracy zestawiono dane materiałowe niezbędne do przeprowadzenia analizy numerycznej. Dokonano analizy wpływu głównych czynników sterujących na wartość skurczu objętościowego wypraski. Stwierdzono, że największy wpływ na w/w kryterium jakościowe ma temperatura uplastycznionego tworzywa. Dokonano optymalizacji parametrów wtrysku z wykorzystaniem planów ortogonalnych Taguchi, w oparciu o które przeprowadzono analizy numeryczne. Ponadto, w oparciu o dostępną literaturę przedstawiono istotne właściwości poliimidu, jego aktualne możliwości przetwórstwa oraz obszary jego zastosowania jako materiału konstrukcyjnego.

Słowa kluczowe: poliimidy, kompozyty polimerowe, symulacje numeryczne, optymalizacja, formowanie wtryskowe

DOI: 10.7862/rm.2016.9

Otrzymano/received: 28.04.2016 r.
Zaakceptowano/accepted: 16.05.2016 r.

ZESZYTY NAUKOWE POLITECHNIKI RZESZOWSKIEJ 293, Mechanika 88
RUTMech, t. XXXIII, z. 88 (2/16), kwiecień-czerwiec 2016, s. 115-125

Piotr GIERLAK[1]

MODEL MATEMATYCZNY KARTEZJAŃSKIEGO MANIPULATORA WŁASNEJ KONSTRUKCJI

W referacie zaprezentowano opis matematyczny robota manipulacyjnego własnej konstrukcji. Robot o strukturze kinematycznej kartezjańskiej posiada trzy stopnie swobody. Sformułowano opis matematyczny kinematyki i dynamiki manipulatora. Do opisu kinematyki zastosowano notację Denavita-Hartenberga. Dynamiczne równania ruchu manipulatora uzyskano z zastosowaniem równań Lagrange'a drugiego rodzaju. W opisie dynamiki manipulatora uwzględniono dynamikę napędów. Dokonano analizy właściwości strukturalnych modelu matematycznego, które są wykorzystywane w syntezie algorytmów sterowania manipulatorami.

Słowa kluczowe: manipulator kartezjański, model manipulatora, kinematyka manipulatora, dynamika manipulatora, właściwości strukturalne modelu

1. Wprowadzenie

Do jednej z najpopularniejszych odmian manipulatorów należą manipulatory o strukturze kinematycznej kartezjańskiej. Powodem tego jest szeroka oferta rynku automatyki i robotyki w zakresie modułowych rozwiązań, zapewniających elastyczność podczas projektowania i konstruowania robotów do specjalizowanych zadań. Istotnymi zaletami manipulatorów kartezjańskich są: łatwość osiągnięcia dużej sztywności konstrukcji, prostota opisu kinematyki i dynamiki, łatwość wyznaczania przestrzeni roboczej i planowania w niej zadań. Prace badawcze dotyczące manipulatorów kartezjańskich prowadzone są głównie w zakresie budowy modeli matematycznych, w tym modeli uwzględniających podatność konstrukcji [4, 6] oraz sterowania manipulatorami kartezjańskimi z uwzględnieniem modeli matematycznych w prawie sterowania [3, 9].W praktyce przemysłowej stosowane są w większości manipulatory o stosunkowo prostej konstrukcji, dużej sztywności i dokładności pozycjonowania. Odpowiednia dokładność może być zapewniona przez zastosowanie śrub kulowych w układzie przeniesienia napędu [5].

W referacie zaprezentowano opis matematyczny robota manipulacyjnego własnej konstrukcji. Robot o strukturze kinematycznej kartezjańskiej posiada

[1] Autor do korespondencji/corresponding author: Piotr Gierlak, Politechnika Rzeszowska, al. Powst. Warszawy 12, 35-959 Rzeszów, tel.: (17) 8651854, e-mail: pgierlak@prz.edu.pl

trzy stopnie swobody. Jest przeznaczony m.in. do badań dotyczących robotyzacji procesów obróbki mechanicznej części maszyn. Wyposażony jest w tzw. moduły liniowe składające się z prowadnic i wózków napędzanych silnikami prądu stałego z wykorzystaniem przekładni zębatych oraz śrub kulowych. Manipulator wyposażony jest w enkodery zamocowane na wałach silników napędowych, czujnik siły umieszczony w końcówce i głowicę z napędem pneumatycznym, w której znajduje się narzędzie skrawające, np. pilnik, frez, itp.

Ze względu na fakt, że prezentowany robot nie jest produktem komercyjnym, lecz układem zbudowanym według własnego projektu autora, konieczne jest zaprojektowanie i wykonanie licznych modułów programowych służących do symulacji oraz programowania robota i sterowania nim. Celem pracy jest, zatem sformułowanie modelu matematycznego manipulatora, który posłuży do syntezy algorytmów sterowania manipulatorem. Model matematyczny jest również tworzony z myślą o zastosowaniu go w prawie sterowania manipulatorem. W związku z tym istotne jest zbadanie właściwości strukturalnych modelu matematycznego manipulatora. W rozdziale 2 przyjęto schemat modułów napędowych i zaprezentowano opis ich dynamiki. W rozdziale 3 przyjęto model manipulatora i przedstawiono równania kinematyki i dynamiki obiektu z uwzględnieniem dynamiki modułów napędowych. Kolejny rozdział dotyczy analizy właściwości strukturalnych modelu matematycznego. W ostatnim rozdziale dokonano podsumowania pracy.

2. Dynamika modułów napędowych

Manipulator zbudowany jest z elementów modułowych, którymi są napędy liniowe. Moduł napędowy liniowy składa się z prowadnicy z wózkiem, którego ruch jest wymuszany ruchem obrotowym śruby kulowej napędzanej silnikiem prądu stałego z przekładnią zębatą. Moduł liniowy schematycznie przedstawiono na rysunku 1. Równanie ruchu wirnika silnika zapisano zgodnie z oznaczeniami na rysunku 1 w postaci [1, 7]:

$$J_S \ddot{q}_S + B_S \dot{q}_S + M_1 = K_m i_W \tag{1}$$

gdzie: M_1 - moment obciążenia,
K_m - stała momentu,
i_W - prąd wirnika, (pozostałe oznaczenia objaśniono w podpisie rys. 1).

Równanie ruchu śruby kulowej z uwzględnieniem elementów przekładni to:

$$\left(J_{PR} + J_{SR}\right)\ddot{q}_{SR} + M_{O\,SR} + i_{SR} P = M_2 \tag{2}$$

gdzie: $M_{O\,SR}$ – moment oporów ruchu śruby,
$i_{SR} = \dot{q}/\dot{q}_{SR}$ – przełożenie przekładni śrubowej,

M_2 – moment napędzający od strony silnika.

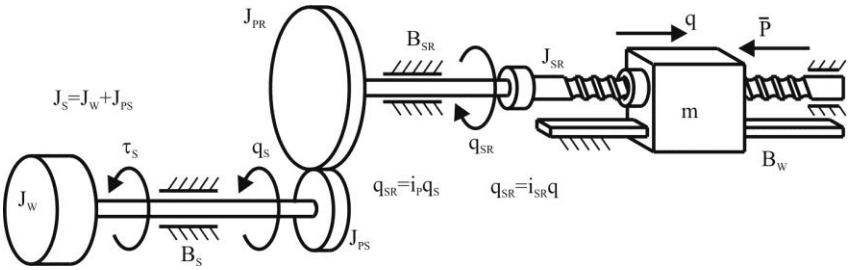

Rys. 1. Schemat modułu napędowego robota: J_W– masowy moment bezwładności wirnika silnika, J_{PS} – masowy moment bezwładności koła przekładni od strony silnika, J_{PR} – masowy moment bezwładności koła przekładni od strony wózka, J_S – masowy moment bezwładności modułu napędowego, J_{SR} – masowy moment bezwładności śruby, m – masa wózka oraz elementów znajdujących się na nim, $\tau_S = K_m i_W$ – moment generowany przez silnik, B_S – współczynnik oporów ruchu wirnika, B_{SR} – współczynnik oporów ruchu śruby i wału przekładni, B_W – współczynnik oporów ruchu wózka, q_S – kąt obrotu wirnika silnika, q_{SR} – kąt obrotu śruby, q - przemieszczenie wózka, i_P – przełożenie przekładni zębatej, i_{SR} – przełożenie przekładni śrubowej, P – siła zewnętrzna

Fig. 1. Scheme of robot's drive: J_W– mass moment of inertia of the motor shaft, J_{PS} – mass moment of inertia of the gear wheel from the side of drive, J_{PR} – mass moment of inertia of the gear wheel from the side of truck, J_S – mass moment of inertia of the drive, J_{SR} – mass moment of inertia of the screw, m – mass of the truck and items on it, $\tau_S = K_m i_W$ – the torque generated by the drive, B_S – coefficient of shaft motion resistance, B_{SR} – coefficient of motion resistance of screw gear shaft, B_W – coefficient of truck motion resistance, q_S –angle of rotation of the motor shaft, q_{SR} – angle of rotation of the screw, q–displacement of the truck, i_P – gear ratio, i_{SR} – helical gear ratio, P – external force

Zakładając równość mocy:

$$M_1 \dot{q}_S = M_2 \dot{q}_{SR} \tag{3}$$

i przełożenie:

$$\dot{q}_{SR} = i_P \dot{q}_S \tag{4}$$

równanie (1) zapisano w następującej postaci:

$$\left[J_S + \left(J_{PR} + J_{SR} \right) i_P^2 \right] \ddot{q}_S + B_S \dot{q}_S + i_P M_{O\,SR} = K_m i_W - i_P i_{SR} P \tag{5}$$

i uzyskano opis dynamiki modułu napędowego w funkcji kinematycznych parametrów ruchu wału silnika. Podobnie można zapisać równania ruchu pozostałych napędów i przedstawić je wszystkie w zwartej formie macierzowej:

$$\mathbf{J}\ddot{\mathbf{q}}_S + \mathbf{B}\dot{\mathbf{q}}_S + \mathbf{F}_{SR} = \mathbf{K}\mathbf{i}_W - \mathbf{i}\mathbf{P} \tag{6}$$

gdzie: $\mathbf{J}=diag\{J_1,J_2,J_3\}$ – macierz bezwładności, $J_j=J_{Sj}+(J_{PRj}+J_{SRj})i_{Pj}^2, j = 1, 2, 3$,
$\mathbf{q}_S=[q_{S1}, q_{S2}, q_{S3}]^T$ – wektor kątów obrotu wirników silników,
$\mathbf{B}=diag\{B_{S1}, B_{S2}, B_{S3}\}$ – macierz oporów ruchu wirników silników,
$\mathbf{K}=diag\{K_{m1}, K_{m2}, K_{m3}\}$ – macierz stałych momentowych silników,
$\mathbf{i}_W=[i_{W1}, i_{W2}, i_{W3}]^T$ – wektor prądów wirników,
$\mathbf{i}=diag\{i_{P1}i_{SR1}, i_{P2}i_{SR2}, i_{P3}i_{SR3}\}$ – macierz przełożeń przekładni,
$\mathbf{P}=[P_1, P_2, P_3]^T$ – wektor sił zewnętrznych,
$\mathbf{F}_{SR}=[i_{P1}M_{O\ SR1}, i_{P2}M_{O\ SR2}, i_{P3}M_{O\ SR3}]^T$ – wektor zredukowanych oporów ruchu śrub.

3. Kinematyka i dynamika manipulatora

Widok robota manipulacyjnego przedstawiono na rysunku 2, a schemat kinematyczny na rysunku 3. Przyjęto lokalne układy współrzędnych zgodnie z notacją Denawita-Hartenberga (DH) [7, 8] oraz bazowy układ odniesienia *xyz*. Parametry zestawiono w tabeli 1, gdzie zmienne przegubowe to l_j, j = 1, 2, 3. Ostatni układ odniesienia związano z końcówką roboczą (punkt D).

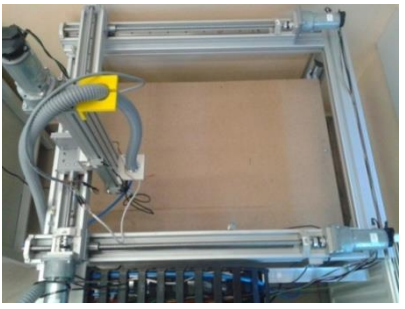

Rys. 2. Widok manipulatora
Fig. 2. The manipulator

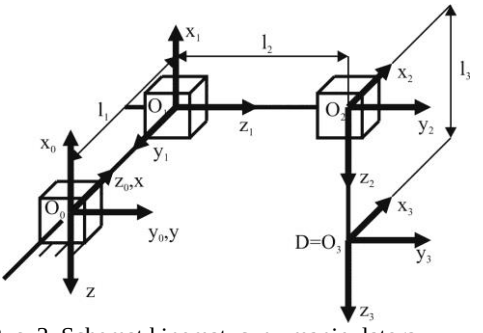

Rys. 3. Schemat kinematyczny manipulatora
Fig. 3. The kinematic diagram of the manipulator

Tabela 1. Parametry manipulatora wg notacji D-H
Table 1. Parameters of the manipulator according to D-H notation

j	a_j, m	α_j, rad	d_j, m	θ_j, rad
1	0	$3\pi/2$	l_1	0
2	0	$\pi/2$	l_2	$3\pi/2$
3	0	0	l_3	0

Uwzględniając dodatkowo rotację układu $x_0y_0z_0$ względem bazowego *xyz* określono macierz transformacji układu 3 do bazowego jako:

$$\mathbf{A} = \begin{bmatrix} 1 & 0 & 0 & l_1(t) \\ 0 & 1 & 0 & l_2(t) \\ 0 & 0 & 1 & l_3(t) \\ 0 & 0 & 0 & 1 \end{bmatrix} \tag{7}$$

Z powyższego wzoru wynika, że orientacja końcówki roboczej jest stała, a zmienne przegubowe l_j, które są funkcjami czasu, są wprost współrzędnymi kartezjańskimi końcówki w przestrzeni roboczej, tzn.:

$$\mathbf{p}_D = \begin{bmatrix} x_D(t) \\ y_D(t) \\ z_D(t) \end{bmatrix} = \begin{bmatrix} l_1(t) \\ l_2(t) \\ l_3(t) \end{bmatrix} \tag{8}$$

gdzie: $\mathbf{p}_D$ – wektor współrzędnych kartezjańskich końcówki manipulatora,

$x_D(t)$, $y_D(t)$, $z_D(t)$ – współrzędne końcówki manipulatora.

Natomiast prędkość końcówki roboczej to:

$$\mathbf{v}_D = \begin{bmatrix} \dot{x}_D(t) \\ \dot{y}_D(t) \\ \dot{z}_D(t) \end{bmatrix} = \begin{bmatrix} \dot{l}_1(t) \\ \dot{l}_2(t) \\ \dot{l}_3(t) \end{bmatrix} \tag{9}$$

W celu wyprowadzenia dynamicznych równań ruchu robota [2, 7, 10] zastosowano równania Lagrange'a II rodzaju, których postać dana jest wzorem:

$$\frac{d}{dt}\left(\frac{\partial E}{\partial \dot{q}_j}\right) - \frac{\partial E}{\partial q_j} = Q_j \tag{10}$$

gdzie: E – energia kinetyczna analizowanego układu,

q_j – współrzędna uogólniona,

Q_j – siła uogólniona odpowiadająca współrzędnej uogólnionej.

Energia kinetyczna układu to:

$$E = \frac{1}{2}\sum_{j=1}^{3} m_j v_j^2 \tag{11}$$

gdzie: m_j – masa j-tego członu,

v_j – prędkość środka masy j-tego członu,

Q_j – siła uogólniona odpowiadająca współrzędnej uogólnionej.

Prędkości poszczególnych członów to:

$$\begin{cases} v_1 = \dot{l}_1 \\ v_2 = \sqrt{\dot{l}_1^2 + \dot{l}_2^2} \\ v_3 = \sqrt{\dot{l}_1^2 + \dot{l}_2^2 + \dot{l}_3^2} \end{cases} \tag{12}$$

Założono, że na każdy człon działają następujące siły: siła P_j napędzająca człon działająca wzdłuż osi przegubu, siła oporu ruchu wózka po prowadnicy F_j oraz ciężar członu G_j działający wzdłuż osi z (rys. 4).

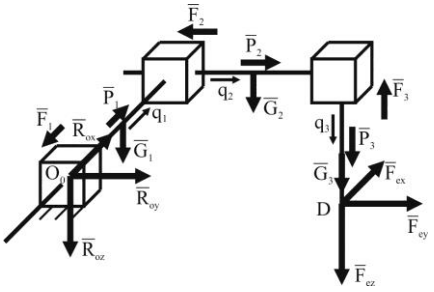

Rys. 4. Układ sił działający na manipulator

Fig. 4. The forces system acting on the manipulator

Ponadto w punkcie D działa na końcówkę roboczą siła zewnętrzna $\mathbf{F}_e=[F_{ex}, F_{ey}, F_{ez}]^T$, a w punkcie O_0 występują reakcje z ostoją. Zakładając współrzędne uogólnione jako $q_j=l_j$, wyznaczono siły uogólnione z zastosowaniem zasady prac przygotowanych porównując pracę przygotowaną sił uogólnionych z pracą przygotowaną działającego układu sił i otrzymano

$$\begin{cases} Q_1 = P_1 - F_1 + F_{ex} \\ Q_2 = P_2 - F_2 + F_{ey} \\ Q_3 = P_3 - F_3 + F_{ez} + G_3 \end{cases} \tag{13}$$

Uwzględniając równania (11)-(13) w (10) zapisano dynamiczne równania ruchu jako:

$$\begin{cases} (m_1 + m_2 + m_3)\ddot{l}_1 = P_1 - F_1 + F_{ex} \\ (m_2 + m_3)\ddot{l}_2 = P_2 - F_2 + F_{ey} \\ m_3\ddot{l}_3 = P_3 - F_3 + F_{ez} + G_3 \end{cases} \tag{14}$$

które wygodnie jest zapisać w postaci macierzowej:

$$\mathbf{M}\ddot{\mathbf{l}} = \mathbf{P} - \mathbf{F} + \mathbf{F}_e + \mathbf{G} \tag{15}$$

gdzie: $\mathbf{M}=diag\{m_1+m_2+m_3, m_2+m_3, m_3\}$ – macierz bezwładności,
$\mathbf{l}=[l_1, l_2, l_3]^T$ – wektor przemieszczeń uogólnionych,
$\mathbf{P}=[P_1, P_2, P_3]^T$ – wektor sił napędzających,
$\mathbf{F}=[F_1, F_2, F_3]^T$ – wektor sił oporów ruchu,
$\mathbf{G}=[0, 0, G_3]^T$ – wektor sił grawitacji.

Uwzględniając opis dynamiki układu (15) w równaniu (6), otrzymano:

$$\mathbf{J}_z\ddot{\mathbf{q}}_S + \mathbf{R} - \mathbf{iG} = \mathbf{K}\mathbf{i}_W + \mathbf{iF}_e \tag{16}$$

gdzie: $\mathbf{J}_z=\mathbf{J}+\mathbf{iMi}$ – macierz bezwładności członów robota,
$\mathbf{R} = \mathbf{B}\dot{\mathbf{q}}_S + \mathbf{F}_{SR} + \mathbf{iF}$ – wektor sumarycznych oporów ruchu.

Człon **R** uwzględniający opory ruchu, można modelować w różnorodny sposób. Powszechnie stosowanym modelem tarcia jest kombinacja modeli tarcia wiskotycznego i suchego. Model taki uzyskano zakładając elementy w wektorze $\mathbf{F}_{SR}$ w postaci:

$$M_{O\,SRj} = B_{SRvj}\dot{q}_{SRj} + B_{SRcj}\,\mathrm{sgn}(\dot{q}_{SRj}) \tag{17}$$

oraz elementy w wektorze oporów ruchu wózków **F** jako

$$F_j = B_{Wvj}\dot{l}_j + B_{Wcj}\,\mathrm{sgn}(\dot{l}_j) \tag{18}$$

gdzie: B_{SRvj} i B_{Wvj} – współczynniki oporu wiskotycznego ruchu śruby i wózka,

B_{SRcj} i B_{Wcj} – współczynniki oporu suchego ruchu śruby i wózka.

Grupując współczynniki występujące w równaniach ruchu otrzymano ostatecznie model dynamiki manipulatora w postaci równania (16) gdzie:

$$\begin{aligned}
\mathbf{J}_z &= \begin{bmatrix} p_1 & 0 & 0 \\ 0 & p_2 & 0 \\ 0 & 0 & p_3 \end{bmatrix} \\
\mathbf{R} &= \begin{bmatrix} p_4\dot{q}_{S1} \\ p_5\dot{q}_{S2} \\ p_6\dot{q}_{S3} \end{bmatrix} + \begin{bmatrix} p_7\,\mathrm{sgn}(\dot{q}_{S1}) \\ p_8\,\mathrm{sgn}(\dot{q}_{S2}) \\ p_9\,\mathrm{sgn}(\dot{q}_{S3}) \end{bmatrix} \\
\mathbf{G} &= \begin{bmatrix} 0 \\ 0 \\ p_{10} \end{bmatrix}
\end{aligned} \tag{19}$$

oraz:

$$\begin{cases} p_1 = J_1 + (m_1 + m_2 + m_3) i_{P1}^2 i_{SR1}^2 \\ p_2 = J_2 + (m_2 + m_3) i_{P2}^2 i_{SR2}^2 \\ p_3 = J_3 + m_3 i_{P3}^2 i_{SR3}^2 \\ p_4 = B_{S1} + B_{SRv1} i_{P1}^2 + B_{Wv1} i_{P1}^2 i_{SR1}^2 \\ p_5 = B_{S2} + B_{SRv2} i_{P2}^2 + B_{Wv2} i_{P2}^2 i_{SR2}^2 \\ p_6 = B_{S3} + B_{SRv3} i_{P3}^2 + B_{Wv3} i_{P3}^2 i_{SR3}^2 \\ p_7 = B_{SRc1} i_{p1} + B_{Wc1} i_{p1} i_{SR1} \\ p_8 = B_{SRc2} i_{p2} + B_{Wc2} i_{p2} i_{SR2} \\ p_9 = B_{SRc3} i_{p3} + B_{Wc3} i_{p3} i_{SR3} \\ p_{10} = m_3 g \end{cases} \tag{20}$$

Wartości parametrów modelu matematycznego zebrano w tabeli 2.

Tabela 2. Parametry manipulatora

Table 2. Parameters of the manipulator

Parametr	Jednostka	Wartość
p_1	kgm^2/s	$1.4236 \cdot 10^{-5}$
p_2		$7.0957 \cdot 10^{-6}$
p_3		$7.0957 \cdot 10^{-6}$
p_4	kgm^2/s	$2.8156 \cdot 10^{-5}$
p_5		$1.4078 \cdot 10^{-5}$
p_6		$1.4078 \cdot 10^{-5}$
p_7	Nm	0.0159
p_8		0.0079
p_9		0.0079
p_{10}	N	49.0500

4. Właściwości strukturalne modelu matematycznego

W tym rozdziale zaprezentowane zostaną właściwości strukturalne modelu matematycznego manipulatora [2, 11], których znajomość jest konieczna w syntezie algorytmów sterowania manipulatorami. Zostanie przeanalizowany model matematyczny określony równaniem (16). Jest to model matematyczny odpowiadający przypadkowi manipulatora sztywnego.

Właściwość 1. Macierz bezwładności $\mathbf{J}_z$ jest symetryczna, dodatnio określona i spełnia ograniczenie:

$$\sigma_{\min}(\mathbf{J}_z)\mathbf{I} \le \mathbf{J}_z \le \sigma_{\max}(\mathbf{J}_z)\mathbf{I} \tag{21}$$

gdzie: $\mathbf{I} \in R^{3\times3}$ – macierz jednostkowa,

$\sigma_{\min}(\mathbf{J}_z)$ –minimalna ściśle dodatnia wartość własna macierzy $\mathbf{J}_z$,

$\sigma_{\max}(\mathbf{J}_z)$–maksymalna ściśle dodatnia wartość własna macierzy $\mathbf{J}_z$.

Właściwość 2. Równanie dynamiki manipulatora jest liniowe względem parametrów, co zapisano:

$$\mathbf{Y}(\mathbf{q},\dot{\mathbf{q}},\ddot{\mathbf{q}})\mathbf{p} = \mathbf{K}\mathbf{i}_W + \mathbf{i}\mathbf{F}_e \tag{22}$$

gdzie: $\mathbf{Y}(\mathbf{q},\dot{\mathbf{q}},\ddot{\mathbf{q}}) \in R^{3\times10}$ – macierz regresji,

$\mathbf{p}=[p_1, p_2, p_3, p_4, p_5, p_6, p_7, p_8, p_9, p_{10}]^T$ – wektor parametrów modelu.

Macierz regresji ma postać:

$$\mathbf{Y}(\mathbf{q},\dot{\mathbf{q}},\ddot{\mathbf{q}}) =$$

$$\left[\begin{array}{c|c|c|c|c|c|c|c|c|c} \ddot{q}_{S1} & 0 & 0 & \dot{q}_{S1} & 0 & 0 & \operatorname{sgn}(\dot{q}_{S1}) & 0 & 0 & 0 \\ \hline 0 & \ddot{q}_{S2} & 0 & 0 & \dot{q}_{S2} & 0 & 0 & \operatorname{sgn}(\dot{q}_{S2}) & 0 & 0 \\ \hline 0 & 0 & \ddot{q}_{S3} & 0 & 0 & \dot{q}_{S3} & 0 & 0 & \operatorname{sgn}(\dot{q}_{S3}) & 1 \end{array}\right] \tag{23}$$

Właściwość 3. Wektor **iG** spełnia zależność:

$$\|\mathbf{iG}\| = i_{p3} i_{SR3} p_{10}, \tag{24}$$

Właściwość 4. Wektor **R** spełnia ograniczenie:

$$\|\mathbf{R}\| \le r_1 \|\dot{\mathbf{q}}_S\| + r_2 \sqrt{|\dot{q}_{S1}| + |\dot{q}_{S2}| + |\dot{q}_{S3}|} + r_3 \tag{25}$$

gdzie: $r_1 = \max\{p_4, p_5, p_6\}$,

$r_2 = \max\left\{\sqrt{2p_4p_7}, \sqrt{2p_5p_8}, \sqrt{2p_6p_9}\right\}$,

$r_3 = \sqrt{p_7^2 + p_8^2 + p_9^2}$.

Właściwość 5. Macierz przełożeń przekładni **i** jest stała, diagonalna i dodatnio określona.

Właściwość 6. Macierz stałych momentowych silników **K** jest stała, diagonalna i dodatnio określona.

5. Podsumowanie

W pracy zaprezentowano metodykę modelowania manipulatora kartezjańskiego z zastosowaniem równań Lagrange'a drugiego rodzaju i uwzględnieniem dynamiki napędów. W modelu matematycznym uwzględniono jedynie najważniejsze zjawiska fizyczne występujące podczas ruchu członów manipulatora, tzn. zjawisko bezwładności, opory ruchu, wpływ sił ciężkości oraz interakcję końcówki roboczej ze środowiskiem. Pominięto natomiast takie zjawiska jak np. deformacje członów, deformacje i luzy w układzie przeniesienia napędu czy drgania mechaniczne. Dzięki takiemu podejściu uzyskany model jest liniowy względem parametrów i wykazuje typowe właściwości strukturalne modeli matematycznych manipulatorów sztywnych [2]. Może być zastosowany w syntezie układu sterowania robotem.

Literatura

[1] Burghardt A. Giergiel J.: Modelling of mobile wheeled robot with dynamic drive compliance, Modelling Optimization Phys. Systems, 9 (2010) 7-12.

[2] De Wit C.C., Siciliano B., Bastin G.: Theory of Robot Control, Springer, London 1996.

[3] Elkady A.Y., Hanna S. N., Elkobrosy G. A.: On the modeling and control of the Cartesian parallel manipulator, in: Advances in Computer and Information Sciences and Engineering, Sobh T. (ed.), books.google.com 2008, pp. 90-96.

[4] Kim H.-S., Tsai L.-W.: Evaluation of a Cartesian parallel manipulator, in: Advances in Robot Kinematics, Lenarčič J., Thomas F. (eds.), Kluwer Academic Publishers, Norwell 2002.

[5] Maeda G. J., Sato K.: Practical control method for ultra-precision positioning using a ballscrew mechanism, Precision Eng., 32 (2008) 309-318.

[6] Pratiher B., Bhowmick S.: Nonlinear dynamic analysis of a Cartesian manipulator carrying an end effector placed at an intermediate position, Nonlinear Dynamics, 69 (2012) 539-553.

[7] Spong M.W., Vidyasagar M.: Dynamika i sterowanie robotów, WNT,Warszawa 1997.

[8] Tchoń K., Mazur A., Dulęba I., Hossa R., Muszyński R.: Manipulatory i roboty mobilne: modele, planowanie ruchu i sterowanie, AOW PLJ, Warszawa 2000.

[9] Yen P.-L., Lai C.-C.: Dynamic modeling and control of a 3-DOF Cartesian parallel manipulator, Mechatronics, 19 (2009) 390-398.

[10] Żylski W., Gierlak P.: Modelowanie ruchu wybranego manipulatora, Acta Mech. Automatica, 4 (2010) 112-119.

[11] Żylski W., Gierlak P.: Sterowanie ruchem nadążnym robotów manipulacyjnych, OW PRz, Rzeszów 2014.

THE MATHEMATICAL MODEL OF THE CARTESIAN ROBOTIC MANIPULATOR OF OWN DESIGN

S u m m a r y

In the paper, the mathematical model of the robotic manipulator of own design is presented. The Cartesian manipulator has three degrees of freedom. The mathematical description of kinematics and dynamics is formulated. The Denavit-Hartenberg notation for kinematics description is used. The dynamical equations of motion of the manipulator are obtained by using Lagrange's equations of the second kind. In the manipulator's dynamics description, the dynamics of the drives is taken into account. An analysis of the structural properties of mathematical model is presented. Proved properties are useful in the synthesis of control algorithms.

Keywords: the Cartesian manipulator, model of manipulator, manipulator kinematics, manipulator dynamics, structural properties of model

DOI: 10.7862/rm.2016.10

Otrzymano/received: 28.04.2016 r.
Zaakceptowano/accepted: 9.06.2016 r.

ZESZYTY NAUKOWE POLITECHNIKI RZESZOWSKIEJ 293, Mechanika 88
RUTMech, t. XXXIII, z. 88 (2/16), kwiecień-czerwiec 2016, s. 127-140

Daniel LICHOŃ[1]
Anna MIKOŁAJCZYK[2]
Łukasz KISZKOWIAK[3]
Tomasz ŁĄCKI[4]

IDENTIFICATION OF UAV STATIC AERODYNAMIC CHARACTERISTICS IN THE WATER TUNNEL BALANCE RESEARCH

This work presents the identification of static aerodynamic characteristics in the water tunnel experiments. The tested object was a scale model of unmanned aerial vehicle (UAV) target drone OCP-Jet. The research was performed in the water tunnel Rolling Hills Research Corporation model no. 2436, Military University of Technology, Warsaw. Water tunnel experiments allow to perform static and dynamic balance measurements, dye flow visualizations and PIV flow field measurements. The advantage of the use of the water tunnel are relatively inexpensive researches and the possibility to use small models manufactured with 3D printing technology. However, testing the flying objects in the water medium has limitations due to difficulties in satisfying the flow similarity criteria. In this paper the researches were focused on identification of the static aerodynamic characteristics with the use of balance measurements. The forces and moments characteristics were performed. The experimental results were compared with full scale aircraft characteristics, calculated with analytical methods and vortex lattice method.

Keywords: static aerodynamics characteristics, water tunnel, UAV, balance measurements, aerodynamics forces, aerodynamics moments

1. Introduction

Static aerodynamic characteristics includes important information about aerodynamic forces and moments acting on the aircraft in steady state flight condition. Determining of static characteristics is a key issue for the estimation of flying qualities such as flight performance, static stability and manoeuvrability. Therefore, the identification of static aerodynamics characteristics is a matter

[1] Autor do korespondencji/corresponding author: Daniel Lichoń, Rzeszow University of Technology, tel.: (+48) 17 743 2346, e-mail: d_lichon@prz.edu.pl

[2] Anna Mikołajczyk, Military University of Technology, e-mail: anna.mikolajczyk@wat.edu.pl

[3] Łukasz Kiszkowiak, Military University of Technology, e-mail: lkiszkowiak@wat.edu.pl

[4] Tomasz Łącki, Military University of Technology, e-mail: tomasz.lacki@wat.edu.pl

of experimental researches and numerical analysis. The tunnel researches and flight tests are used in the identification of aerodynamic characteristics and flight performance. Water tunnel measurement is a one of experimental methods in the aircraft research programme. The available publications [1-4] indicate the following advantages of water tunnel tests:

- researchers are relatively inexpensive,
- simplicity of manufacturing and modifying the test model with the use of 3D printing technology,
- static and dynamic balance measurements of forces and moments supported by three axial model manipulator,
- dye flow visualization,
- flow field measurements with PIV technology.

On the other hand there exist some limitations in researches of flying objects in water tunnel. Physical properties of water medium such as density, viscosity and compressibility are significantly different than in air medium case. It is problematic to satisfy flow similarity criteria. The Reynolds number achieved on models in the water tunnel is approximately two or three rows lower than for full scale airplane [1]. However, for micro aerial vehicles it is possible to meet Reynolds number criterion. The sound velocity in water is four times higher than in the air medium. Thus it is impossible to satisfy Mach number in researches [1].

In this work the balance measurements of static aerodynamic characteristics were performed. The research object was 1:8 scale model of UAV flying drone OCP-Jet [9]. The force (lift, drag and side) and moment (pitching, rolling and yawing) characteristics were measured. In order to verify the usefulness of experimental results the characteristics were calculated for full scale airplane. The calculation included analytical methods [10] and vortex lattice method with the use of "Tornado" software [11, 12]. The collected data was discussed in order to evaluate the usefulness and a range of use the water tunnel in the identification of the flying object characteristics.

2. Research facilities

The research was performed in the water tunnel Rolling Hills Research Corporation (RHRC) Model no. 2436 (fig. 1). The test section (fig. 1, item 7) is equipped with model support (fig. 1, item 8) that provides the rotational movement along three axes. The measurement system includes five component strain balance (fig. 2), flow velocity meter and computer control unit. The strain balance is mounted inside the model and connects the model with manipulator support. The visualisation system consists of 6 independent dye tanks. The dye is distributed into the model airframe nozzles or external mobile nozzle. Additionally 2-dimensional PIV measurement are performed.

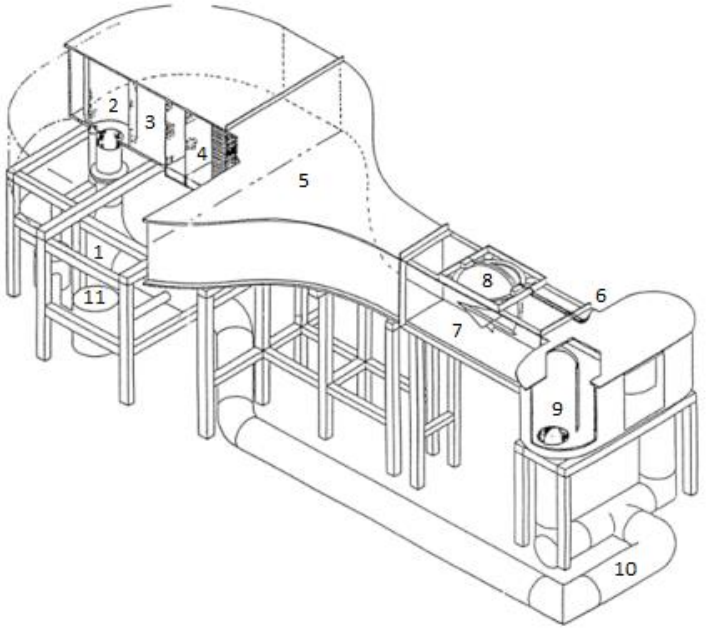

Fig. 1. RHRC 2436 water tunnel layout: 1 - pump, 2 - perforated inlet, 3 - delivery plenum, 4 - flow conditioning elements, 5 - contraction section, 6 - dye lines, 7 - test section, 8 - model support, 9 - discharge plenum, 10 - return piping, 11 - filter system

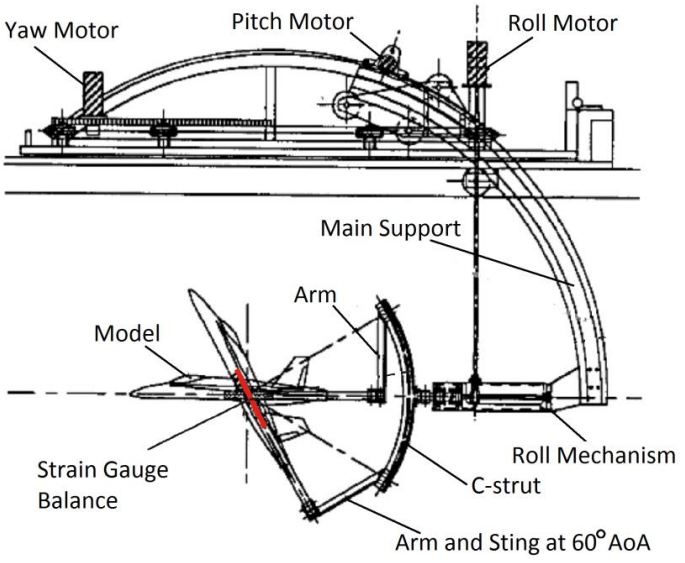

Fig. 2. Model manipulator (up) and strain balance (down) scheme

Table 1. Specifications of RHRC 2436 water tunnel, model support manipulator and strain balance

Water tunnel	
Overall dimensions	6.1 m x 2.5 m x 12.2 m
Water capacity	18 m^3
Flow velocity	0-0.3 m
Test section dimensions	0.6 m x 0.9 m x 1.8 m
Turbulence intensity	< 1.0 % RMS
Water pomp motor	7.5 KM 230V AC 3-phase 60Hz 30 A
Model support manipulator	
Type of movements	Three axes rotation
Pitch; yaw; roll angle (min/max)	-10°/36°; -25°/25°; -520°/520°
Pitch; yaw; roll rate (max)	15 [deg·s^{-1}]; 15 [deg·s^{-1}]; 40 [deg·s^{-1}]
Pitch; yaw; roll acceleration (max)	5 [deg·s^{-2}]; 2 [deg·s^{-2}]; 2 [deg·s^{-1}]
Strain balance	
Measured values	Normal (N) and side (Y) forces, pitching (PM), yawing (YM) and rolling (RM) moments
Size (diameter x length)	0.75 in x 3.75 in (without waterproof cover and mount adapters)
Number of channels (sections)	Total = 5 (2x PM, 2x YM, 1x RM)
Type of strain gage (for each section)	4x 1000Ω semi-conductor gauge arranged in full Wheatstone bridge
Maximum loading Pitch/yaw/torque	15 in·lb / 4 in·lb / 2.5 in·lb

3. Test model

The tested object is target drone OCP-Jet (MSP Company). For the research the 1:8 scale model was manufactured with the use of rapid prototyping technology. The article contains necessary technical data, for the full specification see [9]. Note that scaled model has modified aft fuselage part (fig. 3ab). The balance is mounted inside the model and must be inserted through the widen circular cross section.

Table 2. Specifications of OCP-Jet tested model (selected technical data)

Name	Full scale OCP-Jet	Research model (1:8 scale)
Wing span, mm	2855	356.9
Wing area, cm^2	13500	210.94
Planform area*, cm^2	22440	350.63
MAC, mm	459.2	57.4
Length, mm	3555	444.4
Height, mm	820	102.5
Reference point	25% MAC	25% MAC

* Airplane top view overall area

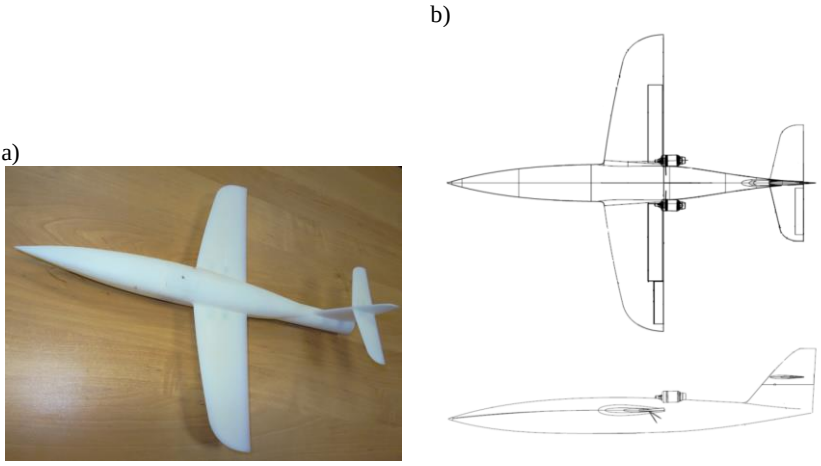

Fig. 3. View (a) and drawing (b) OCP-Jet tested model

The experiment consists of preparing the model, where the model is mounted and levelled along the flow direction in the test section. Considering the sensitivity of balance sensors the next step relies on balance tare in order to eliminate negative effect of model buoyant and weight force. After stabilizing the flow velocity (exact to a 0.02 in/s) the final measurement of hydrodynamic forces and moments is performed.

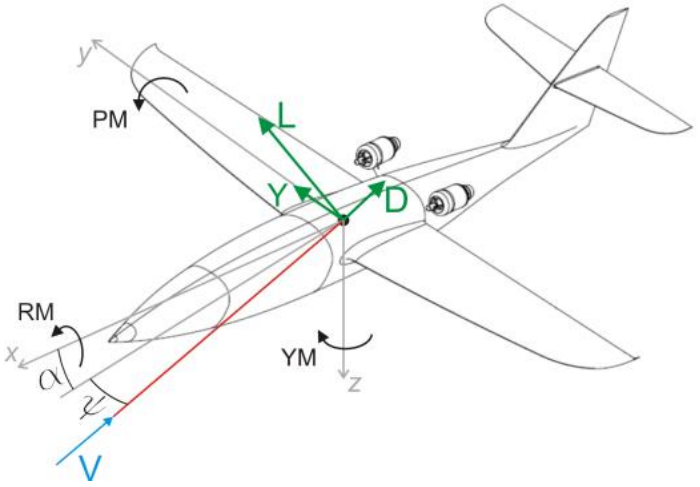

Fig. 4. Components of measured forces and moments

The model was tested with the angle of attack sequence (from $\alpha = 0°$ to $\alpha = 34°$, $\Delta\alpha = 2°$) in three configurations of yaw angle ($\psi = 0°, 10°, 20°$). Water flow velocity was set to V = 0.3 m/s. The components of hydrodynamic

force (lift, drag, side) and hydrodynamic moment (pitch, roll, yaw) were measured. Results are shown as a characteristics of forces and moments (in imperial units) and its coefficients due to the angle of attack. This is common form of flying object.

4. Discussion

The main problem of usefulness of experimental results is the fact that the model of flying object was tested in water medium. There are significant differences between properties of air and water. The density and kinematic viscosity of water are suitably $\rho_{water} = 999.1$ kg/m^3 and $\nu_{water} = 1.142 \cdot 10^{-6}$ m^2/s while the air parameters are $\rho_{air} = 1.225$ kg/m^3 and $\nu_{air} = 1.45 \cdot 10^{-5}$ m^2/s. Thus Reynolds number was different in the model and in the full scale object and equals suitably: $Re_{model,\ V=0.3\ m/s} = 1.2 \cdot 10^4$ and $Re_{object,\ V=75m/s} = 2.4 \cdot 10^6$. The experimental data characteristics was compared with the full scale aircraft characteristics. The classical method [10] and "Tornado" vortex lattice method (VLM) software [11, 12] were used to obtain full scale airplane characteristics.

The measured force characteristics (figs. 5 to 8) has expected run for airplane case. It can be clearly seen that in the practical angle of attack (AoA) range the lift characteristics $C_L(\alpha)$ is linear. Drag characteristics $C_D(\alpha)$ and polar $C_L(C_D)$ exhibit square dependency due to induced drag influence.

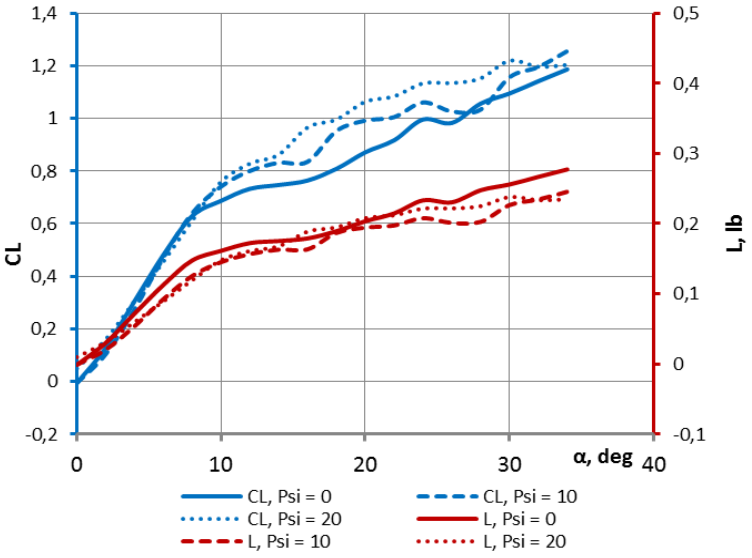

Fig. 5. Lift force characteristics

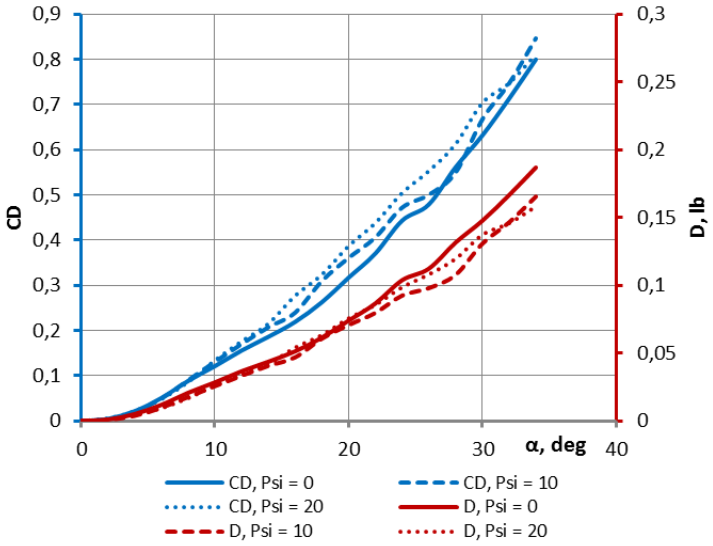

Fig. 6. Drag force characteristics

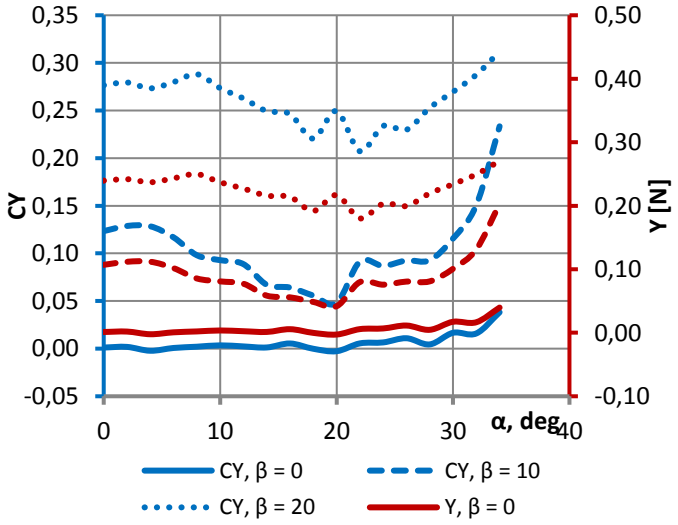

Fig. 7. Side force characteristics

Furthermore, the $C_L(\alpha)$ characteristics obtained with analytical methods and VLM method (fig. 15) in the linear range has virtually the same run. The lift curve slope is $\frac{dC_L}{d\alpha} = 4.35$ for experimental and analytical results and $\frac{dC_L}{d\alpha} = 4.87$ for VLM method. The difference for VLM method is caused by the lack of fuselage body influence on the main wing (VLM software [12] does not consider the

body, see fig. 18). In the range above linear dependence of lift curve slope it can be seen that water tunnel characteristics shows corrugated increment of lift coefficient without a stall point. The interpretation is that the water tunnel balance measures only the normal force that is separated geometrically on lift and drag component. Therefore, on higher AoA the normal force increases due to increasing model planform area crosswise the flow direction (fig. 2).

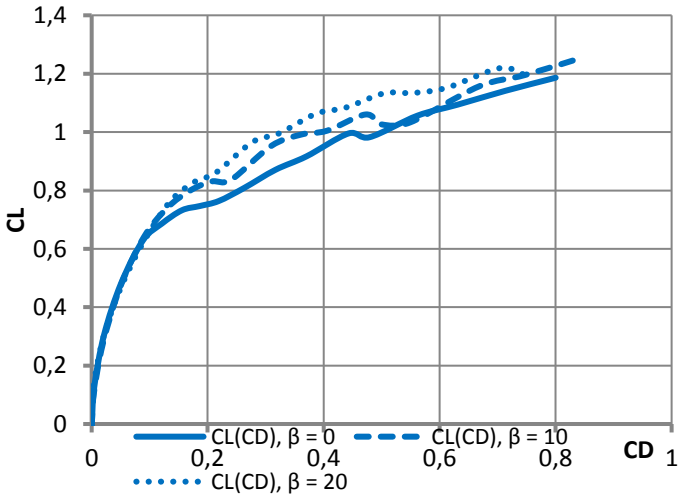

Fig. 8. Force coefficient polar

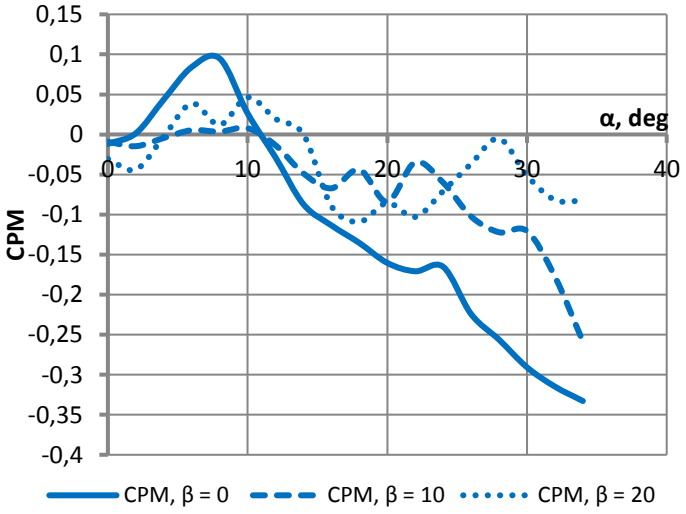

Fig. 9. Pitching moment coefficient characteristics

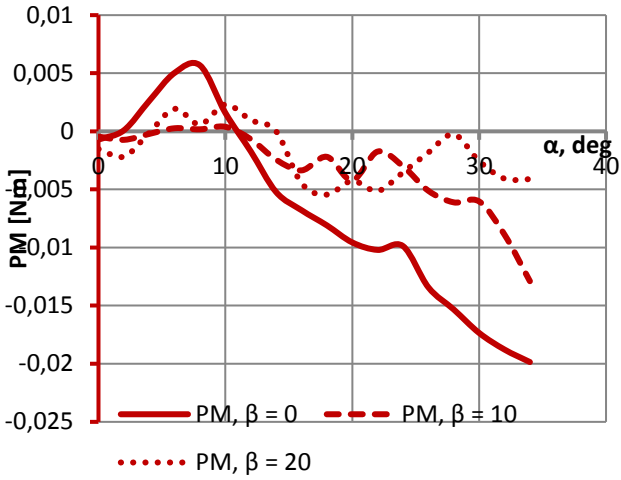

Fig. 10. Pitching moment characteristics

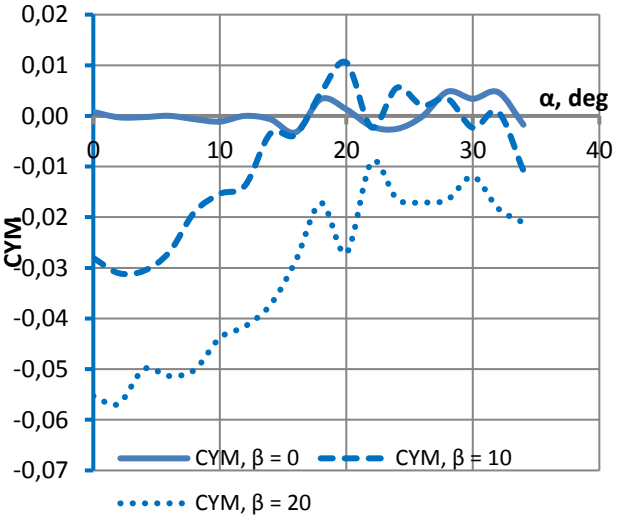

Fig. 11. Yawing moment coefficient characteristics

In a case of drag coefficient characteristics there is significant discrepancy between experiment and other methods. Considering the characteristics $C_L^2 = f(C_D)$ (fig. 16) it can be seen that the static derivative in linear range of $C_L(\alpha)$ dependence equals $\frac{dC_L^2}{dC_D} = 4.33$ for experimental results while for other methods the average value is $\frac{dC_L^2}{dC_D} = 17.4$. The probable cause of the difference is the fact that the drag coefficient in the experiment is identified indirectly by geometrical

separating the normal force on force and drag components. Therefore, increasing model planform area across the flow direction results in increasing measured drag force. As it was expected, experimental moment characteristics displays aerodynamic configuration for aircraft with classical rear tail. The average value of pitching moment coefficient derivative due to AoA remains negative $\frac{dC_m}{d\alpha} < 0$, that indicates positive longitudinal static stability characteristic (figs. 9, 10).

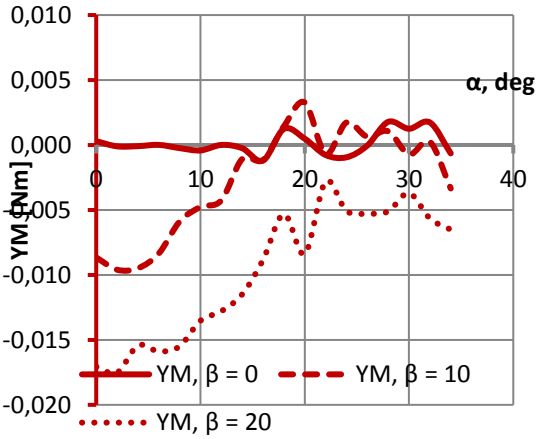

Fig. 12. Yawing moment characteristics

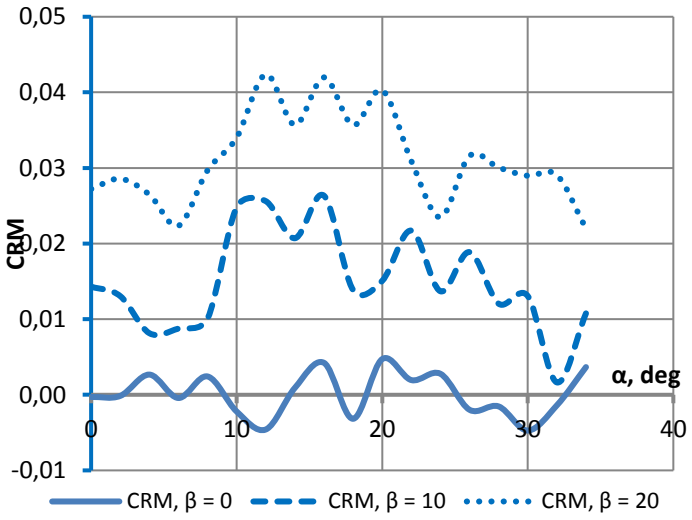

Fig. 13. Rolling moment coefficient characteristics

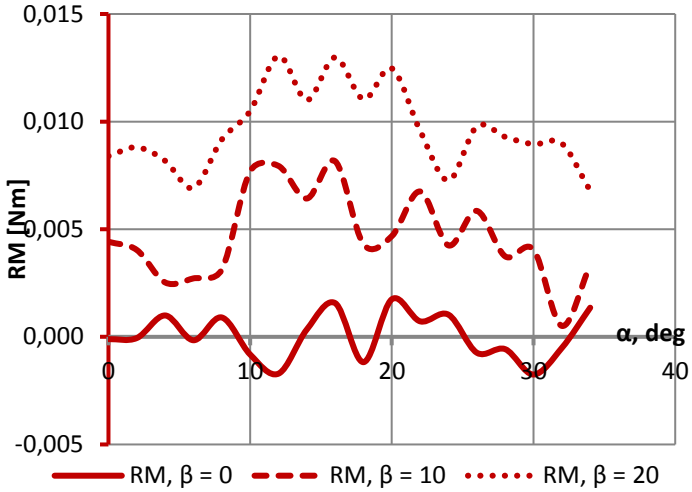

Fig. 14. Rolling moment characteristics

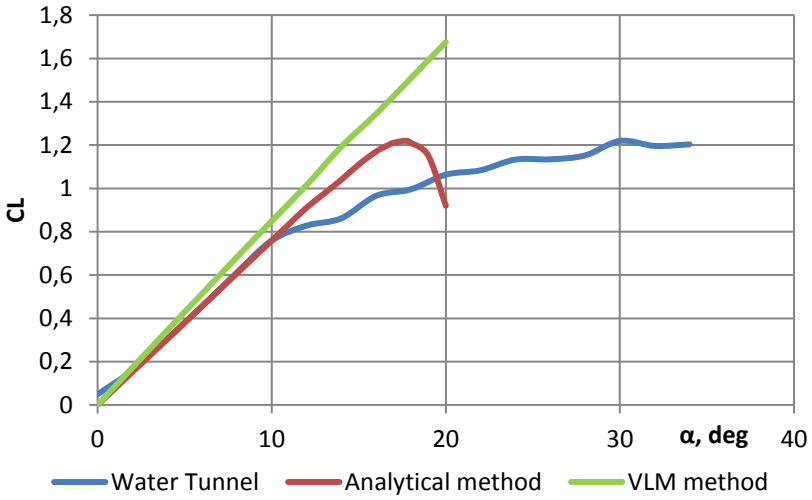

Fig. 15. Comparison of force characteristics $C_L(\alpha)$

5. Conclusion

Comparison of experimental results with calculated characteristics (fig. 17) shows discrepancy between experimental and VLM method results. It is caused by the lack of fuselage body in VLM modelling. In this case the analytical $C_m(\alpha)$ characteristic for the whole aircraft and wing-tail was shown separately. The analytical characteristics overlap with experimental and VLM runs. The only

problematic part of experimental $C_m(\alpha)$ run is at AoA less than $\alpha<8°$ where $\frac{dC_m}{d\alpha} > 0$. The probable reason is an influence of the main wing hydrodynamic shadow on the horizontal tail. Rolling and yawing moment characteristics (fig. 11 to 14) point that tested aircraft has positive static lateral stability characteristics. The measured values of pitching and rolling coefficients increase with yawing angle increment due to vertical tail influence.

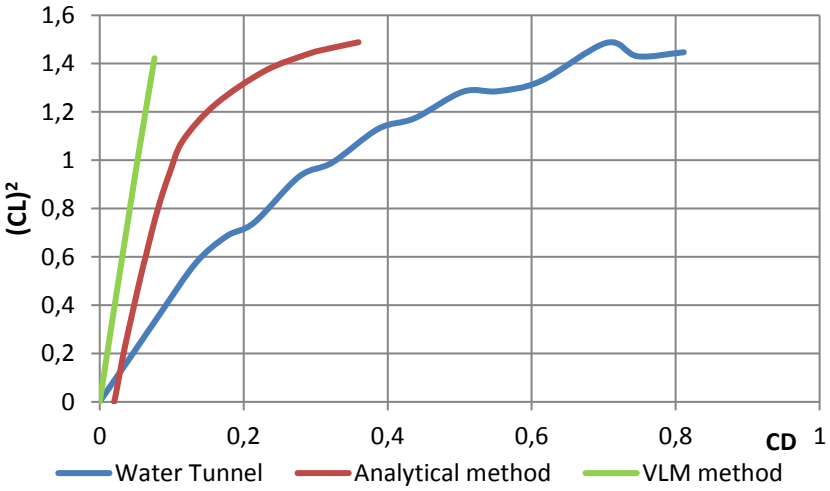

Fig. 16. Comparison of force polar characteristics $C_L(C_D)$

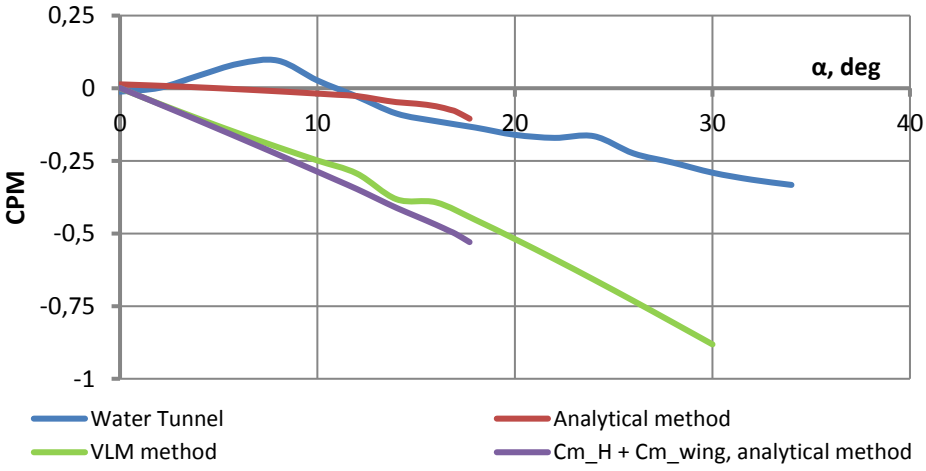

Fig. 17. Comparison of pitching moment characteristics $C_{PM}(\alpha)$

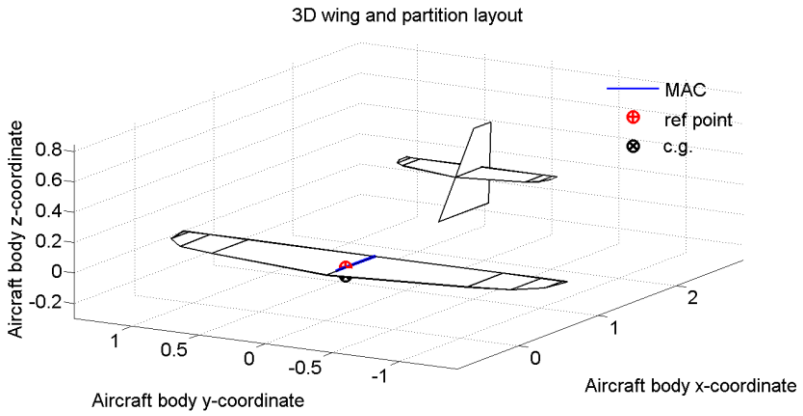

Fig. 18. Tornado VLM full scale model geometry

Acknowledgement

The article has been written within the confines of training period at The Faculty of Mechatronics and Aeronautical Engineering, Military University of Technology, Warsaw. The researches have been performed with the use of Aircraft Propulsion Laboratory (Laboratorium Badań Napędów Lotniczych) facilities.

References

[1] Erm L. P., Ol M.V.: An assessment of the usefulness of water tunnels for aerodynamic investigations, Defence Science and Technology Organization, DSTO-TR-2803, Australia, December 2012.

[2] Erm L. P., Ferrarotto P.: Development of a five-component strain-gauge balance for the DSTO water tunnel, Defence Science and Technology Organization, DSTO-TR-0597, Australia, November 2009.

[3] Erm L. P.: Development and use of a dynamic-testing capability for the DSTO water tunnel, Defence Science and Technology Organization, DSTO-TR-1836, Australia, March 2006.

[4] Erm L. P.: Measurement of flow-induced pressures on the surface of a model in a flow visualization water tunnel, Experiments in Fluids, 35 (2003), 533-540.

[5] Jaroszewicz A., Stachów J., et al.: Water tunel experimental studies of leading edge vortex control on delta wing MAV, 49th AIAA Aerospace Sciences Meeting, AIAA 2011-1158, Orlando, January 2011.

[6] Czekałowski P., Sibilski K., Szczepański C.: Wpływ zredukowanej częstotliwości trzepotania skrzydła entomoptera na obciążenia aerodynamiczne – wizualizacja opływu skrzydla oraz pomiary sił aerodynamicznych, Modelowanie Inżynierskie, 41 (2011), 27-37.

[7] Mueller T. J.: Aerodynamic measurements at low Reynolds numbers for fixed wing micro-air vehicles, Development and operation of UAVs for military and civil applications, Belgium, 1999.

[8] http://www.rollinghillsresearch.com

[9] http://www.uav.com.pl
[10] Fiszdon W.: Mechanika lotu, PWN, Warszawa, 1961.
[11] Melin T.: A vortex lattice Matlab implementation for linerar aerodynamic wing applications, Royal Institute of Technology, Sweden, 2000.
[12] Melin T.: Tornado VLM software, tornado.redhammer.se

IDENTYFIKACJA STATYCZNYCH CHARAKTERYSTYK AERODYNAMICZNYCH SAMOLOTU KLASY BAL Z WYKORZYSTANIEM POMIARÓW WAGOWYCH W TUNELU WODNYM

S t r e s z c z e n i e

W niniejszej pracy przeprowadzono eksperymentalną analizę zmęczeniową łopatki sprężarki lotniczego silnika turbinowego. Rozkład temperatur na łopatce wykorzystano do określenia długości powstałej w trakcie badań szczeliny zmęczeniowej. Łopatka z karbem symulującym uszkodzenie obcym obiektem została poddana drganiom poprzecznym wstanie rezonansu. Podczas badań zarówno amplituda przemieszczenia wierzchołka ostrza, a także długość pęknięcia były monitorowane. W tym samym czasie wykonano kamerą termowizyjną zdjęcia rozkład temperatury. W pierwszej fazie pracy wykresy amplitudowo-częstotliwościowe uzyskano dla różnej wielkości pęknięć. Określono liczbę cykli obciążeń do inicjacji pęknięć, a także dynamikę wzrostu pęknięć w łopatce sprężarki narażonej na drgania. Dodatkowym efektem pracy jest porównanie długości szczelin zmierzonych bezpośrednio na badanej łopatce jak i na obrazie z rozkładami temperatury wokół pęknięcia. Przedstawiono zalety metody pomiaru długości szczeliny z wykorzystaniem zdjęć z kamery termowizyjnej. Wyniki przedstawione w niniejszym artykule mają wartość teoretyczną i praktyczną.

Słowa kluczowe: statyczne charakterystyki aerodynamiczne, tunel wodny, BAL, pomiary wagowe, siły aerodynamiczne, momenty aerodynamiczne

DOI: 10.7862/rm.2016.11

Otrzymano/received: 10.04.2016 r.
Zaakceptowano/accepted: 14.06.2016 r.

ZESZYTY NAUKOWE POLITECHNIKI RZESZOWSKIEJ 293, Mechanika 88
RUTMech, t. XXXIII, z. 88 (2/16), kwiecień-czerwiec 2016, s. 141-152

Bartosz PRZYBYŁA[1]
Zbigniew ZAPAŁOWICZ[2]

USZKODZENIA SPRĘŻARKI ODŚRODKOWEJ SILNIKA LOTNICZEGO P&W 206 b2 SPOWODOWANE ZASSANIEM CIAŁ OBCYCH

W artykule przedstawiono najczęściej występujące uszkodzenia sprężarek odśrodkowych silników P&W 206b2 zamontowanych w śmigłowcach EC-135, eksploatowanych przez Lotnicze Pogotowie Ratunkowe. Uszkodzenia te są następstwem pracy tych silników w pasie nadmorskim, lądowaniami na podłożu piaszczystym np. plaży i zassaniem przez nie ciał obcych, takich jak m.in.: piasek, kurz, kropelki wody. Zanieczyszczenia występujące w zasysanym powietrzu powodują zmiany parametrów eksploatacyjnych silnika. Z kolei na ich podstawie można ocenić stan techniczny eksploatowanego silnika. W pracy omówiono także metodę oceny uszkodzeń elementów sprężarki oraz podano sposób ich naprawy.

Słowa kluczowe: silnik lotniczy, sprężarka odśrodkowa, uszkodzenia sprężarki

1. Wstęp

Sprężarka odśrodkowa jest zasadniczym elementem silnika lotniczego zamontowanym, na wspólnym wale, między wlotem a turbiną gazową. Zadaniem sprężarki jest dostarczyć, w sposób ciągły i nieprzerwany, odpowiednią ilość powietrza do komory spalania oraz powietrza do napędu agregatów połączonych na stałe z przekładnią redukcyjną. Ponadto sprężarka powinna dostarczyć odpowiednią ilość powietrza chłodzącego w celu obniżenia temperatury gorących elementów silnika oraz powietrza służącego do uszczelnienia miejsca wyjścia wału napędowego silnika. Sprężarka zapewnia także powietrze dające sygnał sterujący dla modułu zasilania paliwem FMM (Fuel Management Module). Sprężarka powinna również zasilać kabinę załogi w świeże powietrze - układ wentylacji. Wymagania, jakie stawia się sprężarkom są, więc następujące: wytworzyć odpowiedni spręż i natężenie przepływu, charakteryzować się wysoką

[1] Autor do korespondencji/corresponding author: Bartosz Przybyła, Zachodniopomorski Uniwersytet Technologiczny, al. Piastów 19, 70-310 Szczecin, Tel. 91 449 42 72, e-mail: bartosz.przybyla@zut.edu.pl
[2] Zbigniew Zapałowicz, Zachodniopomorski Uniwersytet Technologiczny, e-mail: zbigniew.zapalowicz@zut.edu.pl

sprawnością przez cały okres eksploatacji silnika (około 80% - 90%), wykazywać się ciągłą, nieprzerwaną oraz stateczną pracą, posiadać odporność na wysokie obroty silnika. Sprężarka silnika P&W 206b2 jest jednostopniową sprężarką odśrodkową (rys. 1), jej spręż wynosi Π_S^* = 8,2, strumień masy powietrza, jaki zasysa silnik jest równy $\dot{m}$ = 2,035 kg/s, a obroty nominalne wału wynoszą n = 58000 obr/min [1].

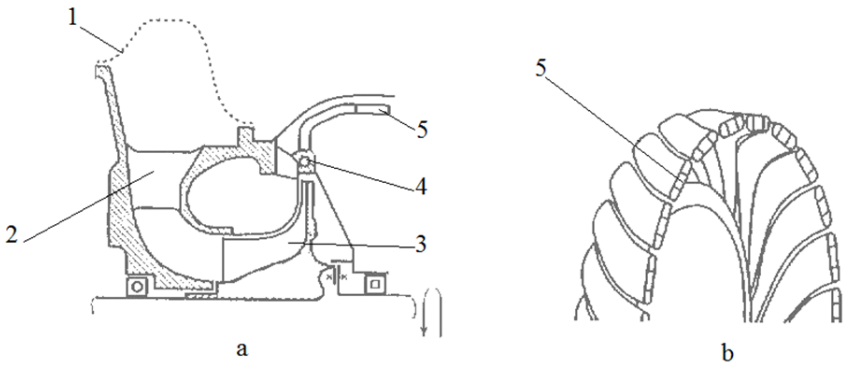

Rys.1. Schemat konstrukcyjny sprężarki silnika PW 206b2: 1 - siatka zabezpieczająca wlot, 2 - łopatki wlotowe, 3 - wirnik, 4 - wlot do dyfuzora rurkowego, 5 - wylot dyfuzora rurkowego

Fig. 1. Construction scheme of a compressor of the PW 206b2 engine: 1 - intake protective mesh, 2 - inlet ribs, 3 - rotor, 4 - inlet to the pipes diffuser, 5 - diffuser pipes outlet

Sekcja sprężarki składa się z następujących elementów konstrukcyjnych: wlotu, wirnika i dyfuzora. Zadaniem wlotu jest ukierunkowanie strumienia powietrza napływającego do sprężarki. Wlot wykonany jest ze stopu aluminium. Wyposażono go w 6 podpór, w których poprzez specjalnie wydrążone otwory przepływa olej silnikowy oraz paliwo. Takie rozwiązanie konstrukcyjne chroni wlot do silnika przed oblodzeniem. W podporach znajdują się też szczeliny do odprowadzania powietrza (regulacja upustowa), co pozwala zwiększyć granicę obszaru statecznej pracy sprężarki. Wirnik wykonany jest ze stopu tytanu. Ze względu na wirowanie jest elementem najbardziej narażonym na uszkodzenia spowodowane zasysaniem ciał obcych. W związku z tym jego żywotność jest ograniczona przez ilość cykli pracy sprężarki bądź też przez rodzaj możliwych jej uszkodzeń. Rozbieżny dyfuzor (rys. 2) składa się z elementów spawanych oraz frezowanych, wykonanych ze stopów stali, połączonych z 22 kanałami. Jego zadaniem jest zwiększenie ciśnienia statycznego powietrza na wylocie ze sprężarki kosztem zmniejszenia jego prędkości. Spośród wszystkich elementów składowych silnika turbinowego wirnik sprężarki jest elementem najbardziej narażonym na uszkodzenia. Jednocześnie jego konstrukcja i konstrukcja sprężarki muszą być odpowiednio lekkie, wytrzymałe oraz precyzyjnie wykonane. Na elementy sprężarki działają obciążenia, które są wywołane:

– zginaniem i skręcaniem, pochodzącym od przepływającego strumienia powietrza,
– rozciąganiem łopatek, spowodowanym działaniem siły odśrodkowej,
– drganiami wynikającymi z niewyważenia bądź uszkodzenia wirnika.

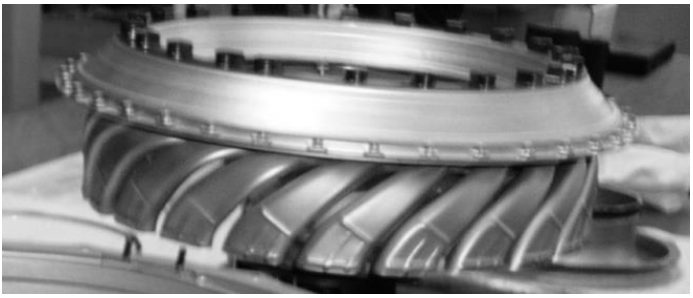

Rys. 2. Dyfuzor silnika P&W 206 b2 (fot. P. Rutkowski)

Fig. 2. Diffuser of the P&W 206 b2 engine (photo P. Rutkowski)

2. Rodzaje uszkodzeń elementów sprężarki

Śmigłowce LPR, wykonując misje ratunkowe bądź transportowe, często są narażone na pracę w trudnych warunkach. Stosunkowo krótkie loty, przy jednoczesnej dużej ich liczbie, powodują, że silniki, a w szczególności sprężarki, są bardzo mocno narażone na uszkodzenia wywołane oddziaływaniem ciał obcych (rys. 3). Szczególnie lądowania/starty na podłożu piaszczystym (np. podczas lotów ratunkowych w pasie nadmorskim), sprzyjają dostawaniu się do silników drobinek piasku, które przy długotrwałym oddziaływaniu, znacznie przyspieszają proces erozji łopatek wirnika sprężarki. Spośród wszystkich występujących rodzajów uszkodzeń sprężarek, najważniejsze to:

– wyszczerbienia krawędzi natarcia/spływu łopatek (rys. 4),
– wgniecenia krawędzi natarcia/spływu powierzchni łopatek (rys. 5),
– rozerwania łopatek (rys. 6),
– zniekształcenia geometrii łopatki (rys. 7),
– pęknięcia łopatek (rys. 8),
– uszkodzenia erozyjne łopatek - powstające najczęściej pod koniec okresu eksploatacji silników bądź w statkach powietrznych operujących w pobliżu zakładów chemicznych lub w środowisku morskim (rys. 9),
– uszkodzenia erozyjne statora sprężarki (rys. 10).

W związku z tym w trakcie remontów silników lotniczych i likwidacji powstałych uszkodzeń dokonuje się montażu filtrów powietrza, które ograniczają do minimum możliwość dostania się do sprężarki ciał obcych (rys. 11). To powoduje z kolei, że czas eksploatacji silników znaczne się wydłużenia.

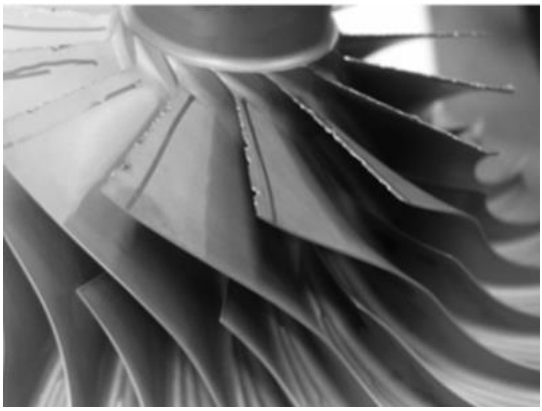

Rys. 3. Wirnik sprężarki uszkodzony ciałami obcymi (fot. P. Rutkowski)
Fig. 3. The compressor rotor damaged by foreign objects (photo P. Rutkowski)

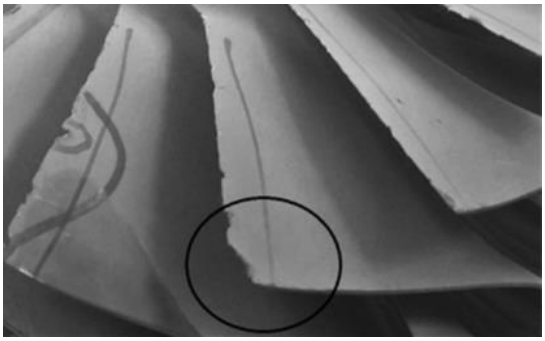

Rys. 4. Wyszczerbienia krawędzi natarcia łopatek wirnika sprężarki (fot. B. Przybyła)
Fig. 4. Nicks in the leading edge of the compressor impeller (photo B. Przybyła)

Rys. 5. Wgniecenia krawędzi natarcia wirnika sprężarki (fot. J. Haliniak)
Fig. 5. Dents in the leading edge of the compressor rotor (photo J. Haliniak)

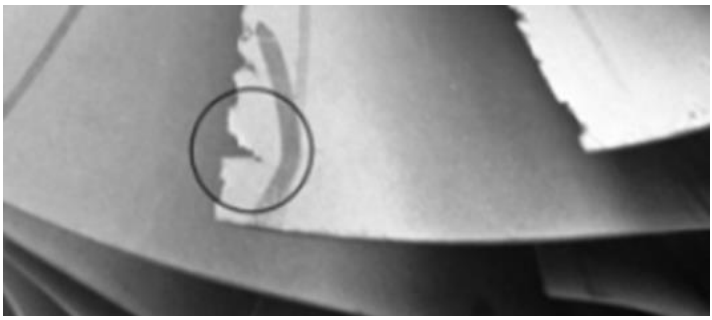

Rys. 6. Rozerwania łopatek wirnika sprężarki (fot. B. Przybyła)
Fig. 6. Tears of the blades of the compressor rotor (photo B. Przybyła)

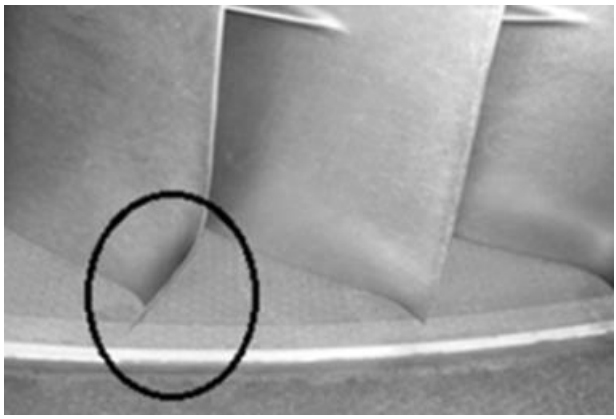

Rys. 7. Zniekształcenia łopatek wirnika sprężarki [4]
Fig. 7. Distortions of the blades of the compressor rotor [4]

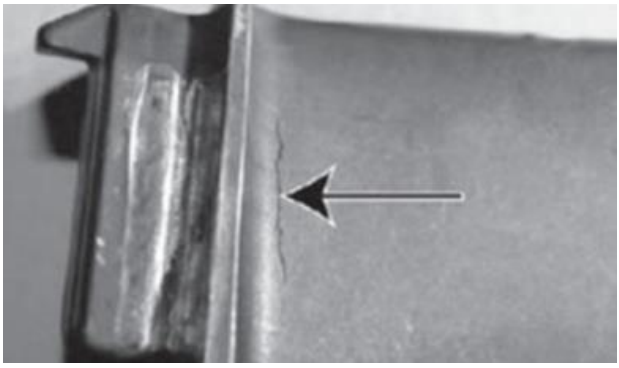

Rys. 8. Pęknięcie łopatki wirnika sprężarki [7]
Fig. 8. Cracks on the blade of the compressor rotor [7]

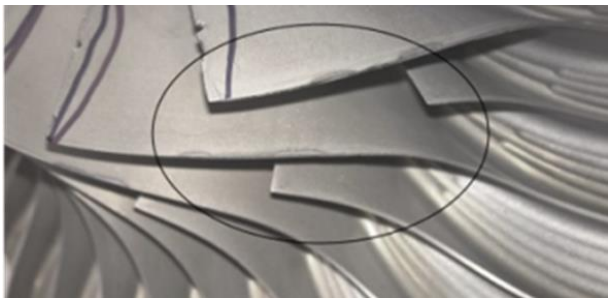

Rys. 9. Uszkodzenia erozyjne krawędzi łopatek wirnika sprężarki (fot. B. Przybyła)
Fig. 9. Erosion damage of the edges of the rotor blades of the compressor (photo B. Przybyła)

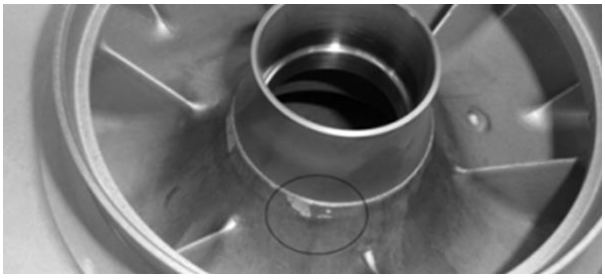

Rys. 10. Uszkodzenia erozyjne statora sprężarki (fot. P. Rutkowski)
Fig. 10. Erosion damage of the compressor stator (photo P. Rutkowski)

Rys. 11. Filtr powietrza zamontowany w śmigłowcu EC-135 (fot. B. Przybyła)
Fig. 11. Inlet barrier filter mounted on the EC-135 helicopter (photo B. Przybyła)

3. Ocena uszkodzeń oraz naprawa elementów sprężarki

W śmigłowcach EC-135, aby ocenić stan techniczny jednostki napędowej, wykonuje się sprawdzenie pośrednie mocy silnika na ziemi tzw. test „GPC" (Ground Power Check). W trakcie badania mierzy się następujące parametry silnika:

– prędkość obrotową wału wirnika sprężarki - n_1,
– prędkość obrotową wału turbiny napędowej - n_2,
– temperaturę gazów na wyjściu z turbiny napędzającej sprężarkę - t_{ot},
– natężenie przepływu paliwa - $\dot{m}_p$ (rys. 12).

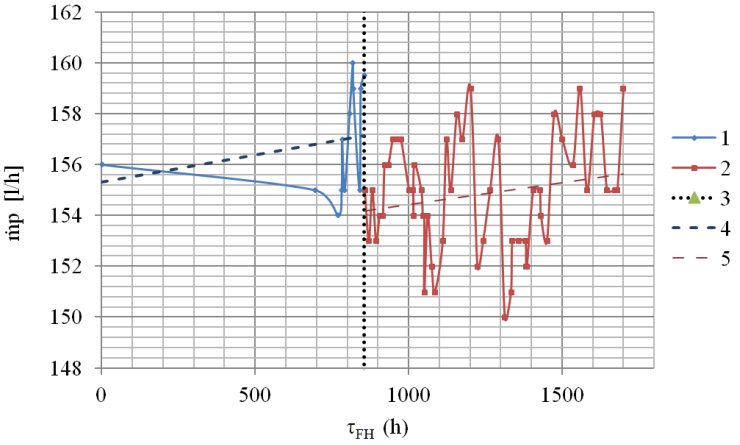

Rys. 12. Zależność natężenia przepływu paliwa $\dot{m}_p$ od czasu eksploatacji silnika τ_{FH}: 1 - przed naprawą silnika i montażem filtrów powietrza, 2 - po naprawie silnika i montażu filtrów powietrza, 3 - czas naprawy silnika i montażu filtrów powietrza, 4 - linia trendu przed naprawą silnika i montażem filtrów powietrza, 5 - linia trendu po naprawie silnika i montażu filtrów powietrza

Fig. 12. Dependence between fuel flow $\dot{m}_p$ and the time of exploration τ_{FH}: 1 - before the repair of the engine and the installation of air filters, 2 - after the repair of the engine and the installation of air filters, 3 –- the time of engine repair and the installation of air filters, 4 - trend line before repairing the engine and the installation of air filters, 5 - trend line after the repair of the engine and the installation of air filters

W trakcie eksploatacji silników wartości prędkości obrotowej wału wirnika sprężarki n_1 oraz temperatury gazów na wyjściu z turbiny napędzającej sprężarkę t_{ot} ulegają zmianie. Na podstawie otrzymanych wyników pomiarów, wyznacza się różnicę pomiędzy maksymalnymi dopuszczalnymi obrotami turbiny napędowej dla danego silnika a obrotami otrzymanymi z badań tj. parametr tzw. „Margin n_1 - Δn_1" (rys. 13). Drugim parametrem na podstawie, którego ocenia się stan jednostki napędowej jest różnicą pomiędzy maksymalną dopuszczalną temperaturą gazów na wyjściu z turbiny sprężarki a temperaturą otrzymaną z pomiarów tzw. „Margin TOT - Δt_{ot}" (rys. 14). Wartości parametrów dopuszczalnych (Δn_1 oraz Δt_{ot}) są podane w dokumentacji technicznej danego silnika turbinowego.

Uzyskane w ten sposób dane, pozwalają wstępnie określić stan techniczny głównych podzespołów silnika. Zauważono, że w badanym silniku, przed jego

remontem następuje wzrost obrotów sprężarki n_1, i temperatury gazów spalinowych za turbiną sprężarki t_{ot} oraz wzrost natężenia przepływu paliwa $\dot{m}_p$. Przyczynami takiej zmiany wielkości mierzonych, mogą być: ograniczony dopływ powietrza do silników poprzez np. zatkany wlot, nieszczelność w kanale wlotowym, zanieczyszczony, zerodowany bądź uszkodzony wirnik sprężarki. W miarę eksploatacji silnika, z powodu jednej z wyżej wymienionych przyczyn, do silnika dostaje się mniej powietrza a więc i obroty obu wałów są mniejsze. Komputer sterujący pracą silnika, analizuje jego parametry m.in. prędkość obrotową oraz moment obrotowy na wale napędowym, a następnie zwiększa ilość dostarczanego paliwa do silnika, tym samym zwiększając obroty sprężarki.

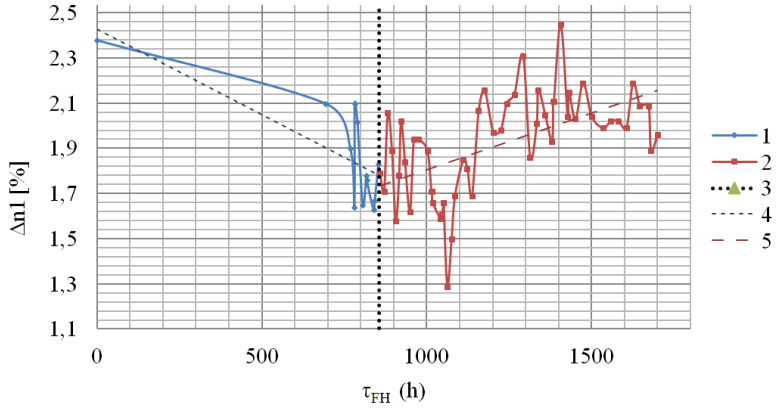

Rys. 13. Zależność parametru Δn_1 od czasu eksploatacji silnika τ_{FH}: 1 - przed naprawą silnika i montażem filtrów powietrza, 2 - po naprawie silnika i montażu filtrów powietrza, 3 - czas naprawy silnika i montażu filtrów powietrza, 4 - linia trendu przed naprawą silnika i montażem filtrów powietrza, 5 - linia trendu po naprawie silnika i montażu filtrów powietrza

Fig. 13. Dependence between the Δn_1 parameter and the time of exploration τ_{FH}: 1 - before the repair of the engine and the installation of air filters, 2 - after the repair of the engine and the installation of air filters, 3 – the time of engine repair and the installation of air filters, 4 – trend line before repairing the engine and the installation of air filters, 5 - trend line after the repair of the engine and the installation of air filters

Po remoncie silnika oraz montażu systemu filtrów powietrza, kiedy to wirnik sprężarki jest chroniony przed uszkodzeniami ciałami obcymi zauważono dalszy wzrost temperatury gazów za turbiną sprężarki t_{ot} oraz wzrost natężenia przepływu paliwa $\dot{m}_p$, natomiast spadek obrotów sprężarki n_1. Przyczyną takich zmian parametrów, może być uszkodzenie statora bądź wirnika turbiny napędzającej sprężarkę, pogorszenie się stanu technicznego części gorącej silnika tj. komory spalania lub wtryskiwaczy paliwa, oraz zużycie lub uszkodzenie okładzin uszczelniających wał turbiny. Turbina ma wtedy mniejszą sprawność, a więc wytwarza mniejszy moment obrotowy niż ten niezbędny. Żeby ten spadek mocy

zrekompensować, do silnika dostarczana jest większa ilość paliwa, a to z kolei powoduje wzrost temperatury gazów spalinowych za turbiną napędową sprężarki.

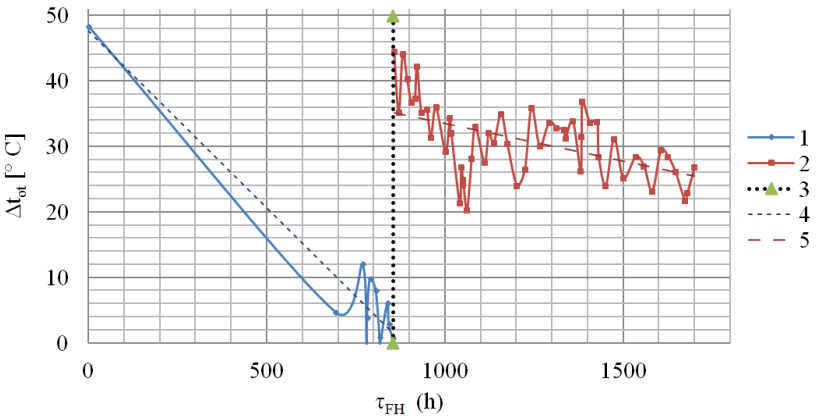

Rys. 14. Zależność parametru Δt_{ot} od czasu eksploatacji silnika τ_{FH}: 1 - przed naprawą silnika i montażem filtrów powietrza, 2 - po naprawie silnika i montażu filtrów powietrza, 3 - czas naprawy silnika i montażu filtrów powietrza, 4 - linia trendu przed naprawą silnika i montażem filtrów powietrza,5 - linia trendu po naprawie silnika i montażu filtrów powietrza

Fig. 14. Dependence between the Δt_{ot} parameter and the time of exploration τ_{FH}: 1- before the repair of the engine and the installation of air filters, 2 - after the repair of the engine and the installation of air filters, 3 - the time of engine repair and the installation of air filters, 4 - trend line before repairing the engine and the installation of air filters, 5 - trend line after the repair of the engine and the installation of air filters

Do oceny stanu technicznego silnika wykorzystuje się też nieinwazyjną technikę diagnostyczną zwaną boroskopią. Boroskopia polega na wprowadzeniu światłowodu do wnętrza silnika, poprzez odpowiednie kanały oraz inspekcji badanego podzespołu (rys. 15), a w przypadku stwierdzenia jego uszkodzenia do pomiaru wielkości uszkodzenia (rys. 16).

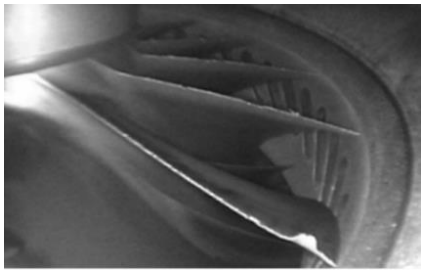

Rys. 15. Widok wnętrza sprężarki podczas boroskopii (fot. J. Haliniak)

Fig. 15. View of the compressor during boroscopy (photo J. Haliniak)

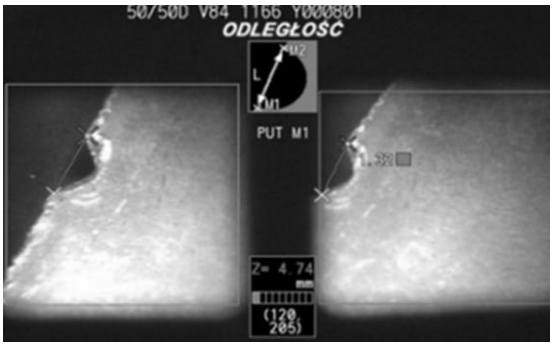

Rys. 16. Pomiar wielkości uszkodzenia wirnika sprężarki (fot. J. Haliniak)

Fig. 16. Measurement of damage to the compressor rotor (photo J. Haliniak)

4. Naprawa uszkodzeń sprężarki

Wykryte podczas boroskopii uszkodzenia wirnika sprężarki, nie zawsze dyskwalifikują silnik z dalszej jego eksploatacji. Wyłączenie silnika z eksploatacji jest uzależnione od stwierdzonego stopnia uszkodzenia tego elementu. Producent będąc świadomym degradacji łopatek sprężarki podczas jej użytkowania zamieścił w instrukcji obsługi silnika, dopuszczalne wartości graniczne parametrów geometrycznych oraz podał zakres koniecznych napraw. Proponowane przez producenta naprawy krawędzi łopatek wirnika sprężarki można dokonywać przy zabudowanej jednostce napędowej, bez jej demontażu. Do tego celu stosuje się specjalne szlifierki elektryczne z giętkim wałkiem oraz zestawem kamieni szlifierskich lub zestawy do szlifowania manualnego. Proces ten ma na celu zlikwidowanie bądź zminimalizowanie naprężeń w łopatce oraz poprawę przepływu powietrza. Uszkodzenia szlifuje się, nadając im odpowiedni promień oraz wygładza się ostre krawędzie (rys. 17). Po wykonaniu naprawy (rys. 18) parametry silnika są przywrócone. Naprawa elementów sprężarki pozwala uniknąć jej całkowitego zniszczenia.

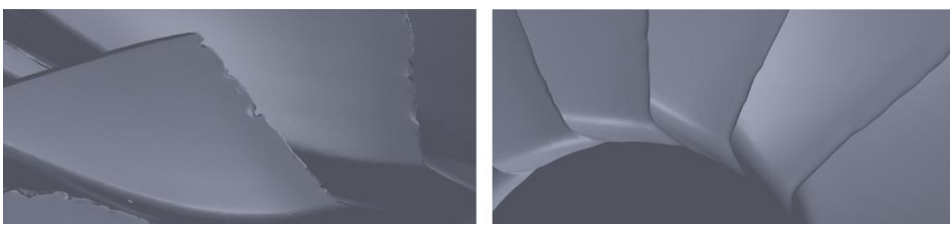

Rys.17. Widok uszkodzonych krawędzi natarcia łopatek sprężarki przed i po naprawie

Fig. 17. View of the damaged leading edge of the rotor blades of the compressor before and after the repair

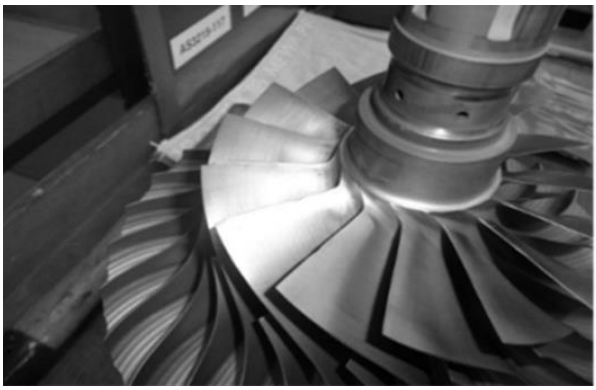

Rys. 18. Wirnik sprężarki po remoncie (fot. P. Rutkowski).
Fig. 18. Compressor rotor after the repair (photo P. Rutkowski)

5. Podsumowanie

Określenie stanu technicznego wirnika sprężarki ma istotny wpływ na dalszą eksploatację silnika lotniczego P&W 206 b2. Uszkodzenia łopatek wirnika sprężarki nie zawsze wykluczają ten silnik z dalszego użytkowania. Jednak wykonanie zalecanych prac naprawczych znacząco wydłuża jego okres użytkowania i bezpośrednio wpływa na obniżenie kosztów eksploatacji. Umiejętność oceny stanu technicznego silnika na podstawie wyników testu naziemnego pozwala na szybsze zdiagnozowanie ewentualnych uszkodzeń oraz podjęcie dalszych szczegółowych działań sprawdzających poszczególnych elementów sprężarki. Naprawa układu łopatkowego sprężarki pozwala przywrócić początkowego parametry pracy silnika, co wpływa istotnie na obniżenie kosztów użytkowania śmigłowca.

Acknowledgement

The research leading to these results has received funding from the People Programme (Marie Curie International Research Staff Exchange) of the European Union's Seventh Framework Programme FP7/2007-2013/ under REA grant agreement n° PIRSES-GA-2013-610547.

Literatura

[1] Balicki W.: Lotnicze silniki turbinowe, Wydawnictwa Naukowe Instytutu Lotnictwa, Warszawa 2010.
[2] Dzierżanowski P.: Napędy lotnicze. Turbinowe silniki odrzutowe. Wydawnictwa Komunikacji i Łączności, Warszawa, 1983.
[3] Tuliszka E.: Turbiny cieplne: zagadnienia termodynamiczne i przepływowe, WNT, Warszawa 1973.
[4] www.flightsafetyaustralia.com, data dostępu 10.02.2016.
[5] www.gasturb.de, data dostępu 10.02.2016.

[6] www.mtu.de, data dostępu 12.02.2016.
[7] www.tc.gc.ca, data dostępu 23.01.2016.

DAMAGE OF A CENTRIFUGAL COMPRESSOR OF P&W 206 b2 AIRCRAFT ENGINE CAUSED BY FOREIGN OBJECTS

S u m m a r y

This paper presents the most common damage of the compressor of P&W 206b2 centrifugal engines mounted in helicopters EC-135, operated by Polish Medical Air Rescue. This damage is the result of the work of these engines in a seaside lane, landings on the beach and sucking foreign objects, such as: sand, dust, water droplets etc. Impurities in the intake air cause the changes of operating parameters of an engine. In turn, on this basis, the technical conditions of an engine can be evaluated. This paper discusses the method of assessing the damage to compressor components and provides a way to repair them.

Keywords: aircraft engine, centrifugal compressor, compressor damage

DOI: 10.7862/rm.2016.12

Otrzymano/received: 19.03.2016 r.
Zaakceptowano/accepted: 21.05.2016 r.

ZESZYTY NAUKOWE POLITECHNIKI RZESZOWSKIEJ 293, Mechanika 88
RUTMech, t. XXXIII, z. 88 (2/16), kwiecień-czerwiec 2016, s. 153-165

Roman SHMEGERA[1]
Volodymyr KUSHCH[2]

INTENSIVE ELECTRO SINTERING OF DIAMOND COMPOSITES WITH MULTICOMPONENT Ni-Sn BASED BINDER

This paper deals with intensive electro sintering (IES) of diamond composite materials (DCM) with multicomponent Ni-Sn based binder. The effect of the powder mixture composition, activating dopants and IES technical parameters on the formation of the microstructure and physical, and mechanical properties of DCM is studied. It has been established that the leading densification mechanisms of IES involve thermally activated plastic deformation of nickel powder particles, tin melting, and infiltration and chemical interaction of components. The presence of a liquid phase during the electro sintering increases conductivity of powder compact and intensity of heating which, in turn, significantly increases shrinkage rate and promotes uniform distribution of components and formation of intermetallic compounds. The macro-kinetic model of intermetallic compounds formation in the Ni-Sn system in non-isothermal conditions and the model of DCM with structured matrix and imperfect interface have been developed. The thermal and mechanical properties of electro sintered DCM have been evaluated. The initial mixture composition and the IES technological parameters promising in terms of DCM quality have been found. The proposed method of manufacturing the drilling bits by IES constitutes a potential basis for the industrial production technology of diamond tools.

Keywords: diamond composites, shrinkage, sintering, thermal conductivity

1. Introduction

The conventional powder metallurgy methods of diamond composite materials (DCM) production for tool applications are vacuum sintering, hot pressing and infiltration. The inherent feature of these and related technologies is quite a long exposure at high (>1000°C) temperature. So high thermal loading provokes diamond cracking and/or graphitization already at the stage of DCM production,

[1] Autor do korespondencji/corresponding author: Roman Shmegera, Institute for Superhard Materials of the National Academy of Sciences, Kyiv, Ukraine, e-mail: shmegerar@ukr.net
[2] Volodymyr Kushch, V.Bakul Institute for Superhard Materials of the National Academy of Sciences, Kyiv, Ukraine, e-mail: vkushch@bigmir.net

which results in reducing their physical, mechanical and performance properties. Improvement of DCM quality can be achieved by significant lowering the temperature and reducing the sintering time as well as by formation of the reliable chemical or adhesive bond between the diamonds and matrix.

The above requirements are met by the intensive electro sintering (IES) technology [1] which consists in passing the electric current through the highly loaded (up to 500 MPa) powder compact. IES is regarded as a promising alternate DCM production technology because its *pT*-parameters allow to avoid degradation of diamond and thus improve the quality of the diamond tools. In addition, the small localized heating zone and transience of the process reduce energy consumption by an order in comparison with the conventional technologies. Currently, practical use of IES is limited to DCM with one-component binders, whose tensile strength and fracture toughness is insufficient for drilling tool applications. A highly promising - but still practically unexplored - area is intensive electro sintering of DCM with multicomponent binder including the activating and alloying additives. However, practical implementation of the advantages of this technology requires development of new, optimized for IES technology DCM binders, study of consolidation patterns and structure formation and their effect on the DCM physical, mechanical and performance properties.

2. Experimental study

It has been shown recently [2] that the Ni-Sn based alloys have a great potential as the IES-oriented DCM binder. The main component of this binder (> 50%) is nickel which, in contrast to iron and cobalt, retains considerable plasticity in the doping and is resistant to oxidation that enables sintering without a protective atmosphere. In addition, nickel at 700°C and above interacts actively with diamond by creating a reliable adhesive contact. The main activating element is tin (up to 15%), which provides electro sintering in the presence of liquid phase and gives, as a result of chemical reaction with the other components, intermetallic compounds that increase hardness and wear resistance of binder. Its durability can be further increased by filling in a certain amount (15-20%) of powder of refractory compounds (WC, TiC, TiB_2, etc.). Adding chromium known to be an effective carbide former is intended to improve diamond-to-matrix bonding. For manufacturing the samples, the nickel and tin powders and synthetic diamonds ACT200 400/315 were mixed in a rattler with hard metal balls in dry grinding mode for 8 hours. The powder mixture was compacted by two-sided cold pressing by pressure of 300 MPa resulting in porosity of compacts around 40%. The intensive electro sintering of samples was carried out by passing the current density of 25 A/mm2 with applying pressure of 150 MPa.

The time-dependent parameters of IES, for example current density (fig. 1) and shrinkage (fig. 2) of DCM binder demonstrate that sintering in the presence of a limited amount of liquid phase (curve 2) differs significantly from solid

state sintering (curve 1). The presence of tin in the mixture provides the appearance of a liquid phase already in the early stage of sintering, resulting in a significant increase in the conductivity of the sample. In turn, this leads to more intensive heating and significant intensification of shrinkage and chemical reactions with formation of the intermetallic compounds. Noteworthy, shrinkage of porous compact begins with some delay (3 s for nickel, and 6 seconds for mixture, fig. 2). This is because the axial pressure of cold pressing (300 MPa) is higher than the pressure during sintering Therefore, plastic flow being the main densification mechanism is activated only when the macroscopic yield strength of porous solid was reduced sufficiently under the action of temperature. Among the possible causes of greater time delay in a case of a powder mixture is that tin facilitates consolidation during the cold pressing resulting in the lower porosity and hence higher yield strength of compact. It is also likely that the transition of one of the components in the liquid phase absorbs a certain amount of heat, thus slowing down the heating process and delaying the start of shrinkage.

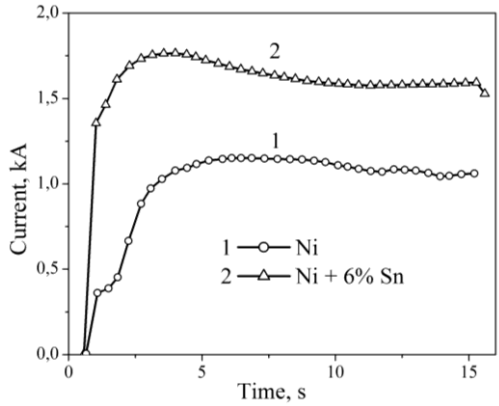

Fig. 1. Current density as a function of time

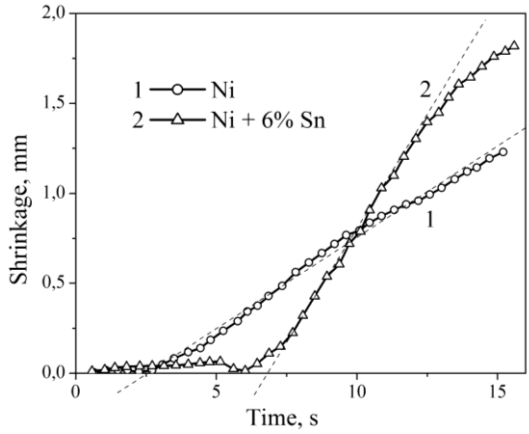

Fig. 2. Shrinkage as a function of time

This, the experimental study proves IES as a highly efficient method of manufacturing the DCM with Ni-Sn binder providing full consolidation of powder compacts for tens of seconds at the sintering temperature below 850°C thus maintaining the original quality of diamonds. The leading densification mechanisms of IES are thermally activated plastic deformation of the nickel powder, tin melting/infiltration and chemical reactions between the components. Presence of a limited amount of liquid phase during the electro sintering significantly increases electrical conductivity of compact and thus intensity of heating and shrinkage rate and also facilitates uniform distribution of components and formation of intermetallic compounds.

3. Macro-kinetic model

The fundamentally important parameter is the time of sintering. For reasons of preserving high quality of diamonds it should be the lowest possible but, at the same time, sufficient for the heterogeneous microstructure formation as a result of chemical reactions. According to the Ni-Sn binary phase diagram (e.g., [3, 4]), formation of Ni_3Sn_4, Ni_3Sn_2 and Ni_3Sn intermetallics during sintering is expected. The experimental data (e.g., [5, 6]) and theoretical models [7, 8] of the Ni-Sn intermetallics formation are available only for the case of isothermal conditions and solid samples. The only paper [9] is available where mixture of nickel and tin powders was studied. It has been found there that heating the mixture to 300°C followed by exposure leads to the formation of all three intermetallic compounds, but no quantitative data were reported.

To describe/predict the process of intermetallics formation in the rapidly heated Ni-Sn powder mixture, the macro-kinetic model has been formulated under the assumption that the rate of each reaction depends on the temperature and concentration by Arrhenius law and the law of mass action, respectively. To account for the diffusive nature of all stages and "braking" the reaction rate by increasing product layer the appropriate braking parameters were introduced. In particular, for Ni + 12% Sn the model predicts completing the reactions in 30 seconds at 900°C while at 800°C it takes above 5 minutes. The model has been experimentally verified and then applied to determine the optimum temperature and the time of sintering.

Among many possible chemical reactions in the Ni-Sn system [3, 4], we consider three most obvious and experimentally confirmed ones:

$$3Ni + 4Sn \rightarrow Ni_3Sn_4;\quad Ni_3Sn_4 + 3Ni \rightarrow 2Ni_3Sn_2;$$
$$Ni_3Sn_2 + 3Ni \rightarrow 2Ni_3Sn. \tag{1}$$

We introduce notations for mass concentrations of reactants and products:

$$y_1 = [Ni];\ y_2 = [Sn];\ y_3 = [Ni_3Sn_4];\ y_4 = [Ni_3Sn_2];\ y_5 = [Ni_3Sn] \qquad (2)$$

where n is a number of substances involved in the reactions (in our case, 5). Each reaction is carried out based on the law of conservation of mass:

$$\sum_{k=1}^{n} \nu_{ki} m_k = 0\ (i = 1,..., r), \qquad \sum_{k=1}^{n} y_k = 1 \qquad (3)$$

where ν_{ki} is the stoichiometric coefficient of component k in the reaction i (in our case, $r = 3$); m_k is its molar weight [kg/mol]: m_1=58.69·10^{-3}; m_2 =118.71·10^{-3}; $m_3 = 3m_1 + 4m_2$; $m_4 = 3m_1 + 2m_2$ and $m_5 = 3m_1 + m_2$.

The formal kinetic equations are based on the standard balance equations where diffusion is taken into account as the slowest process that occurs at the level of individual particles and affects the formal kinetic laws. The balance equations take the form:

$$\rho \frac{dy_k}{dt} = \omega_k \qquad (4)$$

where ω_k is a sum of sources and sinks of component k in reactions:

$$\omega_k = \sum_{i=1}^{r} m_k \nu_{ki} \Phi_i \qquad (5)$$

Here Φ_i is the reaction rate [mol/(m^{3}s)] dependent on the concentrations by the law of mass action:

$$\Phi_1 = z_1 y_1^{\,3} y_2^{4};\ \Phi_2 = z_2 y_3 y_1^{3};\ \Phi_3 = z_3 y_4 y_1^{3}, \qquad (6)$$

where (see, e.g., [10]):

$$z_i = z_{i0} \exp\left(-\frac{E_{ai}}{RT}\right) \exp(-p_i y) y^{-s_i} \qquad (7)$$

$y = y_2 + y_3 + y_4$ is a fixed component which hinders diffusion of reactants to each other and withdrawal of products from the reaction zone, z_{i0} is the rate

constant of reaction, R is the universal gas constant, T is the temperature and E_{ai} is the activation energy of reaction. The braking parameters p_i, s_i are usually determined from an experiment or found from the micro models which take into account the diffusion through the product layer and interface reactions between the particles of various size, etc. [11]. All the microscopic processes affect the values of constants z_i which are measured in mol/(m^{3}s). The explicit form of the system (4) is:

$$\begin{aligned} &\rho\frac{dy_1}{dt} = -3m_1\left[\Phi_1+\Phi_2+\Phi_3\right];\ \rho\frac{dy_2}{dt} = -4m_2\Phi_1;\\ &\rho\frac{dy_3}{dt} = m_3\left[\Phi_1-\Phi_2\right];\ \rho\frac{dy_4}{dt} = m_4\left[2\Phi_2-\Phi_3\right];\ \rho\frac{dy_5}{dt} = 2m_5\Phi_3. \end{aligned} \tag{8}$$

As an example, we conduct calculations for the powder mixture Ni+12% Sn heated by some known law $T(t)$. At the beginning, composition of the powder mixture is given by the conditions:

$$y_1 = y_{10};\quad y_2 = y_{12};\quad y_3 = y_4 = y_5 = 0. \tag{9}$$

To find the mass content of components variation over the time one needs to integrate the ordinary differential equations (8) with the initial conditions (9). The input material parameters reported below were taken from [3, 5, 7, 12]; p_i = 10, s_i = 0 [10].

Table 1. Thermal properties of the Ni-Sn intermetallics

Phase	T_{melt}, K	ρ, g/sm^3	C_p, $\frac{\text{J}}{\text{mol}\cdot\text{K}}$	M, $\frac{\text{g}}{\text{mol}}$	S^0_{298}, $\frac{\text{J}}{\text{mol}\cdot\text{K}}$	$-\Delta H_{298}$, $\frac{\text{kJ}}{\text{mol}}$
Ni_3Sn_4	1057	8.42	160.3	650.9	257.7	177.3
Ni_3Sn_2	1538	9.02	108.7	413.5	173.6	156.9
Ni_3Sn	1250	9.49	99.6	294.8	131.4	93.7

Table 2. Formal kinetic parameters of the reactions

Reaction	$S_{reaction}$, J/(mol·K)	E_a, J/mol	z_{i0}, 1/s
$3Ni + 4Sn \rightarrow Ni_3Sn_4$	-38.10	49060	$7.217\cdot10^{11}$
$Ni_3Sn_4 + 3Ni \rightarrow 2Ni_3Sn_2$	-0.119	242670	$5.87\cdot10^{9}$
$Ni_3Sn_2 + 3Ni \rightarrow 2Ni_3Sn$	-0.419	243300	$5.686\cdot10^{9}$

The system of equations (9) was solved by the Runge-Kutta method with variable in time temperature:

$$T(t) = \begin{cases} (T't - T_0)/(T_{\max} - T_0) & t \le t_{\max} \\ T = T_{\max}, & t > t_{\max} \end{cases} \tag{10}$$

where T_0 is the initial temperature and $t_{\max}$ is the heating time to maximum temperature $T_{\max}$. Figure 3 shows the simulation results for the chemical reactions in Ni-Sn system heated from 20 to 800°C (fig. 3(a)) and 900°C (fig. 3(b)) during 10 seconds with subsequent exposure. The model predicts a rapid decrease (almost zero) tin content at the stage of heating ($t_{\max}$ < 10 seconds) to form intermetallic Ni_3Sn_4. However, at $t = t_{\max}$ we already have some amount of Ni_3Sn_2, then these two intermetallics react with nickel to form Ni_3Sn. For $T_{\max}$ = 800°C estimated duration of chemical reaction is 5 minutes whereas for $T_{\max}$ = 900°C the model predicts completion of chemical reactions after 30 seconds of exposure.

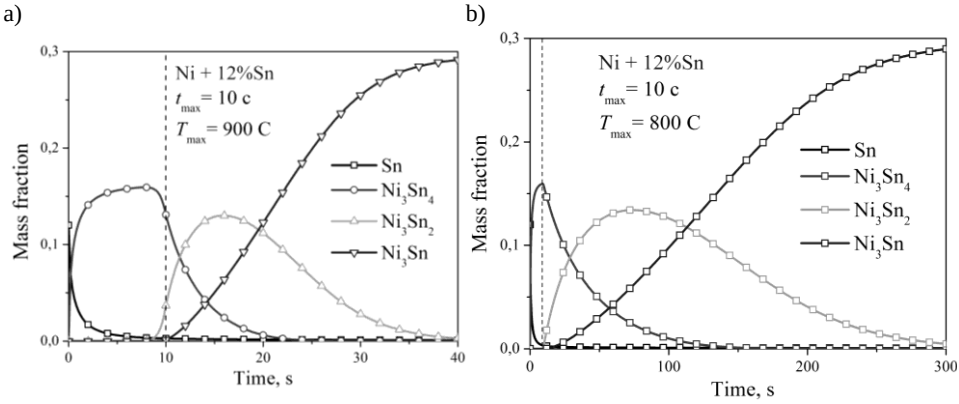

Fig. 3. Chemical reactions in Ni-Sn system when heated from T_0 = 20°C to (a) $T_{\max}$ = 800°C and (b) $T_{\max}$ = 900°C for $t_{\max}$ = 10 seconds with subsequent exposure

For the experimental verification of the developed model, the microstructure and phase composition of two-component DCM binder Ni+12% Sn produced by intensive electro sintering with a temperature profile close to (10) with $T_{\max}$ = 900°C has been analyzed. Figure 4(a) shows microstructure of the partially sintered binder: dark color is nickel, bright color is tin, gray color is intermetallic layer Ni_3Sn_4, black color shows the pores. According to X-ray analysis, binder also contains about 4 wt% of Ni_3Sn. Sintering was intentionally interrupted after 12 seconds to capture evolution of the structure, including the thickness of the reaction layer (noteworthy, it is almost constant). The structure of the same binder sintered for 30 seconds is homogeneous and almost pore-free (fig. 4(b)). The X-ray microanalysis confirms that the reinforcing phase consists al-

most entirely of intermetallic Ni_3Sn which means completion of chemical reactions. These experimental data are quantitatively and qualitatively consistent with simulations that confirms the adequacy of the proposed model.

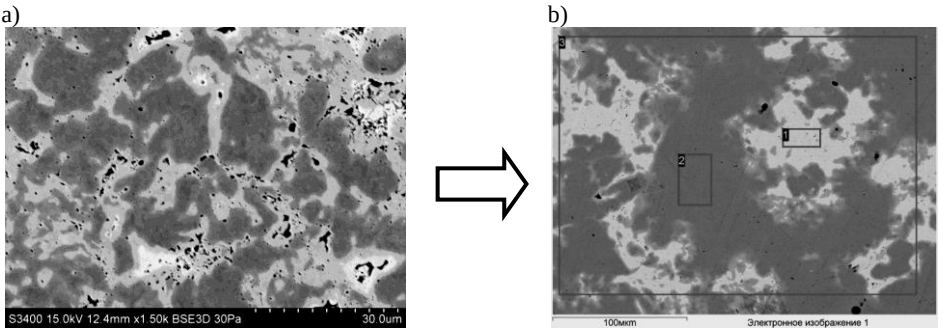

Fig. 4. Microstructure of the partially (after 12 seconds) and completely (after 30 seconds) sintered two-component binder Ni + 12% Sn

4. DCM characterization

4.1. *Thermal conductivity*. For the tool-oriented DCM, reliable adhesive/chemical diamond-to-matrix bonding is particularly important because it determines the retention strength of diamonds and, hence, overall tool performance. Weak bonding worsens temperature regime of diamond grains and leads to their untimely dropping out of the working surface of a tool. There exists a strong correlation between the quality of thermal and mechanical contact because both are determined by the same physical and chemical processes at the interface. This fact is crucial for using the thermal conductivity as a DCM quality criterion.

It has been found that thermal conductivity of Ni-Sn binder significantly decreases with increasing volume fraction of intermetallic phase (fig. 5). DCM conductivity increases with increasing volume fraction of diamonds (fig. 6). Adding the adhesion-active components to the binder provides a significant improvement in the thermal and mechanical properties of DCM. Deposition of chromium on the surface of diamond increases effective thermal conductivity of diamond composite with Ni + 6%Sn binder by 15 - 25%, that is a probable consequence of interface chemical reactions. The obtained data were interpreted with aid of the micromechanical model of composite with imperfect interface [14] predicting the effective thermal conductivity of composite as well as evaluating the interface contact conductivity by solving the inverse problem. It has been found that adding Cr increases the contact thermal conductivity of diamond-binder interface tenfold, from $2.1 \cdot 10^6$ to $2.3 \cdot 10^7$ W/(m^2·K) [14] being typical value for chemical bonding case [15].

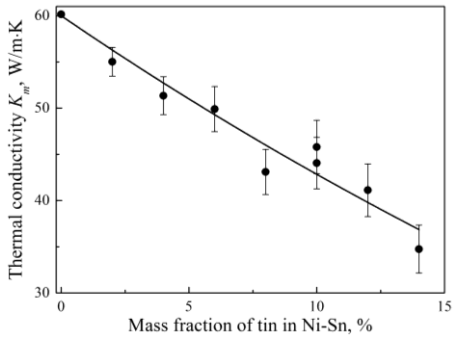

Fig. 5. Thermal conductivity of Ni-Sn binder: solid circles represent experimental data, solid curve is approximation

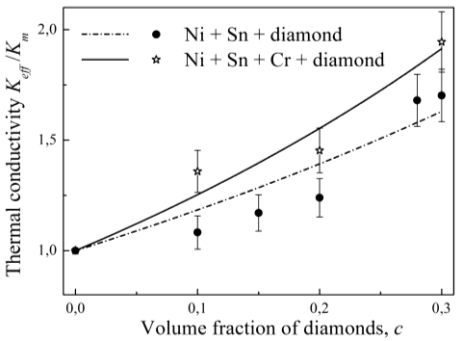

Fig. 6. - Thermal conductivity of DCM with Ni+6%Sn binder (solid circles) and with adding Cr (open stars)

4.2. *Deformation curve and hardness*. The presence of tin significantly (up to 2.5 times for the 16% Sn mass fraction) increases yield limit of binder. This is due to formation of the heterogeneous microstructure where the intermetallics play a role of hard reinforcing phase. In contrast to the binders obtained by conventional powder metallurgy methods or solid-phase IES, the studied samples do not exhaust the resource of plasticity even under strain in tens of percents. The curves in figures 5-7 show a significant hardening of the material, and therefore no significant residual stresses after IES the presence of a limited amount of liquid phase. Macro hardness and yield strength of Ni-Sn alloy increase with increasing fraction of intermetallics, see figure 8.

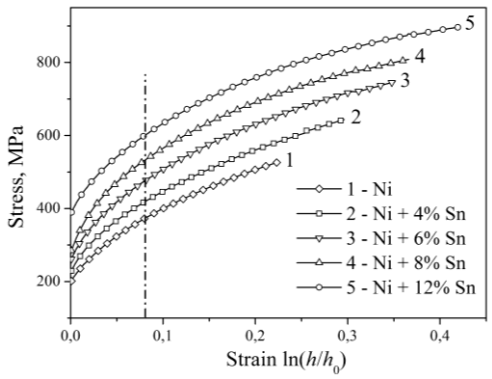

Fig. 7. Deformation curves of the electro sintered Ni and Ni-Sn alloys

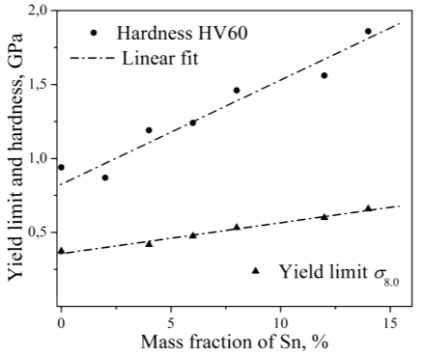

Fig. 8. Macro hardness and yield limit of Ni-Sn alloys

4.3. *Micro- and nanohardness*. Micro and nanohardness of electro sintered DCM binder was conducted by the multiple indentation technique [16], which consists in conducting a series of tests (fig. 9) followed by statistical processing of the obtained indentation curves (fig. 10).

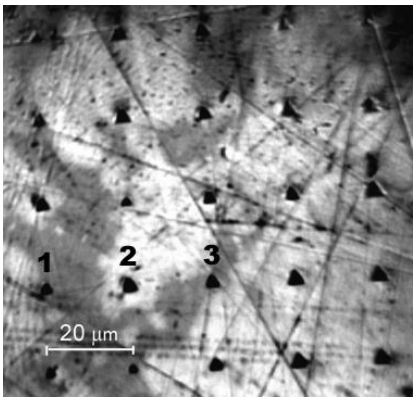

Fig. 9. Grid of indents in DCM binder Ni-6%Sn

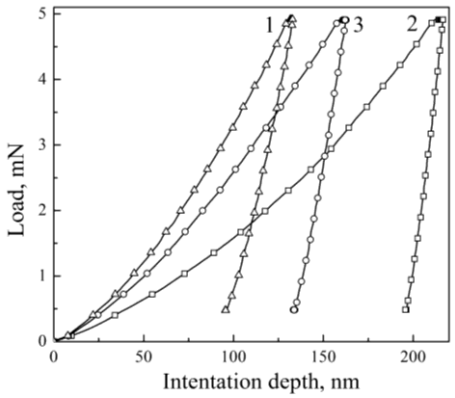

Fig. 10. Load - displacement curves for Ni (curve 1), Ni_3Sn (curve 2) and their mixture (curve 3)

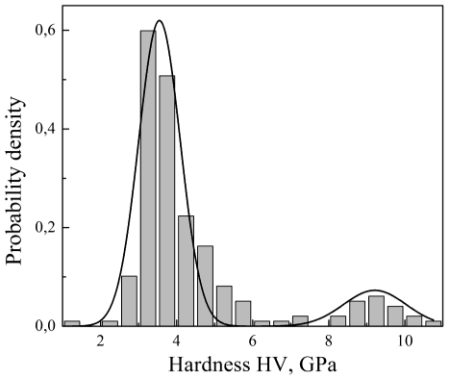

Fig. 11 - Hardness distribution of DCM binder Ni-6%Sn

Comparing the simulation results with experimental data on macro hardness (HV60), micro hardness (HV20g and HV200g) and nanohardness under load 5 mN (figs. 9-11) proves the substantial load-dependence of hardness. In particular, for Ni_3Sn this technique predicts micro hardness HV200g = 2.4 GPa, HV20g in the range of 3.7 to 3.9 GPa and nanohardness from 8.4 to 9.2 GPa for 5 mN load.

4.4. *Fracture*. In completion, we show some results of SEM study of DCM microstructure. In figure 12, the fracture surface of electro sintered DCM (400/315 AST160 diamonds, binder Ni+10%Sn) is shown.

The fact that macro crack passed through the diamond crystals indicates that the strength of the diamond-to-matrix bond exceeds the tensile strength of diamond in the plane (111). On the other diamonds, the rests of binder are observed, especially on the faces (100). This is consistent with the available litera-

ture data [17] on the contact interaction of nickel with diamond at 700°C and above with formation of the adhesive bond with strength of 300 MPa. The fracture behavior of binder is viscous in nickel and brittle in the intermetallic inclusions, see figure 13.

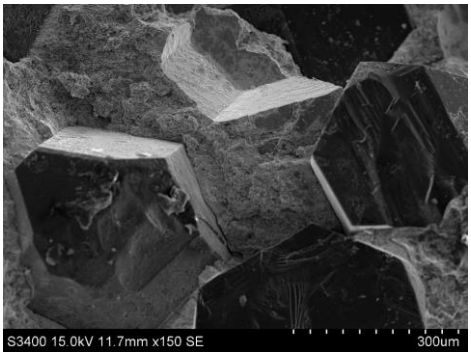

Fig. 12. Fracture surface of electrosintered DCM

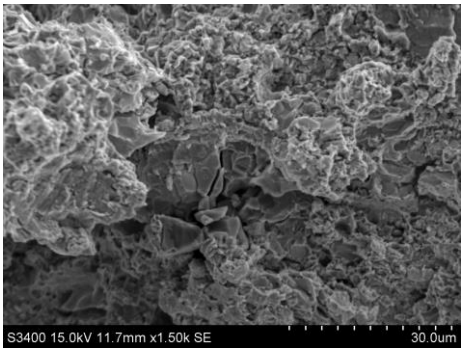

Fig. 13. Fracture surface of DCM binder

5. Concluding remarks

The advantages of using IES for DCM production are as follows. First, in contrast to conventional powder metallurgy technologies, consolidation of powder compacts takes units or tens of seconds at the sintering temperature of 850°C which excludes degradation of diamonds. Second, IES does not require renewable or protective atmosphere that simplifies greatly the manufacturing process. Third, the limited heating area and transience of process reduces energy consumption by an order as compared to traditional technologies. The presence of a limited amount of the liquid phase during the sintering results in significant improvement in physical and mechanical properties due to formation of specific heterogeneous microstructure with the intermetallic compounds acting as a hard reinforcing phase and significantly (by 2.5 times) increasing the hardness and yield limit of binder. What is important, the macro plasticity of DCM is retained: compressive deformation of 40% does not result in cracking or fracture patterns. The established correlations between the initial mixture composition and physico-mechanical properties of the material ensure producing by IES the pore-free structure of DCM and purposeful formation of its properties for the specific tool application. The above mentioned results constitute a scientific basis of the fast and energy-efficient industrial technology of the diamond tools manufacturing.

Acknowledgement

The research leading to these results has received funding from the People Programme (Marie Curie International Research Staff Exchange) of the European Union's Seventh Framework Programme FP7/2007-2013/ under REA grant agreement n° PIRSES-GA-2013-610547.

References

[1] Maystrenko A.L., Ivanov S.A., Pereyaslov V.P., Voloshym M.N.: Intensive electro sintering of diamond-containing composite materials, J. Superhard Materials, 22 (2000), 36-42.

[2] Shmegera R.S., Kushch V.I., Maystrenko A.L.: Metal binder based on nickel for an intensive electro sintering of diamond-containing composites. J. Superhard Materials, 36 (2014) 393-400.

[3] Van Beek J.A. , Stolbe S.A., van Loo F.J.J.: Multiphase diffusion in the systems Fe-Sn and Ni-Sn, Z. Metallkde, 73 (1982) 439-444.

[4] Schmetterer C., Flandorfer H., Richter K.W., et al.: A new investigation of the system Ni-Sn, Intermetallics, 15 (2007) 869-884.

[5] Eremenko V.N., Woodman N.D., Kostrova L.I., Verhovodov P.A.: Contact reaction at tin spreading in nickel. Powder metallurgy, 3 (1985) 31-34.

[6] Bader S., Gust W., Hieber H.: Rapid formation of intermetallic compaunds by interdiffusion in the Cu-Sn and Ni-Sn systems, Acta Metall. Mater., 43 (1995) 329-337.

[7] Klepser C.A.: Growth of Intermetallic Phases at Low Temperature, PhD Thesis, MIT, 1996.

[8] Dybkov V.I.: Reaction Diffusion and Solid State Chemical Kinetics, IPMS Publications, Kyiv 2013p.

[9] Gur D., Bamberger M.: Reactive isothermal solidification in the Ni-Sn system, Acta Materialia, 46 (1998) 4917-4923.

[10] Sorokova S.N., Knyazeva A.G.: Linked model of sintering Ti-TiAl3 powder systems, Bull. Tomsk Polytechnic Univ., 314 (2009) 96-101.

[11] Evstigneev N.K., Knyazeva A.G.: Choice of rheological models to describe the synthesis of the intermetallic compound, combined with extrusion through conical mold, PSTU Bulletin - Mechanics, 1 (2010) 59-71.

[12] Binnewies M., Milke E.: Thermochemical Data of Elements and Compounds, Wiley, Weinheim 2002.

[13] Hasselman, D.P.H. and Johnson, L.F.: Effective thermal conductivity of composites with interfacial thermal barrier resistance, J. Compos. Mater., 21 (1987) 508-515.

[14] Shmegera R.S., Podoba Ya.O., Kushch V.I., Belyaev A.S.: Effect of the contact conductivity of the diamond-metal binder interface on the thermal conductivity of diamond-containing composites, J. Superhard Materials, 37 (2015) 242-252.

[15] Stoner R.J., Maris H.J., Anthony T.R., Banholzer W.F.: Measurements of the Kapitza conductance between diamond and several metals, Phys. Rev. Let., 68 (1992) 1563-1566.

[16] Kushch V.I., Dub S.N., Shmegera R.S., Sirota Yu.V., Tolmacheva G.N.: Procedure of the multiple indentations for determination of the hardness parameters of heterogeneous materials J. Superhard Materials, 37 (2015) 173-181.

[17] Bokhonov B.B.,Ukhina A.V., Dudina D.V., Gerasimov K.B., Anisimov A.G., Mali V.I.: Towards a better understanding of nickel/diamond interactions: the interface formation at low temperatures, RSC Advances, 5 (2015) 51799-51806.

INTENSYWNE SPIEKANIE OPOROWE KOMPOZYTÓW DIAMENTOWYCH ZE SPOIWEM WIELOSKŁADNIKOWYM NA BAZIE Ni-Sn

S t r e s z c z e n i e

Tematyka artykułu dotyczy intensywnego spiekania oporowego (ISO) diamentowych materiałów kompozytowych (DMK) ze spoiwem wieloskładnikowym na bazie Ni-Sn. Badano wpływ składu mieszanki proszku, domieszek aktywujących i parametrów technologicznych spiekania na tworzenie mikrostruktury oraz na właściwości fizyczne i mechaniczne DMK. Ustalono, że mechanizmy zachodzące podczas spiekania oporowego obejmują termicznie aktywowane odkształcenie plastyczne cząstek proszku niklu, topienie cyny oraz infiltrację i interakcje chemiczne składników. Obecność fazy ciekłej podczas spiekania oporowego zwiększa przewodność wypraski i intensywność nagrzewania, co z kolei znacznie zwiększa szybkość skurczu, wspomaga równomierne rozprowadzenie składników oraz powstawanie faz międzymetalicznych. Opracowano makrokinetyczny model powstawania faz międzymetalicznych w systemie Ni-Sn w warunkach nieizotermicznych oraz model diamentowego materiału kompozytowego z uporządkowaną osnową i fazą metaliczną. Przeprowadzono ocenę właściwości termicznych i mechanicznych diamentowego materiału kompozytowego spiekanego oporowo. Określono początkowy skład mieszanki oraz parametry technologiczne spiekania oporowego zapewniające odpowiednią jakość DMK. Zaproponowana metoda wytwarzania wierteł w procesie ISO stwarza potencjalną podstawę do przemysłowej technologii produkcji narzędzi diamentowych.

Słowa kluczowe: kompozyty diamentowe, skurcz, spiekanie, przewodność cieplna

DOI: 10.7862/rm.2016.13

Otrzymano/received: 12.05.2016 r.
Zaakceptowano/accepted: 22.06.2016 r.

ZESZYTY NAUKOWE POLITECHNIKI RZESZOWSKIEJ 293, Mechanika 88
RUTMech, t. XXXIII, z. 88 (2/16), kwiecień-czerwiec 2016, s. 167-181

Gennady SHUSHKEVICH[1]
Svetlana SHUSHKEVICH[2]
Feliks STACHOWICZ[3]

THE SCATTERING OF THE SOUND FIELD BY THIN UNCLOSED SPHERICAL SHELL AND ELLIPSOID

In this paper the result of solution of the axisymmetric problem of the scattering of sound field by unclosed spherical shell and a soft prolate ellipsoid of rotation is presented. Spherical radiator is located in a thin unclosed spherical shell as the source of acoustic field. The equation of the spheroidal boundary is given in spherical coordinates. Scattered pressure field is expressed in terms of spherical wave functions. Using corresponding theorems of addition and assuming small eccentricity of ellipse, the solution of boundary value problem is reduced to solving dual equations with Legendre's polynomials, which are converted to infinite system of linear algebraic equations of the second kind with completely continuous operator. Numerical results are given for various values of the parameters of the problem.

Keywords: sound field, spherical shell, ellipsoid of rotation, spherical radiator

1. Introduction

Many researchers have solved the problem of sound scattering on spheroid by different methods. For example, the scattering of the sound field by hard or soft, prolate or oblate spheroids are considered in [1-7]. The results of the scattering of sound permeable and elastic spheroids are studied in the works [8-12]. Analytical description of the acoustic field scattered by inhomogeneous elastic spheroid is obtained in [13]. In [14] analytical solution of the problem of diffractions of plane sound wave on elastic spheroid with arbitrary located spherical cavity is considered.

In this paper analytical solution of the axisymmetric problem of scattering of sound field by unclosed spherical shell and soft prolate ellipsoid of rotation is

[1] Autor do korespondencji/corresponding author: Gennady Shushkevich, Yanka Kupala State University of Grodno, 22,Ozheshko St., 230023 Grodno, Belarus, e-mail: g_shu@tut.by

[2] Svetlana Shushkevich, Yanka Kupala State University of Grodno, e-mail: spusha@list.ru

[3] Feliks Stachowicz, Rzeszow University of Technology, e-mail: stafel@prz.edu.pl

presented. A spherical radiator was located in the thin unclosed spherical shell as the source of the acoustic field. The equation of spheroidal boundary is given in spherical coordinates. The solution of boundary value problem is reduced to solving dual equations with Legendre's polynomials which are converted to infinite system of linear algebraic equations of the second kind with completely continuous operator. Numerical results are given for various values of parameters of the problem.

2. Problem formulation

Let homogeneous space R^3 contain a thin unclosed spherical shell $\Gamma_1$located on the sphere $\Gamma$of radius with the center at the point O and a prolate ellipsoid of revolution S where a is semi-major axis of the ellipse b is a minor axis of the ellipse a>b (fig. 1). We denote by $D_1$the area of space bounded by the sphere Γ and by D_3 the area of space bounded by the ellipsoid S. The distance between points O and $O_1$is equal to h_1. Then $D_2 = R^3 \setminus (D_1 \cup \Gamma \cup D_3 \cup S)$.

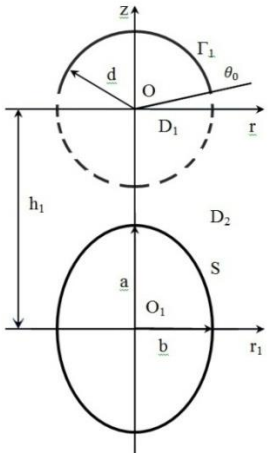

Fig. 1. Geometry of the problem

A point radiator of sound waves oscillating with an angular frequency ω is located at the point O. The areas D_j = 1, 2 are filled with the material in which shear waves do not distribute. Let denote the density of medium by ρ and speed of sound by c in D_j.To solve this problem we connect spherical coordinates with point O and point O_1. Spherical shell Γ_1 and ellipsoidal shell S are described as follows:

$$\Gamma_1 = \{r = d,\ 0 \le \theta \le \theta_0 < \pi,\ 0 \le \varphi \le 2\pi\} \tag{1}$$

$$S = \{r_1 = \gamma(\theta_1),\ 0 \le \theta_1 \le \pi,\ 0 \le \varphi \le 2\pi\} \tag{2}$$

where: $\gamma(\theta_1) = a / \sqrt{1 - V \sin^2 \theta_1}$, $V = 1 - (a/b)^2$.

Let p_c be the pressure of the sound field of the primary point radiator, p_j is secondary sound pressure field in the area D_j, j = 1, 2. The actual sound pressure is calculated by the formula $P_j = \mathrm{Re}(p_j e^{-i\omega t})$.The solution of the diffraction problem is reduced to finding pressures p_j, j = 1, 2, which satisfy:

- Helmholtz equation [15, 16]

$$\Delta p_j + k^2 p_j = 0 \tag{3}$$

where $\Delta = \frac{\partial^2}{\partial x^2} + \frac{\partial^2}{\partial y^2} + \frac{\partial^2}{\partial z^2}$ is Laplace's operator, $k = \omega/c$ is the wave number,

- boundary condition on the surface of spherical shell Γ_1 (acoustically hard shell):

$$\frac{\partial}{\partial \vec{n}} (p_c + p_1)\Big|_{\Gamma_1} = 0, \tag{4}$$

where $\vec{n}$ is the normal to the surface Γ_1,

- boundary conditions on the surface of ellipsoidal shell S (acoustically soft shell):

$$p_2\big|_S = 0 \tag{5}$$

and the condition at infinity [16]:

$$\lim_{M \to \infty} r \left(\frac{\partial p_2(M)}{\partial r} - ik p_2(M) \right) = 0 \tag{6}$$

where M is an arbitrary point at the space.

Condition of continuity of the pressure on the open part of the spherical shell $\Gamma \setminus \Gamma_1$ is given by:

$$(p_c + p_1)\Big|_{\Gamma \setminus \Gamma_1} = p_2\big|_{\Gamma \setminus \Gamma_1} \tag{7}$$

and normal derivative on the surface of the sphere Γ is:

$$\frac{\partial}{\partial r} (p_c + p_1)\Big|_{\Gamma} = \frac{\partial}{\partial r} p_2 \Big|_{\Gamma} \tag{8}$$

Initial pressure of the sound field can be represented in the form [16]:

$$p_c(r,\theta) = P\exp(ikr)/r = P\sum_{n=0}^{\infty} f_n h_n^{(1)}(kr)P_n(\cos\theta), \quad f_n = ik\delta_{0n} \tag{9}$$

where $h_n^{(1)}(x)$ are spherical Hankel's functions, $P_n(\cos\theta)$ are Legendre's polynomials [17], δ_{0n} is Kronecker's delta, P is a constant.

The pressure of the scattered sound field is represented as superposition of basic solutions of Helmholtz equation in spherical coordinates [18, 19] taking into account the condition at infinity (6):

$$p_1(r,\theta) = P\sum_{n=0}^{\infty} c_n j_n(kr)P_n(\cos\theta), \quad r < d, \tag{10}$$

$$p_2 = p_2^{(1)}(r,\theta) + p_2^{(2)}(r_1,\theta_1), \tag{11}$$

$$p_2^{(1)}(r,\theta) = P\sum_{n=0}^{\infty} x_n h_n^{(1)}(kr)P_n(\cos\theta), \quad r > d, \tag{12}$$

$$p_2^{(2)}(r_1,\theta_1) = P\sum_{n=0}^{\infty} y_n h_n^{(1)}(kr_1)P_n(\cos\theta_1), \quad r_1 > \gamma(\theta_1), \tag{13}$$

where $j_n(x)$ are spherical Bessel's functions of first kind [17]. Unknown coefficients c_n, x_n, y_n must be determined from the boundary conditions.

3. Boundary conditions

Let's perform boundary conditions (4), (7), (8). For this purpose the function $p_2^{(2)}(r_1,\theta_1)$ through spherical wave functions in the coordinate system with origin at the point O can be determined using the formula connecting spherical wave functions [18, 19]:

$$h_n^{(1)}(kr_1)P_n(\cos\theta_1) = \sum_{k=0}^{\infty} A_{nk}(h_1)j_k(kr)P_k(\cos\theta), \quad r < h_1, \tag{14}$$

Then

$$p_2^{(2)}(r,\theta) = P\sum_{n=0}^{\infty} p_n j_n(kr)P_n(\cos\theta), \quad p_n = \sum_{k=0}^{\infty} y_k A_{kn}(h_1), \tag{15}$$

where

$$A_{nk}(h_1) = (2k+1)\sum_{\sigma=|k-n|}^{k+n} i^{\sigma+k-n}\, b_{\sigma}^{(n0k0)}\, h_{\sigma}^{(1)}(kh_1), \tag{16}$$

$b_{\sigma}^{(n0q0)} = (nq00\,|\,\sigma 0)^2$, $(nq00\,|\,\sigma 0)$ is the Klepshev-Gordona coefficient [16].

According to representations (10)-(12), (15), the boundary condition (5) taking into account the condition of orthogonality of Legendre polynomials on the interval $[0;\ \pi]$ becomes:

$$\left.\begin{aligned} &f_n \frac{d}{d\xi} h_n^{(1)}(\xi_0) + c_n \frac{d}{d\xi} j_n(\xi_0) = x_n \frac{d}{d\xi} h_n^{(1)}(\xi_0) + p_n \frac{d}{d\xi} j_n(\xi_0), \\ &\xi_0 = kd,\ \ n = 0, 1, \ldots\ . \end{aligned}\right\} \tag{17}$$

Let us perform the boundary condition (4) on the surface of the spherical shell and the condition of continuity (7). Let us exclude factors c_n in the resulting equations using the representation (17), and we obtain dual equations in Legendre's polynomial:

$$\left.\begin{aligned} &\sum_{n=0}^{\infty} x_n \frac{d}{d\xi_0} h_n^{(1)}(\xi_0) P_n(\cos\theta) = -\sum_{n=o}^{\infty} p_n \frac{d}{d\xi_0} j_n(\xi_0) P_n(\cos\theta), \quad 0 \le \theta < \theta_0, \\ &\sum_{n=0}^{\infty} \frac{x_n - f_n}{\dfrac{d}{d\xi_0} j_n(\xi_0)} P_n(\cos\theta) = 0, \quad \theta_0 < \theta \le \pi. \end{aligned}\right\} \tag{18}$$

Let new coefficients be

$$x_n = X_n \frac{d}{d\xi_0} j_n(\xi_0) + f_n,\ n = 0, 1, \ldots, \tag{19}$$

and a small parameter is

$$g_n = 1 + \frac{4i\xi_0^3}{2n+1} \frac{d}{d\xi_0} j_n(\xi_0) \frac{d}{d\xi_0} h_n^{(1)}(\xi_0),\ g_n = O\left(n^{-2}\right),\ \ n \gg \xi_0\,. \tag{20}$$

As a result dual equations (18) take the form:

$$\left.\begin{aligned}&\sum_{n=0}^{\infty}(2n+1)(1-g_n)X_nP_n(\cos\theta)=\sum_{n=o}^{\infty}(2n+1)(\tilde{f}_n+\tilde{p}_n)P_n(\cos\theta),\ 0\le\theta<\theta_0,\\&\sum_{n=0}^{\infty}X_nP_n(\cos\theta)=0,\quad \theta_0<\theta\le\pi,\end{aligned}\right\}\tag{21}$$

where

$$\tilde{f}_n=4i\xi_0^3f_n\frac{d}{d\xi_0}h_n^{(1)}(\xi_0)/(2n+1),\qquad \tilde{p}_n=4i\xi_0^3p_n\frac{d}{d\xi_0}j_n(\xi_0)/(2n+1)\tag{22}$$

Dual equations (18) are converted to infinite system of linear algebraic equations of the second kind with the completely continuous operator using the integral representation for Legendre's polynomials [19, 20]:

$$X_n-\sum_{k=0}^{\infty}g_kR_{nk}(\theta_0)X_k=\sum_{k=0}^{\infty}\left(\tilde{p}_k+\tilde{f}_k\right)R_{nk}(\theta_0),\qquad n=0,1,\ldots,\tag{23}$$

where

$$\left.\begin{aligned}&R_{nk}(\theta_0)=\frac{1}{\pi}\left[\frac{\sin(n-k)\theta_0}{n-k}-\frac{\sin(n+k+1)\theta_0}{n+k+1}\right],\\&\left.\frac{\sin(n-k)\theta_0}{n-k}\right|_{n=k}=\theta_0.\end{aligned}\right\},\tag{24}$$

To analyze boundary conditions (5) we express the function $p_2^{(1)}(r,\theta)$ through spherical wave functions in the coordinate system with origin at the point O using formula [18,19]:

$$h_n^{(1)}(kr)P_n(\cos\theta)=\sum_{k=0}^{\infty}B_{nk}(h_1)j_k(kr_1)P_k(\cos\theta_1),\quad r_1<h_1,\tag{25}$$

then

$$p_2^{(1)}(r_1,\theta_1)=P\sum_{n=0}^{\infty}z_nj_n(kr_1)P_n(\cos\theta_1),\quad z_n=\sum_{p=0}^{\infty}x_pB_{pn}(h_1),\tag{26}$$

where

$$B_{nk}(h_1)=(2k+1)\sum_{\sigma=|k-n|}^{k+n}(-1)^{\sigma}\,i^{\sigma+k-n}\,b_{\sigma}^{(n0k0)}\,h_{\sigma}^{(1)}(kh_1) \tag{27}$$

Taking into account the representation (13), (26) and boundary conditions (5) we obtain

$$\sum_{n=0}^{\infty}z_n\,j_n\left(k\gamma(\theta_1)\right)P_n(\cos\theta_1)+\sum_{n=0}^{\infty}y_n h_n^{(1)}\left(k_0\gamma(\theta_1)\right)P_n(\cos\theta_1)=0 \tag{28}$$

We transform the relation (28) and assume that the eccentricity of ellipse is $h=\sqrt{1-b^2/a^2}<<1$, $a>b$, then

$$\left.\begin{aligned}&V=-h^2-h^4-h^6+O(h^8),\quad \gamma(\theta_1)=a\left[1-\frac{h^2}{2}\sin^2\theta_1-\frac{h^4}{2}\left(\sin^2\theta_1-\right.\right.\right.\\&\left.\left.\left.-\frac{3}{4}\sin^4\theta_1\right)-\frac{h^6}{2}\left(\sin^2\theta_1-\frac{3}{2}\sin^4\theta_1+\frac{5}{8}\sin^6\theta_1\right)\right]+O\left(h^8\right).\end{aligned}\right\} \tag{29}$$

Now we factorize spherical functions $j_n\left(\gamma(\theta_1)\right)$, $h_n^{(1)}\left(\gamma(\theta_1)\right)$ in series with respect to small parameter h:

$$\left.\begin{aligned}&j_n\left(k\gamma(\theta_1)\right)=j_n(\xi_1)-\frac{\sin^2\theta_1}{2}\xi_1 j_n'(\xi_1)h^2-\left(\xi_1 j_n'(\xi_1)\left(\frac{\sin^2\theta_1}{2}-\frac{3\sin^4\theta_1}{8}\right)-\right.\\&\left.-\frac{{\xi_1}^2 j_n''(\xi_1)}{8}\sin^4\theta_1\right)h^4-\left(\xi_1 j_n'(\xi_1)\left(\frac{5\sin^6\theta_1}{16}-\frac{3\sin^4\theta_1}{4}+\frac{\sin^2\theta_1}{2}\right)-\right.\\&\left.-{\xi_1}^2 j_n''(\xi_1)\left(\frac{\sin^4\theta_1}{4}-\frac{3\sin^6\theta_1}{16}\right)+\frac{{\xi_1}^3 j_n'''(\xi_1)\sin^6\theta_1}{48}\right)h^6+O\left(h^8\right),\ \xi_1=ka.\end{aligned}\right\} \tag{30}$$

Similar expansion as (30) holds for the function $h_n^{(1)}\left(\gamma(\theta_1)\right)$, but instead of the function $j_n(\xi_1)$ is the function $h_n^{(1)}(\xi_1)$. Expansions for spherical functions can be written as follows:

$$\left.\begin{aligned}&j_n\left(k\gamma(\theta_1)\right)=p_n^{(0)}(\xi_1)+p_n^{(1)}(\xi_1)\sin^2\theta_1+p_n^{(2)}(\xi_1)\sin^4\theta_1+p_n^{(3)}(\xi_1)\sin^6\theta_1\\&h_n^{(1)}\left(k\gamma(\theta_1)\right)=m_n^{(0)}(\xi_1)+m_n^{(1)}(\xi_1)\sin^2\theta_1+m_n^{(2)}(\xi_1)\sin^4\theta_1+m_n^{(3)}(\xi_1)\sin^6\theta_1\end{aligned}\right\} \tag{31}$$

where

$$\left.\begin{aligned}
&p_n^{(0)}(\xi_1)=j_n(\xi_1),\quad p_n^{(1)}(\xi_1)=-\xi_1(h^2+h^4+h^6)j_n'(\xi_1)/2,\\
&p_n^{(2)}(\xi_1)=\left(3h^4+6h^6\right)\xi_1 j_n'(\xi_1)/8+\left(h^4+2h^6\right)\xi_1^2 j_n''(\xi_1)/8,\\
&p_n^{(3)}(\xi_1)=-(15\xi j_n'(\xi_1)+9\xi_1^2 j_n''(\xi_1)+\xi_1^3 j_n'''(\xi_1))h^6/48,\\
&m_n^{(0)}(\xi_1)=h_n^{(1)}(\xi_1),\quad {}_n^{(1)}(\xi_1)=-\xi_1\left[h^2+h^4+h^6\right]\left(h_n^{(1)}(\xi_1)\right)'/2,\\
&m_n^{(2)}(\xi_1)=\left(3h^4+6h^6\right)\xi_1\left(h_n^{(1)}(\xi_1)\right)'/8+\left(h^4+2h^6\right)\xi_1^2\left(h_n^{(1)}(\xi_1)\right)''/8,\\
&m_n^{(3)}(\xi_1)=-\left[15\xi_1\left(h_n^{(1)}(\xi_1)\right)'+9\xi_1^2\left(h_n^{(1)}(\xi_1)\right)''+\xi_1^3\left(h_n^{(1)}(\xi_1)\right)'''\right]h^6/48.
\end{aligned}\right\}\qquad(32)$$

Let us exclude factors z_n in (28) using the representations (27), (19) and expansions (31). We multiply the resulting equation by $P_s(\cos\theta)\sin\theta d\theta$, s = 0, 1, 2,…, and integrate from 0 to π, then we have:

$$\sum_{n=0}^{\infty} X_n\tilde{a}_{ns}(\xi_0,\xi_1,h_1)+\sum_{n=0}^{\infty} y_n b_{ns}(\xi_1)=-ik\sum_{n=0}^{\infty} B_{0n}(h_1)\,a_{ns}(\xi_1),\ s=0,1,\ldots,\quad(33)$$

where

$$\left.\begin{aligned}
&\tilde{a}_{ns}(\xi_0,\xi_1,h_1)=\frac{d}{d\xi_0}j_n(\xi_0)\sum_{m=0}^{\infty} B_{nm}(h_1)a_{ms}(\xi_1),\\
&a_{ns}(\xi_1)=p_n^{(0)}(\xi_1)I_{ns}^{(1)}+p_n^{(1)}(\xi_1)I_{ns}^{(3)}+p_n^{(2)}(\xi_1)I_{ns}^{(5)}+p_n^{(3)}(\xi_1)I_{ns}^{(7)},\\
&b_{ns}(\xi_1)=m_n^{(0)}(\xi_1)I_{ns}^{(1)}+m_n^{(1)}(\xi_1)I_{ns}^{(3)}+m_n^{(2)}(\xi_1)I_{ns}^{(5)}+m_n^{(3)}(\xi_1)I_{ns}^{(7)},
\end{aligned}\right\}\qquad(34)$$

$$I_{ns}^{(\alpha)}=\int_0^{\pi} P_n(\cos\theta)P_s(\cos\theta)\sin^{\alpha}\theta d\theta,\ \alpha=1,3,5,7\qquad(35)$$

The values of the integrals $I_{ns}^{(\alpha)}$ are given in Appendix. So we have the following connected system of linear algebraic equations for the unknown coefficients from Eqs. (23), (33):

$$\left.\begin{aligned}
&\sum_{n=0}^{\infty}\left(g_n R_{sn}(\theta_0)-\delta_{ns}\right)X_n+\sum_{n=0}^{\infty}\tilde{b}_{ns}(\xi_0,\theta_0,h_1)y_n=4\xi_0^3 k\frac{d}{d\xi_0}h_0^{(1)}(\xi_0)R_{s0}(\theta_0),\\
&\sum_{n=0}^{\infty}X_n\tilde{a}_{ns}(\xi_0,\xi_1,h_1)+\sum_{n=0}^{\infty}y_n b_{ns}(\xi_1)=-ik\sum_{n=0}^{\infty}B_{0n}(h_1)\,a_{ns}(\xi_1),\quad s=0,1,2,\ldots,
\end{aligned}\right\}\qquad(36)$$

where

$$\tilde{b}_{ns}(\xi_0,\theta_0,h_1)=4i\xi_0^3\sum_{p=0}^{\infty}\frac{d}{d\xi_0}j_p(\xi_0)R_{sp}(\theta_0)A_{np}(h_1)/(2p+1)\qquad(37)$$

4. Calculation of the far field

On the basis of formula:

$$\left.\begin{aligned}
&h_n^{(1)}(kr_1)P_n(\cos\theta_1)=\sum_{p=0}^{\infty}\tilde{A}_{np}(h_1)h_p^{(1)}(kr)P_p(\cos\theta),\quad r>h_1,\\
&\tilde{A}_{np}(h_1)=\sum_{\sigma=|p-n|}^{p+n}(2\sigma+1)i^{\sigma+p-n}\,b_p^{(n0\sigma0)}\,j_\sigma(kh_1)
\end{aligned}\right\}\qquad(38)$$

we have representation of the function $p_2^{(2)}(r_1,\theta_1)$ in coordinate system with origin at the point O

$$p_2^{(2)}(r,\theta)=P\sum_{n=0}^{\infty}U_n h_n^{(1)}(kr)P_n(\cos\theta),\quad U_n(h_1)=\sum_{p=0}^{\infty}\tilde{A}_{pn}(h_1)y_p\qquad(39)$$

Using the asymptotic expression for the function $h_n^{(1)}(kr)$ [16]:

$$h_n^{(1)}(kr)\approx(-i)^{n+1}e^{ikr}/kr,\quad kr\to\infty\qquad(40)$$

we obtain representation of pressure in the far field zone:

$$p_2(r,\theta)=P\frac{e^{ikr}}{kr}G(\theta)\qquad(41)$$

where

$$G(\theta)=\sum_{n=0}^{\infty}(-i)^{n+1}\left(X_n\frac{d}{d\xi_0}j_n(\xi_0)+f_n+\sum_{p=0}^{\infty}\tilde{A}_{pn}(h_1)y_p\right)P_n(\cos\theta) \tag{42}$$

The function $G(\theta)$ for some parameters of the problem is calculated using a computer algebra system Mathcad [21]. Spherical functions were calculated by means of built-in functions. Derivatives of spherical functions were calculated by means of the recurrent formulas [17].The infinite system (36) was solved by the method of truncation [16]. The computational experiment showed that the truncation order for the considered parameters of the problem can be equal to 25. It provides the solution of the system (36) with accuracy 10^{-4}. Figure 2 shows plots of the function $G(\theta)$ for some values of the angle $\theta_0$of thin unclosed spherical shell Γ_1. The parameters are equal to: $h_1 = 1.0$ m, $a = 0.2$ m, $b = 0.9a$, $k = 1.5$ m^{-1}. Figure 3 shows plots of the function $G(\theta)$ for some values of the wave number k.The parameters are equal to: $h_1 = 1.0$ m, $d = 0.2$ m, $a = 0.2$ m, $b = 0.9a$, $\theta_0 = 90^0$. Figure 4 shows plots of the function $G(\theta)$for some values b/a and parameters are equal to: $h_1 = 0.7$ m, $d = 0.2$ m, $a = 0.2$ m, $k = 4$ m^{-1}, $\theta_0 = 90^0$.

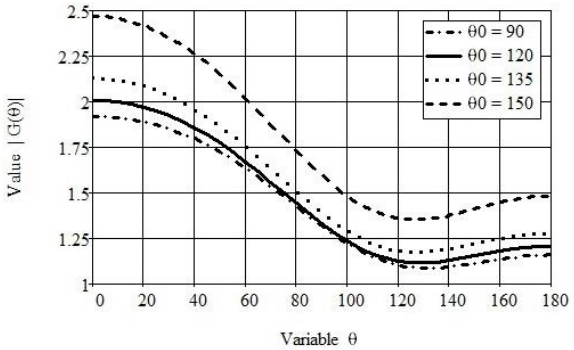

Fig. 2. Graph of function $G(\theta)$ for some values of the angle θ_0

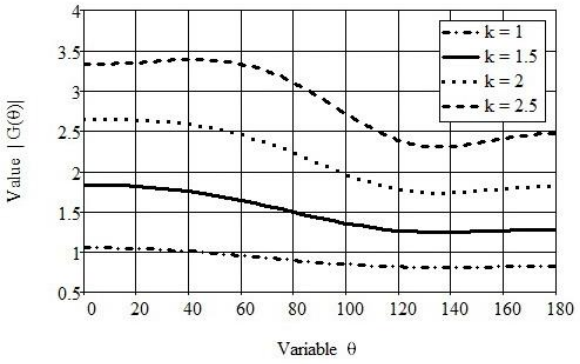

Fig. 3. Graph of function $G(\theta)$ for some values of the wave number k

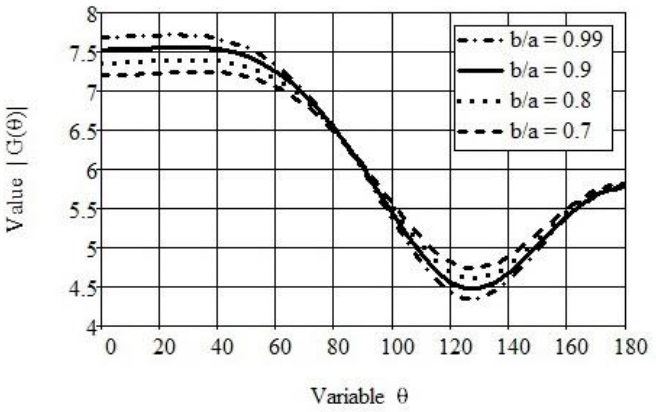

Fig. 4. Graphs of function G(θ) for some values b/a

5. Conclusions

The solution of the problem of the scattering of sound field by unclosed spherical shell and a soft prolate ellipsoid is reduced to solving dual equations in Legendre's polynomials using the addition theorem for spherical wave functions. The spherical radiator is considered as the source of the sound field located within the thin unclosed spherical shell. The equation of spheroidal boundary is considered in spherical coordinates. Following tasks were carried out:

- scattered pressure field is expressed in terms of spherical wave functions,
- dual equations are converted to the infinite system of linear algebraic equations of the second kind with the completely continuous operator,
- numerical results for various values of the parameters of the problem were computed.

The developed methodology and the software can be practically used in the manufacture of sound screens.

Appendix

The values of the integrals $I_{ns}^{(\alpha)}$.

Using recurrence relations for Legendre polynomials

$$x^2 P_n(x) = \frac{n(n-1)}{(2n-1)(2n+1)} P_{n-2}(x) + \frac{2n^2+2n-1}{(2n-1)(2n+3)} P_n(x) + \left. \right\}$$

$$+ \frac{(n-1)(n+2)}{(2n+)(2n+3)} P_{n+2}(x), \left. \right\}$$

$$
\left.
\begin{aligned}
x^4 P_n(x) = {} & \frac{n(n-1)(n-2)(n-3)}{(2n+1)(2n-1)(2n-3)(2n-5)} P_{n-4}(x) + \\
& + \frac{n(n-1)\left(4n^2-4n-14\right)}{(2n-5)(2n-1)(2n+1)(2n+3)} P_{n-2}(x) + \frac{3\left(2n^4+4n^3-2n^2-8n+3\right)}{(2n-3)(2n-1)(2n+3)(2n+5)} P_n(x) + \\
& + \frac{(n+1)(n+2)\left(4n^2+12n-6\right)}{(2n-1)(2n+1)(2n+3)(2n+7)} P_{n+2}(x) + \frac{(n+1)(n+2)(n+3)(2+4)}{(2n+1)(2n+3)(2n+5)(2n+7)} P_{n+4}(x)
\end{aligned}
\right\}
$$

and the value of the integral

$$
I_{sn}^{(1)} = \int_0^{\pi} P_n(\cos\theta) P_s(\cos\theta) \sin\theta d\theta = \begin{cases} \dfrac{2}{2n+1}, & s = n, \\ 0, & s \neq n, \end{cases}
$$

we obtain the following values of integrals

$$
I_{sn}^{(3)} = \begin{cases} \dfrac{-2n(n-1)}{(2n-3)(2n-1)(2n+1)}, & s = n-2, \\ \dfrac{4\left(s^2+s-1\right)}{(2s-1)(2s+1)(2s+3)}, & s = n, \\ \dfrac{-2(n+1)(n+2)}{(2n+1)(2n+3)(2n+5)}, & s = n+2, \\ 0, & s \neq n, \end{cases}
$$

$$I_{sn}^{(3)}=\begin{cases}\dfrac{2n(n-3)(n-2)(n-1)}{(2n-7)(2n-5)(2n-3)(2n-1)(2n+1)}, & s=n-4,\\ \dfrac{8n(n-1)\left(-n^2+n+4\right)}{(2n-5)(2n-3)(2n-1)(2n+1)(2n+3)}, & s=n-2\\ \dfrac{4\left(3n^4+6n^3-8n^2-14n+12\right)}{(2n-3)(2n-1)(2n+1)(2n+3)(2n+5)}, & s=n,\\ \dfrac{8(n+1)(n+2)\left(-n^2-3n+2\right)}{(2n-1)(2n+1)(2n+3)(2n+5)(2n+7)}, & s=n+2,\\ \dfrac{2(n+1)(n+2)(n+3)(n+4)}{(2n+1)(2n+3)(2n+5)(2n+7)(2n+9)}, & s=n+4,\\ 0, & s\neq n,\end{cases}$$

$$I_{sn}^{(7)}=\begin{cases}\dfrac{-2(n-5)(n-4)(n-3)(n-2)(n-1)n}{(2n-11)(2n-9)(2n-7)(2n-5)(2n-3)(2n-1)(2n+1)}, & s=n-6,\\ \dfrac{-12n(n-3)(n-2)(n-1)\left(-n^2+3n+7\right)}{(2n-9)(2n-7)(2n-5)(2n-3)(2n-1)(2n+1)(2n+3)}, & s=n-4,\\ \dfrac{-6n(n-1)\left(5n^4-10n^3-59n^2+64n+180\right)}{(2n-7)(2n-5)(2n-3)(2n-1)(2n+1)(2n+3)(2n+5)}, & s=n-2,\\ \dfrac{8\left(5n^6+15n^5-52n^4-129n^3+155n^2+222n-180\right)}{(2n-5)(2n-3)(2n-1)(2n+1)(2n+3)(2n+5)(2n+7)}, & s=n,\\ \dfrac{-6(n+1)(n+2)\left(5n^4+30n^3+n^2-132n+72\right)}{(2n-3)(2n-1)(2n+1)(2n+3)(2n+5)(2n+7)(2n+9)} & \text{if } s=n+2\\ \dfrac{12(n+1)(n+2)(n+3)(n+4)\left(n^2+5n-3\right)}{(2n-1)(2n+1)(2n+3)(2n+5)(2n+7)(2n+9)(2n+11)}, & s=n+4,\\ \dfrac{-2(n+1)(n+2)(n+3)(n+4)(n+5)(n+6)}{(2n+1)(2n+3)(2n+5)(2n+7)(2n+9)(2n+11)(2n+13)}, & s=n+6,\\ 0, & n\neq s.\end{cases}$$

Acknowledgement

The research leading to these results has supported by funding from the People Programme (Marie Curie International Research Staff Exchange) of the EU FP7/2007-2013/ under REA grant agreement n° PIRSES-GA-2013-610547.

References

[1] Kleshchev A.A., Sheiba L.S.: Scattering of a sound wave by ideal prolate spheroids, Acoustic J., 16 (1970) 264-268 (in Russian).

[2] Sidman R.D.: Scattering of acoustical waves by a prolate spherical obstacle, J. Acoust. Soc. America, 52 (1972) 879-883.

[3] Lauchle G.C.: Short-wavelength acoustic diffraction by prolate spheroids. J. Acoust. Soc. America, 58 (1975) 568-575.

[4] Germon A., Lauchle G.C.: Axisymmetric diffraction of spherical waves by a prolate spheroid, J. Acoust. Soc. America, 65 (1979) 1322-1327.

[5] Varadan V.K., Varadan V.V., Dragonette L.R., Flax L.: Computation of rigid body by prolate spheroids using the T-matrix approach, J. Acoust. Soc. America, 71 (1982), 22-25.

[6] Sammelmann G.S., Trivett D.H., Hackmann R.H.: High-frequency scattering from rigid prolate spheroids, J. Acoust. Soc. America, 83 (1988) 46-54.

[7] Barton J.P., Wolf N.L., Zhang H., Tarawneh C.: Near-field calculations for a rigid spheroid with an arbitrary incident acoustic field, J. Acoust. Soc. America, 103 (2003) 1266-1222.

[8] Burke J.E.: Scattering by penetrable spheroids, J. Acoust. Soc. America, 43 (1968) 871-875.

[9] Kotsis A.D., Roumeliotis J.A.: Acoustic scattering by a penetrable spheroid, Acoust. Phys., 54 (2008) 153-167.

[10] Kleshchev A.A., Rostovcev D.M.: Scattering of a sound by elastic and liquid ellipsoidal shells of revolution, Acoustic J., 32 (1986) 691-694 (in Russian).

[11] Kleshchev A.A. With reference to low frequency resonances of elastic spheroidal bodies, J. Techn. Ac., 2 (1995) 27-28.

[12] Bao X.L., Uberall H., Niemiec J.: Experimental study of sound scattering by elastic spheroids, J. Acoust. Soc. America, 102 (1997) 933-942.

[13] Tolokonnikov L. A., Lobanov A. V.: About scattering of plane sound wave by inhomogeneous elastic spheroid, Proc. Tula Stat. Univ. Natural Sci., 3 (2011) 119-125 (in Russian).

[14] Tolokonnikov L. A.: Diffraction of plane sound wave on elastic spheroid with arbitrary located spherical vacuity, Proc. Tula State Univ. Natural Sci., 2 (2011) 169-175 (in Russian).

[15] Grinchenko V.T., Vovk I.V., Matsipura V.T.: Fundamentals of acoustics, Naukova dumka, Kiev 2007 (in Russian).

[16] Ivanov E. A.: Diffraction of electromagnetic waves on two bodies, Springfield, Washington 1970.

[17] Handbook of Mathematical Functions: with Formulas,Graphs and Mathematical Tables, Eds. by M. Abramowitz and I. A. Stegun, Dover, New York 1972.

[18] Erofeenko V.T.: Addition theorems, Nauka i Technika, Minsk 1989 (in Russian).

[19] Shushkevich G.Ch., Kiselyova N.N.: Penetration of sound field through multi-layered spherical shell, Informatika, 3 (2013) 47-57 (in Russian).

[20] Rezunenko V.A. Diffraction of plane acoustic wave on sphere with circular aperture, Bulletin Kharkiv Nat. Univ., serie Mat., Appl. Mat. Mech., 850 (2009) 71-77 (in Russian).

[21] Shushkevich G.Ch., Shushkevich S.V.: Computer technology in mathematics.The system Mathcad 14: in 2 parts, Grevsova, Minsk 2012 (in Russian).

ROZPROSZENIE POLA AKUSTYCZNEGO ZA POMOCĄ CIENKIEJ NIEZAMKNIĘTEJ KULISTEJ POWŁOKI ORAZ ELIPSOIDY

S t r e s z c z e n i e

W niniejszym opracowaniu zaprezentowano wyniki rozwiązania osiowosymetrycznego problemu rozproszenia pola dźwiękowego przez niezamkniętą powłokę kulistą oraz lekko wydłużoną elipsoidę. Radiator kulisty znajdujący się w cienkiej niezamkniętej powłoce kulistej jest źródłem pola akustycznego. Równanie granicy kulistej podane jest we współrzędnych sferycznych. Rozproszone pole ciśnienia jest wyrażona w funkcji fal sferycznych. Stosując odpowiednie twierdzenia dodawania i przy założeniu zbyt małej mimośrodowości elipsy, rozwiązanie problemu wartości brzegowych jest ograniczone do rozwiązania podwójnych równań wielomianów Legendre'a, które przekształca się w nieskończony układ liniowych równań algebraicznych drugiego rodzaju z w pełni ciągłym operatorem. Wyniki obliczeń numerycznych są podane dla różnych wartości analizowanych parametrów.

Słowa kluczowe: pole akustyczne, kulista powłoka, elipsoida obrotowa, radiator kulisty

DOI: 10.7862/rm.2016.14

Otrzymano/received: 4.05.2016 r.
Zaakceptowano/accepted: 2.06.2016 r.

Informacje dodatkowe

1. Lista recenzentów współpracujących będzie opublikowana w czwartym numerze *Zeszytów Naukowych Politechniki Rzeszowskiej*, *Mechanika*, z. 88 (4/2016) oraz zamieszczona na stronie internetowej:

   http://oficyna.portal.prz.edu.pl/pl/zeszyty-naukowe/mechanika/

2. Zasady recenzowania są udostępnione na stronie internetowej:

   http://oficyna.portal.prz.edu.pl/zasady-recenzowania/

3. Informacje dla autorów artykułów są udostępnione na stronie internetowej:

   http://oficyna.portal.prz.edu.pl/informacje-dla-autorow/

4. Formularz recenzji jest udostępniony na stronie internetowej:

   http://oficyna.portal.prz.edu.pl/pl/zeszyty-naukowe/mechanika/

5. Instrukcja dla autorów omawiająca szczegółowo strukturę artykułu, jego układ, sposób przygotowywania materiału ilustracyjnego i piśmiennictwa jest zamieszczona na stronach internetowych:

   http://oficyna.portal.prz.edu.pl/pl/instrukcja-dla-autorow/

   oraz

   http://oficyna.portal.prz.edu.pl/pl/zeszyty-naukowe/mechanika/

   w zakładce „Instrukcja dla autorów".

6. Dane kontaktowe do redakcji czasopisma, adresy pocztowe i e-mail do przesłania artykułów oraz dane kontaktowe do wydawcy są podane na stronie internetowej (Komitet Redakcyjny):

   http://oficyna.portal.prz.edu.pl/pl/zeszyty-naukowe/mechanika/

Zasady recenzowania, informacje dla autorów, formularz recenzji, instrukcja dla autorów i dane kontaktowe do redakcji czasopisma i wydawcy będą opublikowane w czwartym numerze *Zeszytów Naukowych Politechniki Rzeszowskiej, Mechanika*, z. 88 (4/2016).

Nakład 200 egz. Ark. wyd. 6,05. Ark. druk. 6,25. Papier offset. 80g B1.
Oddano do druku w czerwcu 2016 r. Wydrukowano w czerwcu 2016 r.
Drukarnia Oficyny Wydawniczej, al. Powstańców Warszawy 12, 35-959 Rzeszów
Zam. nr 89/16